Available on CMS information server

CMS AN 2008/097

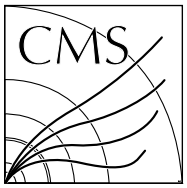

The Compact Muon Solenoid Experiment

Analysis Note

The content of this note is intended for CMS internal use and distribution only

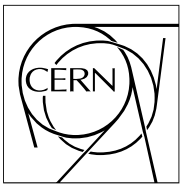

July 2, 2009

Muon Reconstruction in the CMS Detector

G. Abbiendi[1)], N. Adam[16)], J. Alcaraz[2)], N. Amapane[3)], E. Antillon[4)], R. Bellan[5)], I. Belotelov[6)], I. Bloch[7)] C. Campagnari[8)], T. Cox[9)], A. Everett[4)], A. Grelli[4)], J. Goh[10)], V. Halyo[16)], A. Hunt[16)], E. James[7)], P. Kalavase[8)], S.C. Kao[11)], M. Konecki[12)], D. Kovalskyi[8)], V. Krutelyov[8)], C. Liu [4)], D. Miller[4)] M. Mulders[5)], N. Neumeister [4)], D. Pagano[4)], J. Pivarski[14)], J. Ribnik[8)], S. Stoynev[13)], P. Traczyk[5)], D. Trocino[3)], J.R. Vlimant[8)], R. Wilkinson[15)], ..., *(Author list to be completed)*

Abstract

The reconstruction of muons in CMS combining tracking and calorimeter information is described. The high-level muon physics objects are reconstructed in a multi-faceted way, with the final collection being comprised of three different muon types, Stand-alone, Global and Tracker muons. The reconstruction in the muon spectrometer starts with the reconstruction of hit positions in the DT, CSC and RPC subsystems. Hits within each DT and CSC chamber are then matched to form "segments" (track stubs). The segments are collected and matched to generate seeds that are used as a starting point for the actual track fit of DT, CSC and RPC hits. The result is a reconstructed track in the muon spectrometer, and is called "stand-alone muon". Stand-alone muon tracks are then matched with tracker tracks to generate "global muon" tracks, featuring the full CMS resolution. "Tracker muons" are muon objects reconstructed with an algorithm that starts from a silicon tracker track and looks for compatible segments in the muon chambers. A unique collection of muon objects is assembled from the stand-alone, global, and tracker muon collections. Muon isolation quantities using calorimeter information and tracker tracks for muons defined at the three different levels are combined into the muon objects.

[1)] Università di Bologna e Sezione dell'INFN, Bologna, ITALY

[2)] CIEMAT, Madrid, Spain

[3)] Università di Torino e Sezione dell'INFN, Torino, Italy

[4)] Purdue University, West Lafayette, Indiana, USA

[5)] CERN,Geneva, Switzerland

[6)] Joint Institute for Nuclear Research, Dubna, Russia

[7)] Fermi National Accelerator Laboratory, Batavia, Illinois, USA

[8)] University of California, Santa Barbara, Santa Barbara, California, USA

[9)] University of California, Davis, Davis, California, USA

[10)] Sungkyunkwan University, Suwon, Korea

[11)] University of California, Riverside, Riverside, California, USA

[12)] Institute of Experimental Physics, Warsaw, Poland

[13)] Northwestern University, Evanston, Illinois, USA

[14)] Texas A&M University, College Station, Texas, USA

[15)] California Institute of Technology, Pasadena, California, USA

[16)] Princeton University, Princeton, New Jersey, USA

Contents

List of Figures

List of Tables

1 Introduction

The CMS experiment is expected to make major new discoveries at the LHC and make precision measurements of the properties of the fundamental particles and interactions. The key to these discoveries and measurements is the ability to trigger on, and reconstruct, muons with high efficiency. The muon reconstruction algorithms have been designed to achieve these goals and this note decscribes the current performance of the algorithms. The analysis presented here is *ideal* in that it does not include effects such as miscalibration or detector inefficiencies, except those caused by the detector geometry. Similarly actual event environments or beam induced backgrounds are not studied. The performance of these algorithms has been evaluated using the full detector simulation with a magnetic field of 4 Tesla. The performance has been tested using samples of single muons generated with different values of p_{T} and flat distributions in η and ϕ and in the presence of more than one muon and with non-flat distributions. The categories of reconstruction analyzed are

- Stand-alone reconstruction: this just uses hits in the muon detectors
- Global Reconstruction: this starts with the muon segment information and then adds tracker information
- Tracker Muon reconstruction: this starts with tracks found in the inner tracker and identifies them as muon by matching expected information from the calorimeters and muon system.

In all cases the *beam* spot position is used as a constraint.

2 The CMS Muon System and Local Reconstuction

2.1 Muon System

Muon detection and reconstruction is a powerful tool for the discovery of new physics and precision measurements of standard model physics.This requires the robust detection of muons over the full acceptance of the CMS detector and over the very high background rate expected at the LHC with full luminosity. The muon system has 3 functions: muon identification, momentum measurement, and triggering over the entire kinematic range of the LHC. Excellent muon momentum resolution and trigger capability are enabled by the high-field solenoidal magnet and its flux-return yoke. The latter also serves as a hadron absorber to facilitate the identification of muons.

The muon system has 4 detector stations alternated with the segmented iron return flux yoke.The detectors consist of 3 types of gas detector staggered between the flux-return yoke according to their response in inhomogeneous magnetic fields. The measured points determine the bending curvature which in turn provides a measurement of the inverse momentum and the charge of a muon. The magnetic field is saturated inside the iron yoke at **B** = 2 T. In addition, the multi-stage flux-return yoke shields the muon detectors from hadrons to ensure that the measured particles can be identified as minimum ionizing muons.

The three types of detector are Drift Tubes (DT), Cathode Strip Chambers (CSC), and Resistive Plate chambers (RPC) arranged in a cylindrical barrel section and 2 planar endcap regions, with a total area of 25,000 meters squared.

Table 1: Muon System Detectors

Det	chamber	dimension	R	$\|z\|$	σ_R	$\sigma_z/\sigma_\phi/\sigma_t$
DT	one cell	$13 \times 42mm^2 \times 2 - 3m$			$250\mu m$	
w/2 ϕ SLs	1-4		4-7m	$\leq$6.7m	$100\mu m$	1 mrad
CSC	strip pitch	8-16 mm				2-5mm
	wires pitch	3.2 mm			$900\mu m$	
	1		5.5m	1-2.8m	$100\mu m$	$\geq$ 10 mrad
	2-4		6.5-10m	1-7m	$200\mu m$	10 mrad
RPC	1-7	(85-130)cm $\times$ 1 cm			$\approx$ cm	3 ns

The principle of gas chambers is to maintain a potential difference between the surrounding cell and a detecting probe which collects ionization. Charged particles with enough energy will ionize the gas inside the cell, and the electrons and ions will accelerate to the anodes and cathodes respectively. The drift time, which is a function of the random diffusing motion and the drift velocity due to an electric field, provides the hit spatial resolution for the particle. For a high rate environment, such as in CMS, it is important to achieve large drift velocities by using

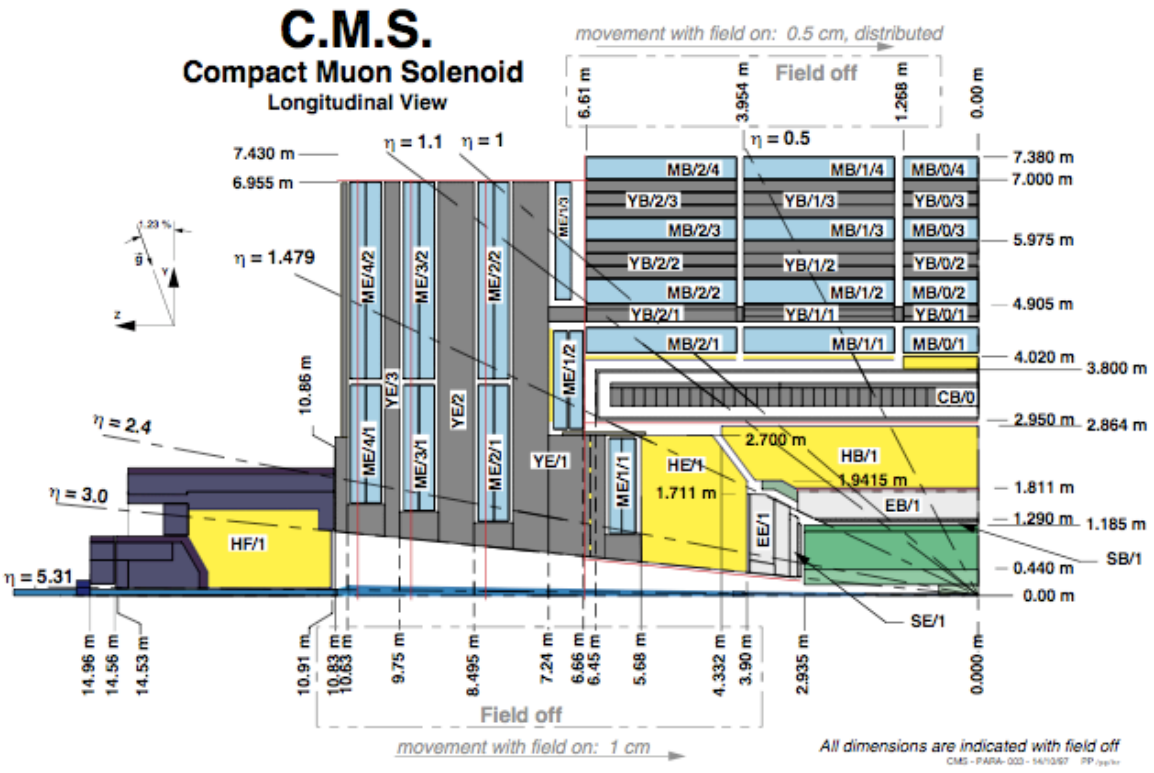

Figure 1: Longitudinal view of the muon system

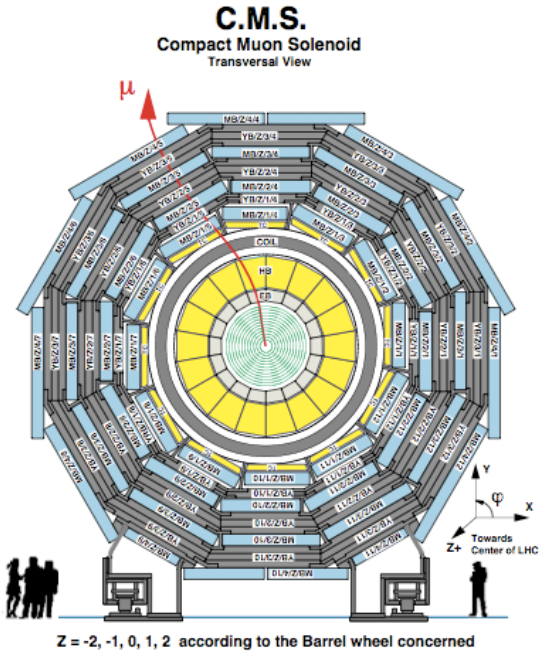

Figure 2: Transverse view of the muon system

gas mixtures that provide a large mean free path. Using the diffusion coefficient $D/\mu = kT/e$ (Einstein relation), then $\sigma(x) = \sqrt{2Dt_{drift}}$. Since $v_{drift} = \Delta x/\Delta t_{drift} = \mu E$ then

$$\sigma(x) = \sqrt{\frac{2(D/\mu)x}{E}}$$

Thus a large E/T ratio, must be maintained to achieve optimal resolution and this means a large E field, cooling, and a gas with large mobility (μ).

The CMS barrel muon detector consists of 4 stations forming concentric cylinders $|\eta| < 1.2$ around the beam line: the 3 inner cylinders have 60 drift chambers each and the outer cylinder has 70. There are about 172 000 sensitive wires. It is possible to use drift chambers as the tracking detectors for the barrel muon system because of the low expected rate and the relatively low strength of the local magnetic field which is also relatively uniform. The smallest unit of the DT detector is a drift cell 42×13mm in area by (2-3) m in depth and four rows of drift cells staggered by half a cell form a *super layer*. The final geometrical arrangement is 2 super layers along the beam and one perpendicular to it spaced by a honeycomb structure to provide support and higher angular coverage.

At the time of the LHC start-up, the CMS Endcap Muon system will consist of 468 cathode strip chambers (CSC) arranged in groups as follows: 72 ME1/1, 72 ME1/2, 72 ME1/3, 36 ME2/1, 72 ME2/2, 36 ME3/1, 72 ME3/2, and 36 ME4/1. The de-scoped 72 ME4/2 chambers will not be available during early years of CMS operation. A CSC unit has a trapezoidal shape, It is made of 6 sets of multi-wire gas chambers planes with cathode strips glued to the walls and aligned along the radial direction and perpendicular to the wires. The strip pitch is constant in $\Delta\phi$, from $\Delta\phi \approx 2.3 - 4.6$ mrad depending on the disk. The inner-most CSC detector lies inside the solenoid, so the wires have to be rotated at a Lorentz angle of 29^o to compensate for the Lorentz drift. . A muon in the pseudorapidity range $1.2 < |\eta| < 2.4$ crosses 3 or 4 CSCs. In the endcap-barrel overlap range, $0.9 < |\eta| < 1.2$, muons are detected by both the barrel drift tubes (DT) and endcap CSCs.

In both the barrel and the end caps Resistive Plate Chambers are used as part of the trigger. Resistive Plate Chambers (RPC) are gaseous parallel-plate detectors that combine adequate spatial resolution with a time resolution comparable to that of scintillators. A RPC consists of two gas chambers with a small (2mm gap) sealed by bakelite plates which are non-conductive. Both chambers are placed under a high voltage by coating the ends of the bakelite with a conductive graphite substance. An ionizing particle develops an electron avalanche that is picked up by a read out strip in contact with the anode. A RPC is capable of tagging the time of an ionizing event in a much shorter time than the 25 ns between 2 consecutive LHC *Bunch Crossings*. Therefore, a fast dedicated muon trigger device based on RPCs can identify unambiguously the relevant *Bunch Crossing* to which a muon track is associated even in the presence of the high rate and background expected at the LHC. In the barrel iron yoke, the RPC chambers form 6 coaxial sensitive cylinders (all around the beam axis) that are approximated with concentric dodecagon arrays arranged into 4 stations. In total there are 480 rectangular chambers , each one 2455 mm long in the beam direction. Exceptions are the chambers in sector 3 of wheel 1 and sector 4 of wheel +1, which are 2055 mm long to allow passage of the magnet cooling chimney. In the forward and backward regions of the CMS detector, 3 iron disks constitute the endcap yokes. In the initial detector, 3 RPC stations (RE13) are interspersed with the CSC chambers. For optimal performance of the muon spectrometer over the entire momentum range up to 1 TeV, the different muon chambers must be aligned with respect to each other and to the central tracking system to within a few hundred microns. The required alignment precision for the endcap chambers is 75 to 200 microns, while for the barrel the precision varies from 150 microns for the inner chambers of Station 1 to 350 microns for the outer chambers of Station 4. The Muon Alignment (MA) system was designed to provide continuous and accurate monitoring of the barrel and endcap muon detectors among themselves as well as alignment between them and the inner tracker detector.The optical network uses two types of light sources, LEDs and laser beams. The MA system is composed of 10 000 LEDs and 150 laser beams together with precise measuring devices consisting of 900 photo-detectors and 600 analog sensors (distance sensors and inclinometers), complemented by temperature, humidity and Hall probes.

All three muon systems, the DT, the CSC and the RPC, take part in the trigger. The barrel DT chambers provide local trigger information in the form of track segments in the ϕ -projection and hit patterns in the η -projection. The endcap CSCs deliver 3-dimensional track segments. All chamber types also identify the bunch crossing from which an event originated. The Regional Muon Trigger consists of the DT and CSC Track Finders, which join segments to complete tracks and assign physical parameters to them. In addition, the RPC trigger chambers, which have excellent timing resolution, deliver their own track candidates based on regional hit patterns. The Global Muon Trigger then combines the information from the three sub-detectors, achieving an improved momentum resolution and efficiency compared to the stand-alone systems. The initial rapidity coverage of the muon trigger is $|\eta| < 1.2$ at the startup of LHC. The design coverage is $|\eta| < 2.4$.

3 Tracking of Charged Particles and Parameter Measurements in CMS

The strategy for physics analyses in CMS is based on the reconstruction of high-level physics objects which correspond to particles traveling through the detector. The detector components record the signal of a particle as it travels through the material of the detectors, and this signal is reconstructed as individual points in space known as *recHits*. To reconstruct a physical particle traveling through the detector, the recHits are associated together to

determine points on the particle trajectory. The characteristics of the trajectory as it travels through the detector are then used to define it's momentum, charge, and particle identification.

3.1 Track Parameters

Measuring the full trajectory in space of a charged particle in a magnetic field provides a method to determine the momentum ($\vec{p} = m\gamma\vec{v}$) and charge, *q*. The *Lorentz force* provides a relation between the momentum and its motion in a magnetic field, and allows the determination of the equation of motion for the trajectory of the charged particle. Parameterizing the Lorentz force as a function of the distance along the trajectory, $s(t)$, the trajectory is given by the differential equation

$$\frac{d^2\vec{r}}{ds^2} = \frac{q}{p}\frac{d\vec{r}}{ds}B(r) \tag{1}$$

where $\frac{d\vec{r}}{ds}$ is the unit length tangent to the trajectory, and $\frac{d^2\vec{r}}{ds^2}$ is a measure of the trajectory's curvature. Thus, for a known $\vec{B}$, the momentum at a point (x, y, z) is determined by measuring the tangent to the trajectory and the curvature of the trajectory. The tangent to the trajectory makes an angle λ with respect to the magnetic field as illustrated in Fig. 3. Solving eq. 1, for known $\vec{B}$, yields three relations for $x(s)$, $y(s)$, and $z(s)$ that describe a helix in space that is parameterized by $x, y, z, \lambda, q/p$. The projection in the xy plane follows a circle with fixed radius of curvature $R_T = |\vec{p}|\cos\lambda/qB$, while the z coordinate measures the *stretch* of the helix in the direction parallel to $\vec{B}$.

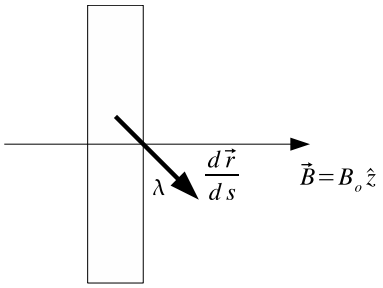

Figure 3: Tangent to the trajectory ($\frac{d\vec{r}}{ds}$) making an angle λ to a detector oriented along B

The above parameterization does not take into account three important factors caused by the real CMS detector

1. *inhomogeneous* $\vec{B}$ field
2. the energy loss as the particle travels through the detector
3. the multiple scattering which deflects the trajectory in a *stochastic* manner

Therefore, a failure to include these effects biases the most important parameters that are extracted from the trajectory: the *momentum* and its *direction*. An accurate measurement of direction is critical in determining whether the particle came from the interaction point or a detached vertex. In order to take into account these effects we use a different set of parameters that *scales* with the changes mentioned.

The magnetic field is a function of the coordinates $\vec{B}(x, y, z)$, therefore to correctly describe the trajectory it is necessary to incorporate the magnetic field changes into the parametrization. The set of parameters $\{x, y, x', y', q/|\vec{p}|\}$, at a reference surface $z = z_r$ together with the derivatives with respect to z, provides the change from the *ideal* trajectory. This new parametrization also scales with the effects of multiple scattering and localizes the trajectory to a plane region where the $\vec{B}$ field can be expanded as a perturbation to a good approximation. Thus, a solution to the trajectory in an inhomogeneous $\vec{B}$ field field can be found by using a recursive method of *Runge-Kutta* [1].

It was shown previously that in order to uniquely specify a trajectory of a helix in a region of known magnetic field, one needs to specify at least five *degrees of freedom*, where a unique determination would require infinite precision on the five parameters. For large momenta, the projection of the trajectories can be approximated by a straight line $y = a + bz$ in a plane containing the magnetic field and with a parabola $y = a + bx + (c/2)x^2$ in the plane normal to the magnetic field, with $c = -R_T^{-1}$. The uncertainties on the above parameters due to the intrinsic resolution of the detectors translates directly into an uncertainty on the momentum vector. Using typical values expected in CMS, the intrinsic momentum resolution of the detector has the following features:

1. the resolution *grows* linearly in momentum and *drops* as $\vec{B}^{-1}$ and L^{-2}
2. the *transverse* resolution dominates over the full η range in CMS

3.2 Material Effects

A charged particle will be deflected by random Coulomb scattering with the material of the detector. For sufficient material (length L), the deflection angle from its unperturbed trajectory becomes *Gaussian distributed* around zero [1] [2]. The scattering introduces an uncertainty in the position measurements and a correlation in the measurements after the material scattering. In cases where the multiple scattering dominates the uncertainty, the momentum resolution does not depend on the momentum, but there is a weak dependence on the number of measurements for a fixed amount of material and on the length of the spectrometer.

Although ionizing single atoms in a medium requires a relatively small amount of energy transfer, the additive effects do contribute in a well understood manner. The average energy loss for charged particles heavier than the electron is given by the *Bethe-Bloch* formula:

$$-\frac{dE}{dx} = \frac{const}{\beta^2} \times [\ln(\frac{2m_e c^2 \beta^2 \gamma}{\underbrace{I}_{Mean\ Excitation\ E}}) - \beta^2 - \overbrace{\delta(\beta)}^{density\ effect}] \tag{2}$$

- The constant is roughly independent of material
- a minimum ≈ 2 MeV cm^2/g is reached at $\beta = 0.96 \rightarrow E_\mu = 0.35$ GeV/c for muons
- 0.35 GeV/$c \leq E_\mu \leq 100$ GeV/c there's a slight rise of $\approx 10\%$
- $E_\mu \geq 100$ GeV/c radiation losses become significant.

This provides the statistical energy loss per unit x ($density \times length$). The method is well understood and provides a reasonable estimation for the energy [1]. The loss of energy has to be incorporated in the equations of motion, and the information can be introduced in an iterative manner.

3.3 Tracking Algorithm

The hits from the position sensitive detectors are analyzed using a pattern recognition algorithm to associate the measurements with trajectories. Independent of the sub detector information used the procedure from hits to tracks follows the same sequence and reconstructing and parameterizing a track occurs in four stages:

- seeding
- trajectory building
- trajectory cleaning
- trajectory smoothing.

The details of the tracker track algorithm and muon track algorithm are discussed elsewhere [3, 4], here we present a brief description of the tracking algorithm steps.

Trajectory Seeding The initial point for the track reconstruction is determined using an estimated trajectory state or set of hits that are compatible with the assumed physics process. The most common types of trajectory seeds in CMS are hit-based seeds and state-based seeds and it is assumed that the trajectories, and therefore the trajectory seeds, are compatible with the beam spot. Hit-based seeds require a hit-pair or hit-triplet compatible with the beam spot to provide the initial vector. Additional options are that the seed direction meet certain criteria, or that the hits be located in a certain geometric region of the detector. State-based seeds do not require any hits and are specified by an initial momentum and direction.

Trajectory Building Trajectory building starts at the position specified by the trajectory seed, and the building then proceeds in the direction specified by the seed to locate compatible hits on the subsequent detector layers. The track finding and fitting is accomplished using a combinatorial Kalman filter [5] where the full knowledge of the track parameters at each detector layer is used to find compatible measurements in the next detector layer, forming combinatorial trees of track candidates. The Kalman filter method uses an iterative approach to update the trajectory estimate $\tilde{\mathbf{p}}$ and its covariance matrix by incorporating material effects. The method starts with track parameters $\tilde{\mathbf{p}}_\mathbf{i}$ and covariance $\mathbf{C}(\tilde{\mathbf{p}}_\mathbf{i})$ at a known surface, and propagates them $(\tilde{\mathbf{p}}_{\mathbf{i+1}})$ to the next surface with the known equation of motion by incorporating scattering effects and also uses information from the subset of the measurement vector at the propagated surface $\mathbf{c}_{\mathbf{i+1}} = \mathbf{f}_{\mathbf{i+1}}(\mathbf{p}_{\mathbf{i+1}}) + \epsilon_{\mathbf{i+1}}$. In this process, the trajectory state which is propagated to the next detector layer is then *updated* with the information of a compatible hit. The final trajectory estimate is properly weighted with information from the measurement $\mathbf{m}_{\mathbf{i+1}}$ and the information with predicted state based in all preceding detectors. As discussed in Section 3.1 and Section 3.2, the propagation of a trajectory state to another position must take into account the detailed knowledge of the $\vec{B}$ field and the effects of propagating through the detector material in order to properly evaluate the position and momentum vectors. See Section 3.4 for descriptions of the propagators and the magnetic field as used in CMS tracking.

Trajectory Cleaning Trajectory building produces a large number of trajectories, many of which share a large fraction of their hits. In the cleaning stage, ambiguities among the possible trajectories are resolved and a maximum number of track candidates are kept.

Trajectory Smoothing A backward fitting (*smoothing*) allows the use of all covariance matrices to be applied to all the intermediate points based on all measurements used so far. Thus, the *Kalman filter* provides a good method in track finding/fitting since it is linear in the measurements, and its backward complement makes use of the full information, thereby providing room for robustness.

3.4 Propagators

Several propagators are used during the muon track reconstruction to perform a function of predicting the state of a muon given it's initial state vector. The propagators provide a solution of a muon transport in the detector accounting for magnetic field and energy loss in detector material to predict the mean expected path as well as provide a propagation of initial state errors (covariance matrix) to the propagation final point including material effects like multiple scattering and energy loss fluctuations.

Three propagators are used at different stages of muon reconstruction: the *analytic with material* propagator, the *Runge-Kutta* propagator, and the *stepping-helix* propagator. The first two propagators are used extensively inside the silicon tracker volume, while the latter is predominantly used to propagate muons outside the tracker volume. While the first two propagators are used in the standard tracking software, the *stepping helix* propagator is predominantly used for muon reconstruction only. In a typical muon reconstruction application when the propagated trajectory crosses into the tracker volume the *analytic with material* or the *Runge-Kutta* propagators are coupled with the *stepping helix* propagator into the *smart* propagator which internally selects which propagator is to be used depending where the initial propagation state is: the *stepping helix* propagator is chosen if the state is outside the silicon tracker volume.

Choice of a propagator to be used in a given task is driven by the speed, precision or flexibility. The *analytic with material* propagator is the fastest, but is constrained by an assumption that the magnetic field is aligned in the z-direction and does not change between the propagation points. The *Runge-Kutta* propagator provides a transport solution using the fourth order Runge-Kutta method and takes into account the non-uniform magnetic field. Both the *analytic with material* and the *Runge-Kutta* propagators are available through the *PropagatorWithMaterial* which accounts for material effects by introducing them at the initial propagation state and then calls either the *analytic* or the *Runge-Kutta* propagators. The *stepping-helix* propagator includes all of the magnetic field and material effects treatment internally.

3.4.1 Analytic

A constant magnetic field aligned with the z-axis is assumed. Sensors, or other tracker hardware, can be represented by a set of thin layers with nothing in between. The trajectory state from a layer is extrapolated to the

next layer, and material effects are introduced at end-points only, which is appropriate for the layered tracker volume. The *analytic* propagator is not used in recent CMSSW releases and has been replaced by the *Runge-Kutta* propagator.

3.4.2 Runge-Kutta

High precision extrapolation in a varying B field requires a numerical method. The trajectory state is updated by choosing a boundary surface and propagating the current trajectory state to the chosen surface and introducing material effects. For the Runge-Kutta propagator, non-uniformities in the magnetic field are accounted for by solving the equation of motion in between the final points using the fourth order Runge-Kutta method.

3.4.3 Stepping helix

The *stepping-helix* propagator provides a solution to the muon transport[1)] using steps of finite helix length with parameters updated after each step. Each step includes an update with magnetic field and material effect values at a middle-point, which is equivalent to the second order (helicoidal) Runge-Kutta method. Since each (sub)step is analytically a helix the precision of this propagation method in non-highly-nonuniform magnetic fields is better than a simple second order Runge-Kutta method with polynomial approximation of the trajectory. Except for the tracker volume where the propagation goes in 10 cm steps the propagation proceeds in 5 cm steps as long as no material or magnetic volume boundary is crossed or the destination condition is reached. The propagator stops at each material and magnetic volume boundary. In addition to the destination conditions defined by an intersection with a surface provided by the public interface of the base `Propagator` class the *stepping-helix* propagator can provide a propagation to a fixed path length and to the point of closest approach to a point or a line. The direction of propagation can be a predetermined direction along or opposite to momentum or be left to the propagator to choose internally based on the closest distance to the destination.

Detector material and navigation is based on the internal model which represents an approximated description of the CMS detector volumes. The silicon tracker volume is modeled as several volumes with diffuse (constant) material density. Similarly the calorimeters, the solenoid volume, and the yoke and chamber volumes of the muon end-cap are represented as several volumes with constant material density. The model of material volumes in the region of barrel muon detectors relies on the description provided by the magnetic field model: each magnetic (iron, magnet yoke) and non-magnetic (air, chambers, gas, etc.) volume boundaries are taken from the magnetic field volume description. Every magnetic volume is identified from values of the magnetic field[2)] reported in three points along z at the center and $1/5$th away from the edges: if the field is above 0.6 T at each point the volume is considered to be a solid iron. If the volume is not magnetic it is treated as a chamber volume with a constant density corresponding to an average density in the volume (5.3% of iron density).

Material effects accounted for during the transport are the energy loss contributing to the expected state transport, and multiple scattering and energy loss fluctuations contributing to the propagation of the state covariance matrix.[3)] The energy loss values and its dependence on muon momentum correspond to the restricted mean energy loss reported in [6] for iron. The values reported in the energy loss table for iron are fit by a single function which gives about 5% precision along the momentum range of muons expected from the LHC:

$$\mathrm{d}E/\mathrm{d}x = -(11.4 + 0.96 * |\ln 2.8p| + 0.033p(1 - p^{-1/3}))\ \mathrm{MeV/cm}.$$

Energy loss in every non-iron volume is represented as a fraction of energy loss in iron. The fluctuations in energy loss (a squared uncertainty on the momentum) at each step is incremented by $(\Delta E)^2/x(1 + p \cdot 10^{-3})$, where ΔE is the energy loss (in GeV/c) within that step. This roughly corresponds to the expected smearing of momentum observed in simulation after crossing a fair amount of material (on the order of 1 m of iron-equivalent). The multiple scattering effects are accounted for based on the material radiation length and the value of muon momentum using formula provided in [6]:

$$\theta_0 = \frac{13.6\ \mathrm{MeV}}{p}\sqrt{x/X_0}(1 + 0.38\ln(x/X_0)).$$

1) Unlike the other two propagators the covariance matrix is internally updated in a 6×6 form.

2) It is anticipated that the volume-based magnetic field software will be able to identify a magnetic volume by a corresponding flag which can be used instead of the less precise method described here.

3) Note that the fluctuations from the multiple scattering and the energy loss are **added** to the covariance matrix independent of the propagation direction.

To preserve this dependence along multiple (internal) steps the propagator keeps track of the integrated path length in units of radiation length. Similar to energy loss, accounting the material radiation length used to describe multiple scattering is based on values relative to that of iron.

The material description provided by the *stepping helix* propagator is adjusted and tested to give unbiased width-1 normalized residuals (pulls) of propagated position vs. the simulated final state position (determined by GEANT and stored in `RecHits`). From the performed tests the widths of the pull distributions are within 10% from unity while the mean value is typically much closer to zero (compared to the deviation of width from unity). Based on the same tests, a propagation of a muon successively through all the detectors with hits belonging to the muon takes 3-4 ms on a 2.8 GHz Pentium 4 processor.

4 Muon Reconstruction in the Muon Spectrometer

Based on the Kalman filter technique (cf. [5]), track reconstruction starts with the estimation of the seed state from track segments in the off-line reconstruction (Section 4.1) and from the trajectory parameters estimated by the Level-1 trigger in the on-line. The track is then extended using an iterative algorithm which updates the trajectory parameters at each step and, in order to reduce the possible bias from the seed, a pre-filter can be applied before the final filter (Section 4.2). Once the hits are fitted and the fake trajectories removed, the remaining tracks are extrapolated to the point of closest approach to the beam line. In order to improve the p_{T} resolution a beam-spot constraint is applied.

The track reconstruction handles the DT, CSC and RPC reconstructed segment/hits and it can be configured in such a way as to exclude the measurements from one or more muon subsystems. The independence from the subsystem from which the measurements come is achieved thanks to a generic interface also shared with the inner tracking system. This allows the *tracker* and the *muon* code to use the same tracking tools (such as the Kalman filter) and the same track parametrization.

4.1 Seed Generator

The algorithm is based on the DT and CSC segments (Section 2.1).

A pattern of segments in the stations is searched for, using a rough geometrical criteria. Once a pattern of segments has been found (it may also consist of just one segment), the p_{T} of the seed candidate is estimated using parametrisations of the form:

$$p_{\mathrm{T}} = A - \frac{B}{\Delta\phi} \tag{3}$$

For DT seed candidates with segments in MB1 or MB2, $\Delta\phi$ is the bending angle of the segment with respect to the vertex direction. This part of the algorithm assumes the muon has been produced at the interaction point. If segments from both MB1 and MB2 exist, the weighted mean of the estimated p_{T}'s is taken. If the seed candidate only has segments in MB3 and MB4, the difference in bending angle between the segments in the two stations is used to calculate p_{T}.

In the CSC and overlap region, the seed candidates are built with a pair of segments in either the first and second stations or the first and third stations. $\Delta\phi$ is the difference in ϕ position between the two segments. Otherwise, the direction of the highest quality segment is used.

Although this algorithm is currently used only for the off-line seeding, it can also be used for very fast muon reconstruction, and could be used in the High-Level Trigger (HLT) chain as an intermediate step between L1 and L2.

4.2 Pattern Recognition

In the standard configuration the seed trajectory state parameters are propagated to the innermost compatible muon detector layer (the technique to find the compatible layers is described in Section 4.2.1) and a pre-filter is applied in the inside-out direction. Its main purpose is to refine the seed state before the true filter. The final filter in the outside-in direction is then applied and the trajectory built. The algorithm is flexible enough to perform the reconstruction starting from the outermost layer instead of the innermost. The pre-filter step can optionally be skipped, hence increasing the speed of the reconstruction which could be important for the HLT. However, the standard reconstruction can already meet the strict HLT speed requirement.

The pre-filter and filter are based on the same iterative algorithm used in two different configurations. In both cases it can be subdivided into different sub-steps: search of the next compatible layer (cf. Section 4.2.1) and propagation of the track parameters to it, best measurement finding and possibly update of the trajectory parameters with the information from the measurement. The process stops when the outermost, (for the pre-filter), or the innermost, (for the filter), compatible layer of muon detectors is reached.

At each step the track parameters are propagated from one layer of muon detectors to the next. This process correctly includes material effects like multiple scattering and energy losses due to ionisation and bremsstrahlung in the muon chambers and return yoke. This propagation is also optimized for speed. The trajectory is extrapolated in sequential steps using helix parametrisations. The required precision is obtained by using smaller steps in regions with larger magnetic field inhomogeneities. Multiple scattering and energy losses in each step are estimated from fast parametrisations, avoiding time-consuming accesses to the detailed material and geometry descriptions. The resulting propagated state contains these effects in its parameters and errors.

The best measurement is searched for on a χ^2 basis. The χ^2 compatibility is examined at the segment level, estimating the incremental χ^2 given by the inclusion in the fit of the track segment. In case no matching hits (or segments) are found, the search continues in the next station.

4.2.1 Navigation in the Muon Detector

The track fitting method described in the previous sections does not require the full set of reconstructed hits to be available before the fit. Instead, at each step the track parameters are used to identify the detectors that most probably contain the next hit to be included in the trajectory.

The algorithmic problem of finding the next detector crossed by one trajectory, given its parameters at a given point, is called *navigation*. The efficiency and speed of this operation are fundamental: the navigation is one of the most time consuming parts of the track fit, and a fast implementation is necessary to allow track reconstruction within the timing constraints of the trigger.

The possibility of an optimised implementation derives from the fact that the tracking detectors in CMS are arranged in layers with a defined distance from the detector centre, so that a track coming from the interaction point always crosses them in a defined sequence. Moreover, individual detectors within the layers are arranged in a (quasi-) periodic way, and can be organised in sub-structures with a simple geometrical shape, like disks or rods.

The problem of navigation is therefore solved by organising the detectors in a hierarchical structure. Each element in the hierarchy is described geometrically in terms of an elementary surface that approximates the surface of its constituents (detectors or groups of detectors). The element can be queried to find which detectors are compatible with a given trajectory; in this case, the trajectory is extrapolated to the surface of the element and compatible constituents are selected taking into account the uncertainty on the extrapolated track position. Selected constituents are queried in the same way, so that the hierarchy is traversed vertically, up to the level of individual detectors. As a result, the reconstructed hits are returned together with the trajectory state extrapolated to the corresponding detector surface. Both the reconstructed hits and the state are directly used for the Kalman filter update step described in the previous section. This procedure minimises the number of track extrapolations, especially in the case of extrapolations between stations in the muon system where the trajectory crosses the iron return yoke. These constitute the time-consuming part of the navigation.

The CMS software provides a framework and a set of base classes for the implementation of these hierarchies. Such classes are shared by all tracking detectors, to allow a consistent behaviour. Navigation in each detector system is implemented by specialising these classes, i.e. grouping the detectors in the optimal way and defining the rules to determine how the search is performed within each hierarchy level. The case of the muon system is described in the following.

The first level of the hierarchy is a full layer of detectors; in the barrel muon system it consists of a cylinder, corresponding to either one DT or one RPC station. In the endcap, layers are flat vertical disks corresponding to either one CSC or one RPC station, except for the first station (ME1), which is split into two layers at different positions in z (cf. Fig. 1). Layers are sorted by their distance from the detector centre (i.e. by radius in the barrel and by z in the endcaps). This is the order in which they are traversed by a trajectory coming from the interaction point, so that, at each fitting step, reconstructed hits are looked for in the next layer in the list (provided that the track direction with its error is within the layer's η boundaries.)

Inside these layers, detectors are organised in groups with a common surface. Since an extrapolation to each detector surface is needed to test the compatibility with a track, the most efficient organisation is obtained when

individual detectors with a common surface are grouped together. The organisation is different for the barrel and the endcaps.

Muon barrel layers. From the mechanical point of view, the muon barrel is composed of five wheels of 12 or 14 chambers each. However, as discussed above, it is preferable to have chambers with the same flat surface grouped together. For this reason, barrel muon layers are constituted of rods, each consisting of five chambers. There are 12 rods in each layer, except for MB4, where there are 14. Chambers in a rod lie on the same plane, are contiguous in z and are all at the same r and ϕ coordinates. Rods in a layer are quasi-periodic in ϕ and, in some cases, slightly overlap in this coordinate.

When a layer is queried for the reconstructed hits compatible with a given track, a first extrapolation is done to the cylinder representing the layer's surface. The extrapolated position in ϕ is used to determine the closest rod, which is selected. If the extrapolated error, scaled by an adjustable factor, extends beyond the rod's border in ϕ, the neighbouring rods are selected as well. Then, selected rods are individually queried for compatible chambers. A short extrapolation is made from the layer's cylinder to the rod plane, and one or more chambers are selected according to the z position of the extrapolated track and its uncertainty.

Muon endcap layers. Endcap layers are organised in rings of chambers. All chambers in one ring are located at the same r and are periodic in ϕ. In all endcap layers, with the exception of ME1/3 CSCs, the chambers in a ring are staggered in z. In this case, the ring's nominal surface is a flat disk placed between the two planes of chambers.

When the layer is queried for the measurements compatible with a track, a first extrapolation is made to the plane representing the layer's surface. The radius of the extrapolated position is used to determine the closest disk, which is selected. If the extrapolated error, scaled by an adjustable factor, extends beyond the disk's border in r, the neighbouring disks are selected as well. Then, selected disks are individually queried for compatible chambers. This is done using the ϕ coordinate and the uncertainty of the previously extrapolated state. In the case of staggered chambers in a disk, one more short extrapolation from the ring's central surface to the surface of each chamber is needed to obtain the state on the detector surface as required by the track fitting procedure.

4.2.2 Trajectory Building

For the update of the trajectory parameters the pre-filter and the filter follow two different approaches. As the pre-filter should give only a first estimate of the track parameters, it uses the segment for the fit. The parameters are almost always updated as the χ^2 cut imposed at this stage is loose (of the order of one hundred). The final filter instead uses the hits composing the segment with a tighter χ^2 cut (of the order of 25) which can reject individual hits. This results in a more refined trajectory state. The RPC measurements are not aggregated in segments, so that for them the only distinction between the pre-filter and the filter is the χ^2 cut.

The mechanism for updating the trajectory parameters can be seen as a combination of the predicted trajectory state and the hit in a weighted mean, as the weights attributed to the measurement and to the predicted trajectory state depend on the respective uncertainties. A more detailed explanation is given in [3, 4].

In order to finally accept a trajectory as a muon track, at least two measurements, one of which must be of the DT or CSC type, must be present in the fit. This allows rejection of fake DT/CSC segments due to combinatorics. Moreover the inclusion of the RPC measurements can improve the reconstruction of low momentum muons and those muons which escaped through the inter-space between the wheels (and the DT sectors), leaving hits in only one DT/CSC station. In Fig. 4 the effect of the inclusion of the RPC measurements in the track fitting is shown.

4.3 Stand-Alone Muon Track

After the fake track suppression the parameters are extrapolated to the point of closest approach to the beam line. In order to improve the momentum resolution a constraint to the nominal interaction point (IP) is imposed. The matrix error of the IP is diagonal and its values are: (15 μm 15 μm 5.3 cm).

5 Global Muon Reconstruction in the CMS Detector

The ability to reconstruct muons over a wide range of energies and in the whole geometric acceptance of the detector is central to the proper recognition of physics signatures at the LHC. The CMS detector is designed

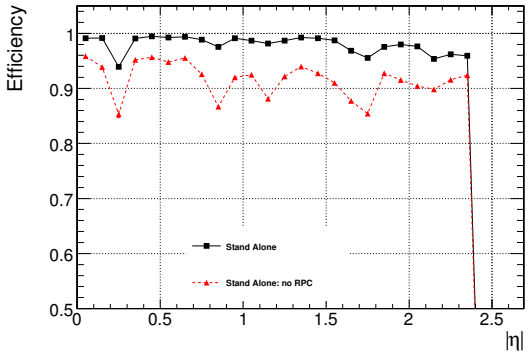

(a) Efficiency as a function of pseudorapidity.

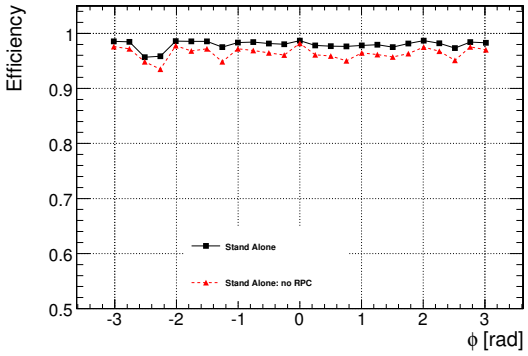

(b) Efficiency as a function of ϕ.

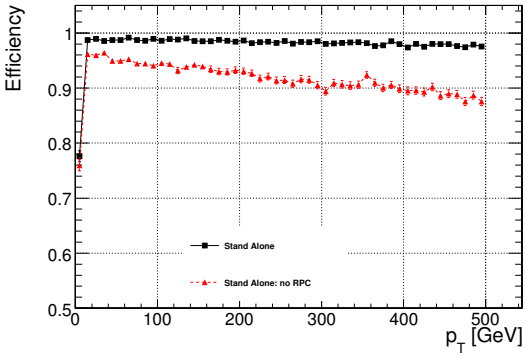

(c) Efficiency as a function of p_{T}.

Figure 4: Efficiency of the reconstruction in the muon spectrometer as a function of η, ϕ and p_{T}, with (black square) and without (red triangle) the inclusion of RPC in the track reconstruction.

to meet these requirements by using several different types of sub-detectors with different and complementary capabilities. While each sub-detector is able to measure a part of a muon's properties, the concept of a global muon is to combine information from multiple sub-detectors in order to obtain a more accurate description of the muon. The muon's track parameters are measured in two sub-detectors: the inner tracker, and the muon system. The reconstruction of tracks in the silicon tracker is described in [3], while the reconstruction of tracks in the muon system is described in Section 4. As described in Section 4, the momentum resolution of muon tracks up to $p_{\mathrm{T}} = 200\mathrm{GeV}/c$ reconstructed in the muon system alone is dominated by multiple scattering. At low momentum, the best momentum resolution for muons is obtained from the silicon tracker. At higher momentum, however, the characteristics of the muon system allow the improvement of the muon momentum resolution by combining the muon track from the silicon detector, *tracker track*, with the muon track from the muon system, *stand-alone muon*, into a global muon track. The reconstruction of global muon tracks begins after the completion of the reconstruction of the central tracker tracks and the muon system tracks.

5.1 Matching Tracker Tracks to Stand-Alone Muon Tracks

The first step in reconstructing a global muon track is to identify the silicon tracker track to combine with the stand-alone muon track. This process of choosing tracker tracks to combine with stand-alone muon tracks is referred to as *track matching*. The large multiplicity of tracks in the central tracker necessitates the selection of a subset of tracker tracks that roughly correspond in momentum and position to the stand-alone muon track. The method of track matching proceeds in two steps. The first step of the track matching process is to define a region of interest that is rectangular in $\eta - \phi$ space, and to select a subset of tracker tracks that are in this tracking region of interest. The second step is to iterate over the subset of tracker tracks, applying more stringent spatial and momentum matching criteria to choose the best tracker track to combine with the stand-alone muon.

5.1.1 Tracking Region of Interest

In the case of global muon reconstruction, we use a rectangular eta-phi tracking region to choose the initial set of tracker tracks that roughly correspond to the stand-alone muon track. The definition of the region of interest has a strong impact on the reconstruction efficiency, fake rate, and CPU reconstruction time. A rectangular eta-phi tracking region is defined with a set of seven parameters:

- Origin: the origin position of the tracking region - usually taken to be near the interaction point
- ΔZ: the allowed z spread for the region origin
- ΔR: the allowed r spread for the region origin
- Direction: vector giving the direction from the *origin* around which the tracking region will be opened
- $\Delta\phi$: the ϕ size of the tracking region
- $\Delta\eta$: the η size of the tracking region
- min p_{T}: the minimum p_{T} of tracks in the tracking region - used to determine the curvature of the tracking region

The origin is chosen to be the primary vertex as defined by the pixel vertexing algorithm [7], or the beam spot if the pixel vertex is not known. ΔZ is defined by the pixel vertex, or is chosen to be a fixed value if the beam spot is used as the origin. ΔR is a fixed value chosen by our knowledge of the detector. We use the stand-alone muon track updated at the vertex to define the other parameters of the tracking region of interest. The direction and minimum p_{T} are taken as the direction of the stand-alone muon track and as 60% of the stand-alone muon p_{T}, respectively. The values for $\Delta\eta$ and $\Delta\phi$ are extracted from the error estimates of the stand-alone muon direction, with certain minimum and maximum values to constrain the tracking region to be of reasonable size.

With the tracking region of interest defined around the stand-alone muon, the matching algorithm iterates over all reconstructed tracker tracks and chooses a subset of tracks that are within this region. The collection of regional tracker tracks are then compared to the stand-alone muon track using more stringent matching criteria.

5.1.2 Track Matching Methods

The matching of two disjoint tracks is performed by comparing the 5 parameters describing the trajectory, this is best done by propagating the tracks onto a common reference point or surface; the choice of a surface constraint provides one more degree of freedom on the fit as opposed to a point constraint, and it is therefore better at incorporating random scattering effects. We will describe the surfaces considered in track matching and the combination of variables used to select the best match.

Common matching surface The two competing objectives that determine the choice of the common surface for track propagation (and matching) are choosing the plane that (1) minimizes the covariant error matrix of the propagated track parameters and (2) reduces the number of matches per stand-alone muon. It is possible to attempt to propagate the tracker track and stand-alone muon track to any common plane, but it is natural to choose a plane that does not require the track to be propagated through a lot of a material. Some of the natural choices for a common surface are the tracker system outer boundary, the muon system inner boundary, the detector surface of the outermost tracker track hit, and the detector surface of the innermost muon track hit. Propagating the tracks to the tracker or muon system boundaries requires that both tracks be propagated with subsequent enlargement of both error matrices. Another difficulty arises when propagating the tracks to the cylinder surface representing the boundaries of the barrel region because each trajectory-state-on-surface is actually defined on a plane *tangent* to the cylinder at that point. If the trajectory-states are separated in ϕ, then the trajectory-states will be on different planes and it is improper to attempt to compare their local parameters on a plane. Fig. 6 and Fig. 7 shows the error ellipses of the stand-alone muon track and tracker track respectively when propagated to the detector surface of the inner (outer) hit of the stand-alone muon track (tracker track) starting from the muon (tracker) hit surface or the interaction point. For low momentum ($p_{\mathrm{T}} = 10\mathrm{GeV}/c$) multiple scattering dominates on the precision of the errors, thus a gain in precision is made when propagating from the interaction point to the tracker hit surface since there is less material. For high momentum ($p_{\mathrm{T}} = 100\mathrm{GeV}/c$) the local errors at the muon hit surface become more sensible. After discussing the matching algorithm, we will consider the number of fakes at a given surface.

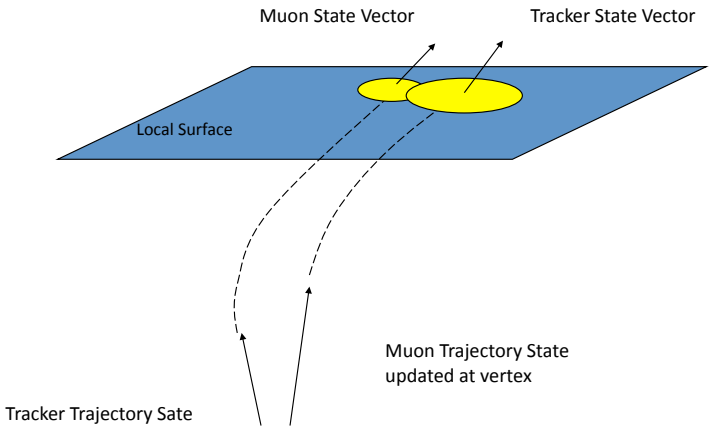

Figure 5: Illustration of matching the error matrix of two trajectory states on a common surface.

Discriminating variables Once the tracks are propagated to the common surface, a comparison of the track parameters is made using the tracks' position and momentum. Comparing the momentum parameters provides the best match for low-p_{T} tracks, while the spatial coordinates gives the best match to the high-p_{T} candidate.

The choices of discriminating variables are, given the 5 parameter space $\vec{p_i}$ = {q/$|P|$,x,y,x‘,y‘}:

1. Compare all 5 parameters by doing a χ^2 similarity comparison involving their covariance matrices of the propagated tracks (C_i)
$$\chi^2 = (\vec{p_1} - \vec{p_2})^T [C_1 + C_2]^{-1} (\vec{p_1} - \vec{p_2})$$

2. Compare the track positions on the plane in coordinates local to the plane ($\vec{d}$ = {x,y})
$$d = \sqrt{(x_1 - x_2)^2 + (y_1 - y_2)^2}$$

3. Compare the local position parameters by doing a local χ^2 similarity comparison involving their local covariance matrices of the propagated tracks (C_{di})
$$\chi^2 = (\vec{d_1} - \vec{d_2})^T [C_{d1} + C_{d2}]^{-1} (\vec{d_1} - \vec{d_2})$$

4. Compare of the track positions in $\eta - \phi$ space using the *position* vector at the surface
$$\Delta R = \sqrt{(\eta_1 - \eta_2)^2 + (\phi_1 - \phi_2)^2}$$

5. Compare of the track direction in $\eta - \phi$ space using the *momentum* vector defined at the primary vertex
$$\Delta R_{IP} = \sqrt{(\eta_1^{mom} - \eta_2^{mom})^2 + (\phi_1^{mom} - \phi_2^{mom})^2}$$

The current matching algorithm loops over all track candidates for the given matching variables in the order described, except the local χ^2 is not currently implemented. If no match is found based on certain cuts on the distributions at the innermost muon hit surface, then the best pick is chosen based on a loose cut on the directions at the interaction point.

To study the behavior of the various matching quantities and the effect of misalignment on the matching algorithm, the matching algorithm was performed on various sets of data of simulated physics processes. These matching

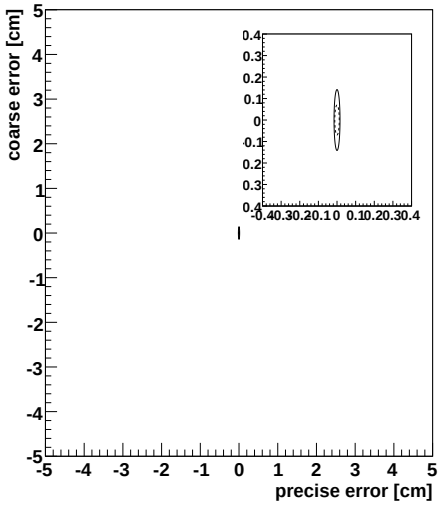

(a) stand-alone local errors on the barrel ($|\eta| = 0$) for $p_{\mathrm{T}} = 10\mathrm{GeV}/c$ (solid) and $p_{\mathrm{T}} = 100\mathrm{GeV}/c$ (dashed) evaluated at the *innermost muon hit surface*

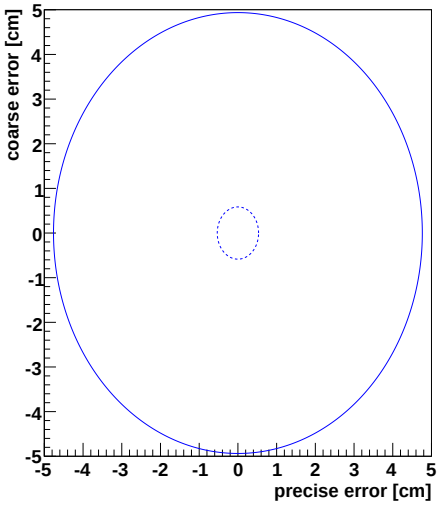

(b) stand-alone local errors on the barrel ($|\eta| = 0$) for $p_{\mathrm{T}} = 10\mathrm{GeV}/c$ (solid) and $p_{\mathrm{T}} = 100\mathrm{GeV}/c$ (dashed) evaluated on the *innermost muon hit surface* from the *interaction point* (right)

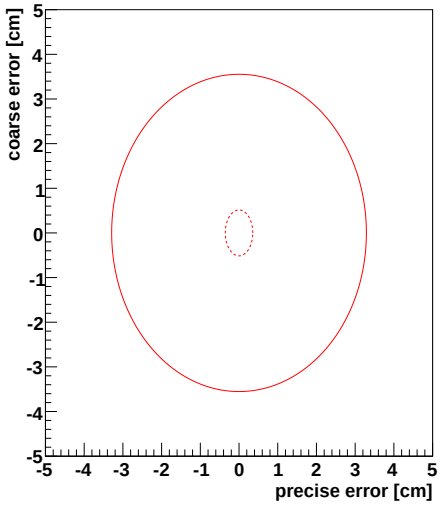

(c) stand-alone local errors on the barrel ($|\eta| = 0$) for $p_{\mathrm{T}} = 10\mathrm{GeV}/c$ (solid) and $p_{\mathrm{T}} = 100\mathrm{GeV}/c$ (dashed) evaluated on the *outermost tracker hit surface* starting from the *muon system*

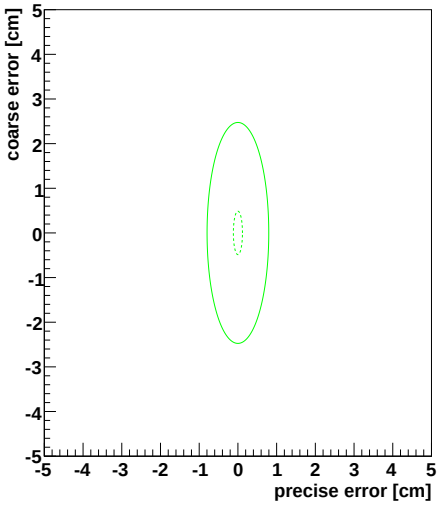

(d) stand-alone local errors on the barrel ($|\eta| = 2.0$) for $p_{\mathrm{T}} = 10\mathrm{GeV}/c$ (solid) and $p_{\mathrm{T}} = 100\mathrm{GeV}/c$ (dashed) evaluated on the *outermost tracker hit surface* starting from the *interaction point*

Figure 6: The error ellipses of the stand-alone muon track when propagated to various detector surfaces

studies were performed on data simulations that would have a high multiplicity of tracks near the simulated muon in order to test the discriminating power of the match quantities. Events with multiple tracks near the true muon provided the ability to compare the match quantites for good track matching and for tracks that were improperly matched. Shown here is the matching performance with a sample of $t\bar{t}$ simulated data.

Fig. 8 shows the independent distributions of the matching variables for good track matches in comparison to the distribution of incorrect matches to tracks inside the region of interest. A cut at d=10 cm arises from the AssociatorByPosition used to select the correct generated particle to the stand-alone muon.

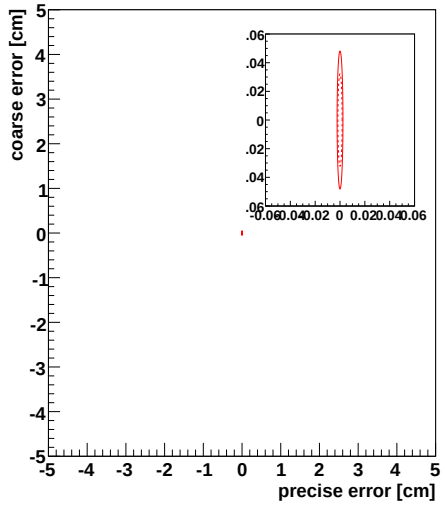

(a) Tracker track local errors on the barrel ($|\eta| = 0$) for $p_{\mathrm{T}} = 10\mathrm{GeV}/c$ (solid) and $p_{\mathrm{T}} = 100\mathrm{GeV}/c$ (dashed) evaluated at the *outermost tracker muon hit surface*

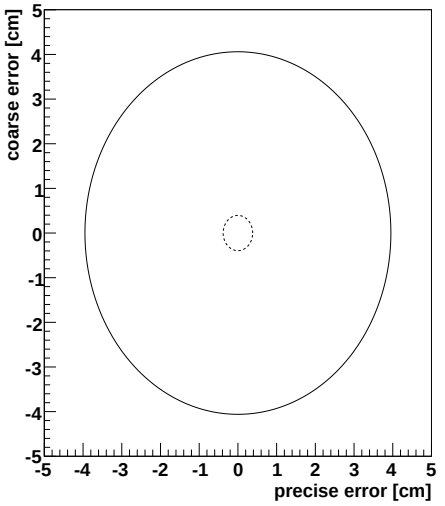

(b) Tracker track local errors on the barrel ($|\eta| = 0$) for $p_{\mathrm{T}} = 10\mathrm{GeV}/c$ (solid) and $p_{\mathrm{T}} = 100\mathrm{GeV}/c$ (dashed) evaluated on the *outermost tracker hit surface* starting from the *muon system*

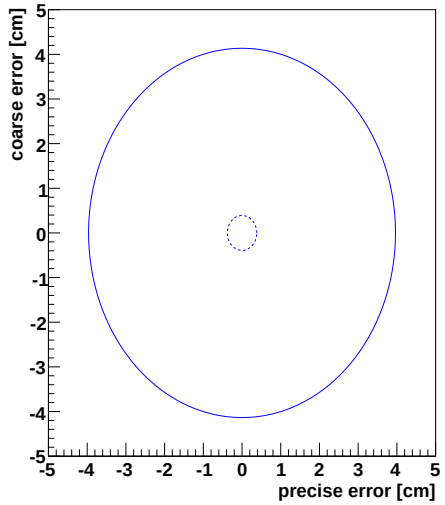

(c) Tracker track local errors on the barrel ($|\eta| = 0$) for $p_{\mathrm{T}} = 10\mathrm{GeV}/c$ (solid) and $p_{\mathrm{T}} = 100\mathrm{GeV}/c$ (dashed) evaluated on the *innermost muon hit surface* from the *interaction point* (right)

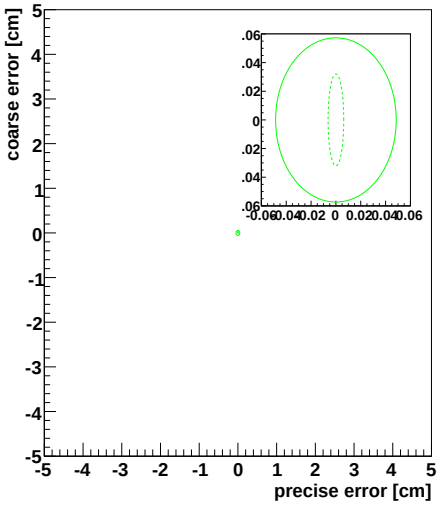

(d) Tracker track local errors on the barrel ($|\eta| = 2.0$) for $p_{\mathrm{T}} = 10\mathrm{GeV}/c$ (solid) and $p_{\mathrm{T}} = 100\mathrm{GeV}/c$ (dashed) evaluated on the *outermost tracker hit surface* starting from the *interaction point*

Figure 7: The error ellipses of the tracker track when propagated to various detector surfaces

Fig. 10 shows the number of matches per stand-alone muon and efficiencies vs p_{T} and η for the innermost-muon hit surface and outermost-tracker hit surface, for the ideal and misaligned cases.

5.1.3 Effects of Misalignment on Track Matching

The misalignment affects track matching in the sense that the local positions of the trajectory-state-on-surface on the muon system are shifted with respect to the local position of the corresponding trajectory-state-on-surface on the tracker system. The greatest alignment uncertainty occurs when the muon system is shifted along the beamline

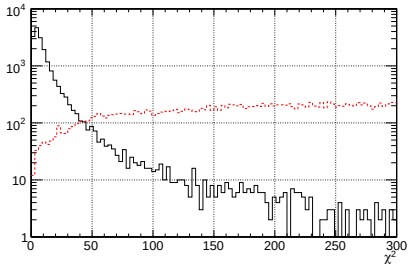

(a) χ^2 distribution at the *innermost muon hit surface*

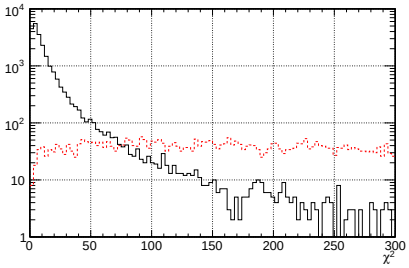

(b) χ^2 distribution at the *outermost tracker hit surface*

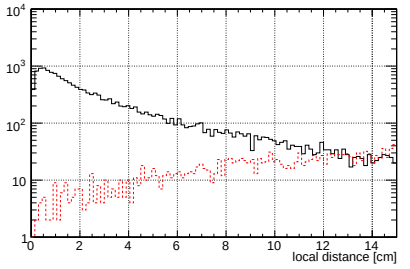

(c) local distance distribution the *innermost muon hit surface*

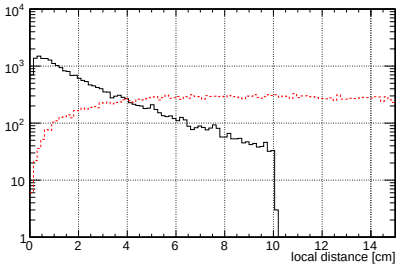

(d) local distance distribution at the *outermost tracker hit surface*

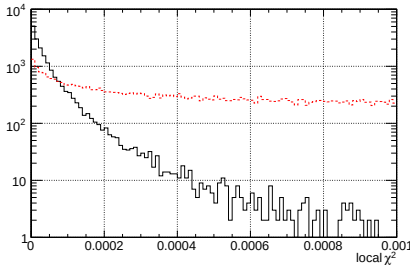

(e) local χ^2 distribution at the *innermost muon hit surface*

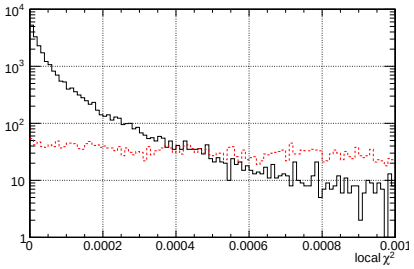

(f) local χ^2 distribution at the *outermost tracker hit surface*

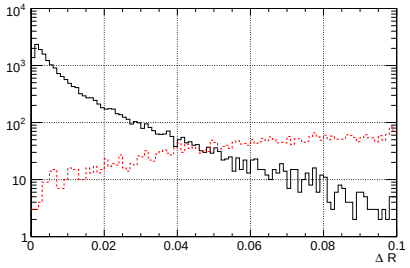

(g) ΔR distribution at the *innermost muon hit surface*

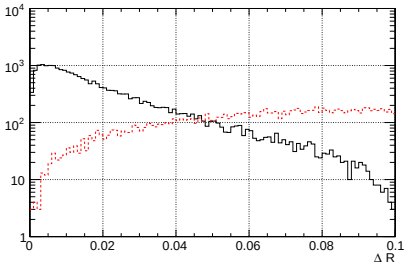

(h) ΔR distribution at the *outermost tracker hit surface*

Figure 8: Distributions of matching variables for *correct* matches (black) and *incorrect* matches (dashed) with a $t\bar{t}$ sample

with respect to the tracker system. For the purposes of placing the muon track matching through an extensive

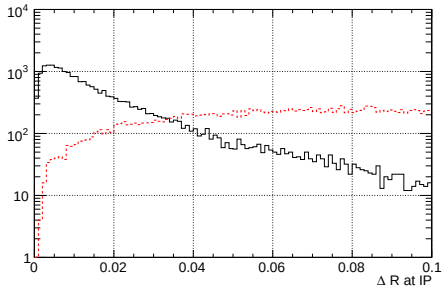

Figure 9: ΔR at the *Interaction Point* for a $t\bar{t}$ sample for *correct* matches (black) and *incorrect* matches (dashed).

stress test, in this section we have misaligned the muon system geometry with an uncertainty of $\Delta z \approx 1$ cm. This $\Delta z \approx 1$cm misalignment is roughly 5 times the expected uncertainty at the start up of the CMS detector. This unrealistic misalignment is meant to help us understand the robustness of the muon track matching algorithm, and it is not meant as a reflection of real running conditions.

Fig. 11 to Fig. 14 shows the single muon distributions of the matching variable in the *ideal* case, compared to the *misaligned* scenario of $\Delta z \approx 1$ cm for both innermost-track hit surface and outermost-muon hit surface. The distributions are quite robust for low momentum, only for high momentum ($p_{\mathrm{T}} \geq 100$GeV/c) does the χ^2 distribution becomes degraded, this is also true for the local distance distribution to a lesser extent. The Muon hit surface is more stable to compute the difference in the direction in $\eta - \phi$ compared to the tracker hit surface. It is worth noting that the local χ^2 distribution remains invariant due to misalignment since it takes into account the misalignment errors.

5.2 Global Refit of Silicon Hits and Muon Hits

After the selection of a subset of tracker tracks that match the stand-alone muon track, the next step in making a global muon track is to fit a track using the hits from the tracker track and the stand-alone muon track. The global refit algorithm attempts to perform a track fit for each tracker track - stand-alone muon pair. If, after the fit is attempted for each pair, there is more than one possible global muon track, the global muon track with the best χ^2 is chosen. Thus, for each stand-alone muon there is a maximum of one global muon that will be reconstructed.

5.2.1 Selecting Muon Hits

Since the pattern recognition of selecting appropriate hits has already been performed during the reconstruction of the tracker track and stand-alone muon track, there is no additional pattern recognition to be done for the global muon track fit. The default global muon algorithm simply combines the collection of tracker hits corresponding to the chosen tracker track with the collection of muon hits corresponding to the stand-alone muon track. However it is also possible to combine only a subset of the hits for the global fit. Choosing a subset of the muon hits provides a better reconstruction resolution for high energy muons, when the measurements in the muon system are frequently contaminated by electromagnetic showers. The treatment of very energetic muons will be described in Section 5.4.

In the following paragraphs, we will describe the dependence of the momentum resolution of the global refit when different numbers of hits from the tracker and stand-alone muon tracks are included.

5.2.2 Momentum Resolution vs Momentum

The minimum momentum can be estimated based on the geometry of the muon stations and the minimum radius of curvature to reach these stations. At this energy, the muon is a minimum ionizing particle, thus the energy loss due to ionization is of the order $\frac{dE}{dx} \cdot \Delta X \approx 2 - 3$ GeV/c, where $\Delta X = (120 - 160) X_o$ to the first muon station as shown in fig. Fig. 16; taking an estimate $X_o \approx$ 10-15 $[g/cm^2]$ Table 2 shows the minimum p and p_{T} values needed to reach the first muon station with the corresponding η regions.

The contribution due to multiple scattering adds a *constant* component to the resolution curves vs momentum, this appears below 100 GeV/c for the Muon system and below 50 GeV/c for the Tracker Simple calculation for the magnitude shows that for the *muon system* (excluding the tracker region) with $L/X_o = 220$, and average of $\mathbf{B} = 2$ T and $L = (7 - 1)$m we expect a momentum resolution of 5%, which is within 20% of what is seen; recalling that

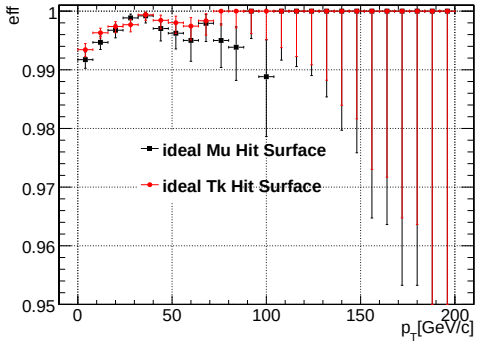

(a) Matching efficiency vs p_{T} under an ideal case for a $t\bar{t}$ sample

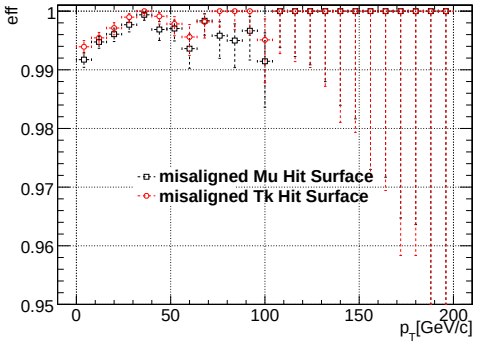

(b) Matching efficiency vs p_{T} under a misaligned case for a $t\bar{t}$ sample

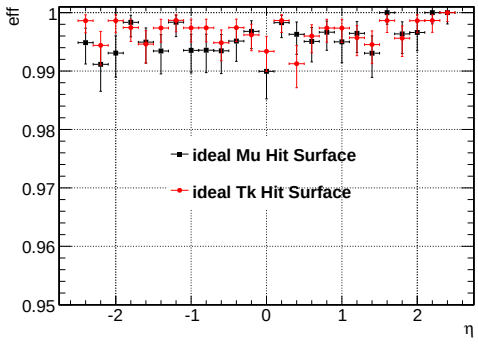

(c) Matching efficiency vs η under an ideal case for a $t\bar{t}$ sample

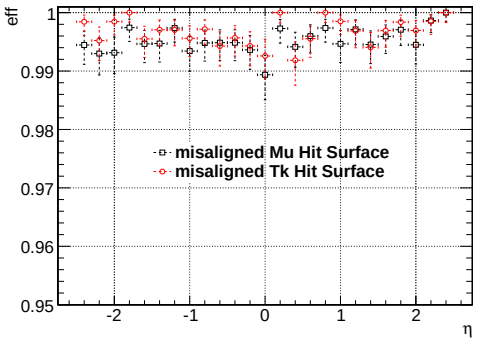

(d) Matching efficiency vs η under a misaligned case for a $t\bar{t}$ sample

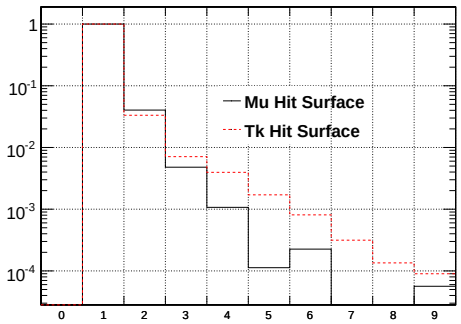

(e) Number of matches per stand-alone for a $t\bar{t}$ sample (normalized)

Figure 10: Matching Efficiencies vs p_{T} and η for ideal and misaligned scenarios, also shown is the track directions compared at the interaction point for *correct* matches (solid) and *incorrect* matches (dashed)

the formula used is accurate within 11% for $L/X_o \leq 100$. For the *tracker system* $L/X_o \cong 0.5$ and uniform $\mathbf{B} = 4$ T and $L = 1$m we expect a momentum resolution of 0.9%, this is roughly what is seen.

At higher momenta the *intrinsic* resolution due to the finite measurements, becomes significant. This resolution is proportional to the momentum, and shows up in the tracker above 50 GeV/c, and later becomes of the same order of magnitude in the Muon system at 2 TeV in the barrel. This effect occurs in the muon system later in momenta

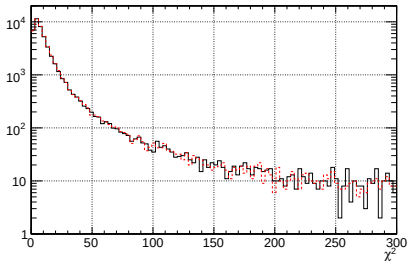

(a) χ^2 distribution at the *innermost muon hit surface*

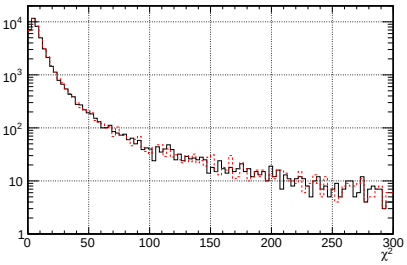

(b) χ^2 distribution at the *outermost tracker hit surface*

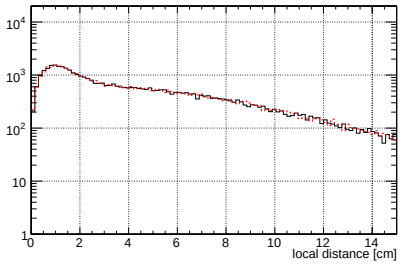

(c) local distance distribution the *innermost muon hit surface*

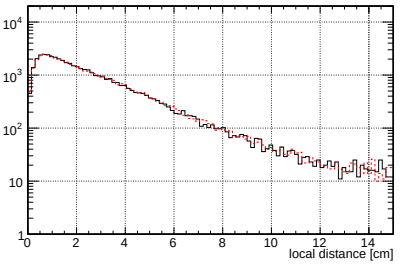

(d) local distance distribution at the *outermost tracker hit surface*

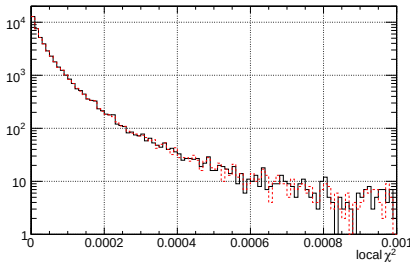

(e) local χ^2 distribution at the *innermost muon hit surface*

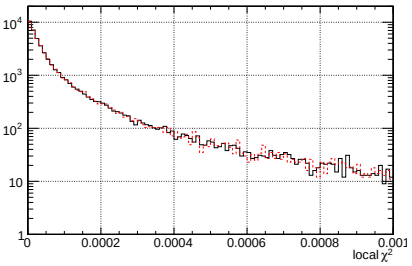

(f) local χ^2 distribution at the *outermost tracker hit surface*

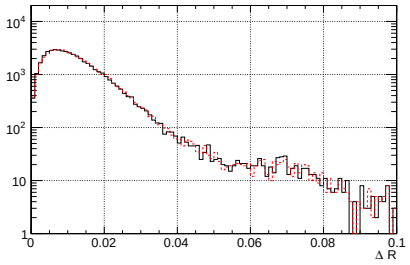

(g) ΔR distribution at the *innermost muon hit surface*

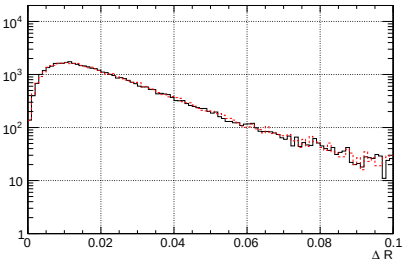

(h) ΔR distribution at the *outermost tracker hit surface*

Figure 11: Single muon ($p_{\mathrm{T}} = 10\mathrm{GeV}/c$) matching variables distributions for ideal (solid line) and misaligned (dashed line) scenario of $\Delta z \approx 1\mathrm{cm}$

because of the larger amount of material of an additional 60 radiation lengths in the end-caps and somewhat less in the overlap (see fig. Fig. 16).

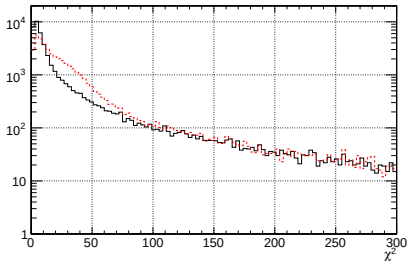

(a) χ^2 distribution at the *innermost muon hit surface*

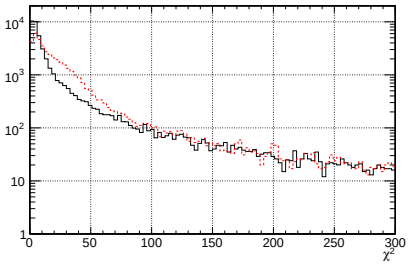

(b) χ^2 distribution at the *outermost tracker hit surface*

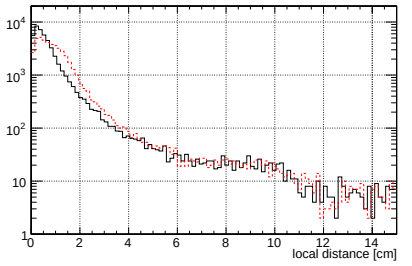

(c) local distance distribution the *innermost muon hit surface*

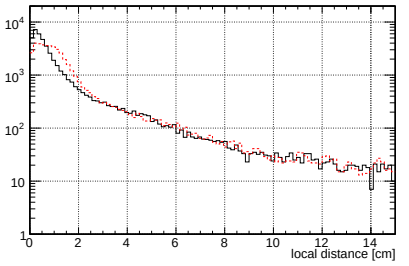

(d) local distance distribution at the *outermost tracker hit surface*

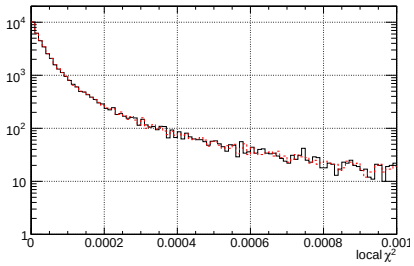

(e) local χ^2 distribution at the *innermost muon hit surface*

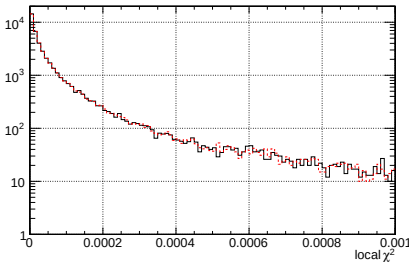

(f) local χ^2 distribution at the *outermost tracker hit surface*

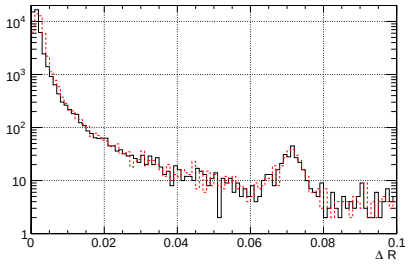

(g) ΔR distribution at the *innermost muon hit surface*

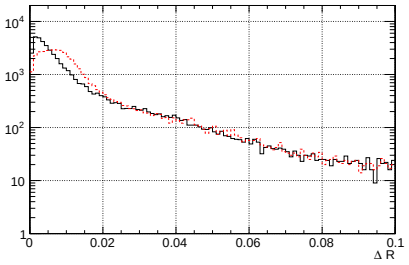

(h) ΔR distribution at the *outermost tracker hit surface*

Figure 12: Single muon ($p_{\mathrm{T}} = 100\mathrm{GeV}/c$) matching variables distributions for ideal (solid line) and misaligned (dashed line) scenario of $\Delta z \approx 1\mathrm{cm}$

The effect of adding one muon hit with very precise resolution has little or not effect on the combined fit for $p_{\mathrm{T}} \geq 1TeV\mathrm{GeV}/c$. The reason has to do with the fact that we update the stand-alone trajectory to originate from

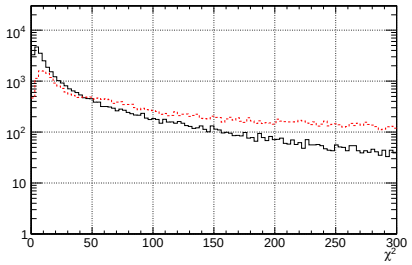

(a) χ^2 distribution at the *innermost muon hit surface*

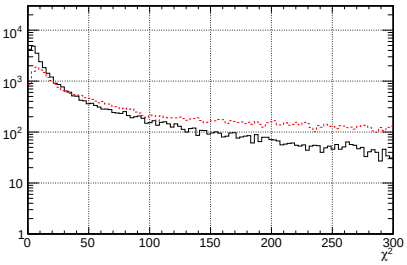

(b) χ^2 distribution at the *outermost tracker hit surface*

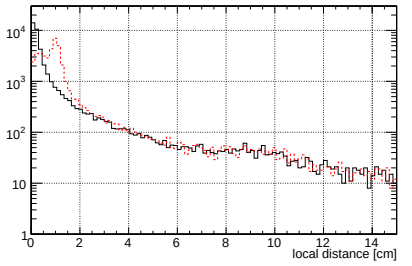

(c) local distance distribution the *innermost muon hit surface*

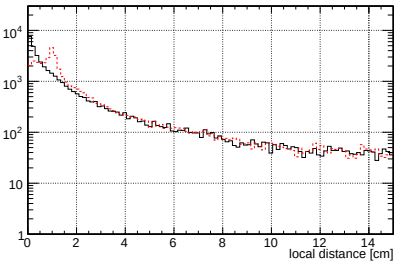

(d) local distance distribution at the *outermost tracker hit surface*

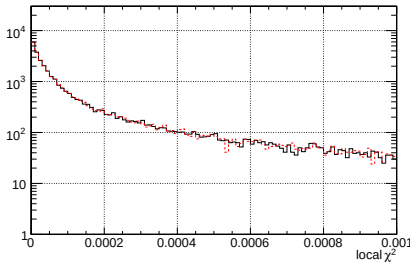

(e) local χ^2 distribution at the *innermost muon hit surface*

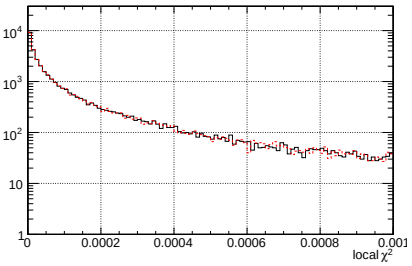

(f) local χ^2 distribution at the *outermost tracker hit surface*

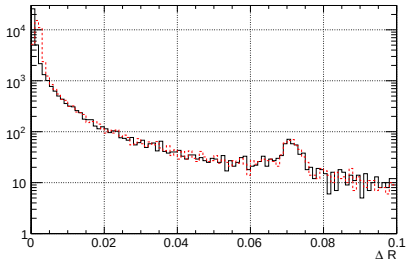

(g) ΔR distribution at the *innermost muon hit surface*

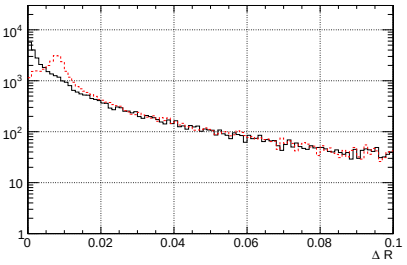

(h) ΔR distribution at the *outermost tracker hit surface*

Figure 13: Single muon ($p_{\mathrm{T}} = 1000\mathrm{GeV}/c$) matching variables distributions for ideal (solid line) and misaligned (dashed line) scenario of $\Delta z \approx 1\mathrm{cm}$

the vertex, so the stand-alone fit and the stand-alone + 1 tracker hit are essentially identical; for TeV muons the

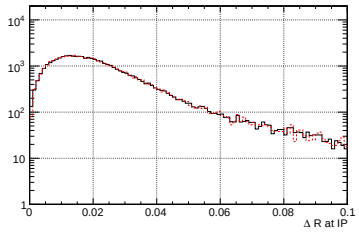

(a) ΔR at the *Interaction Point* for a single Muon sample with p_{T} = 10GeV/c respectively

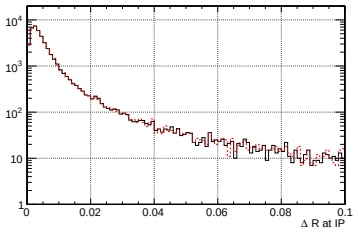

(b) ΔR at the *Interaction Point* for a single Muon sample with p_{T} = 100 GeV/c respectively

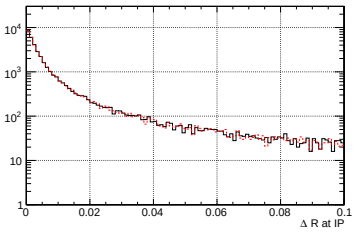

(c) ΔR at the *Interaction Point* for a single Muon sample with p_{T} = 1000 GeV/c respectively

Figure 14: Distributions of the directions at the primary vertex for an *ideal* geometry (solid) and *misaligned* geometry by Δ z $\approx$ 1cm (dashed) for a single Muon sample with p_{T} = $\{$10,100,1000$\}$ GeV/c respectively

Table 2: Minimum p and p_{T} to reach first Muon station

$\eta = -\ln\tan\frac{\theta}{2}$	R_T^{min}	$p_{\mathrm{T}}^{min} = 0.3BR_T^{min}$	$p^{min} = p_{\mathrm{T}}^{min}/\sin\theta$
$0 \leq \lvert\eta\rvert \leq 1.2$	4 m	4.8 GeV/c	4.8-8.7 GeV/c
$1.2 \leq \lvert\eta\rvert \leq 1.5$	3 m	3.6 GeV/c	6.5-8.5 GeV/c $\bigoplus$ $\overbrace{2GeV}^{Loss\ in\ barrel}$ to $\underbrace{3GeV}_{Loss\ on\ endcaps}$
$1.5 \leq \lvert\eta\rvert \leq 2.4$	1 m	1.2 GeV/c	2.8-6.7 GeV/c

precise tracker hit slightly improves the resolution. The resolution as a function of the number of tracker hits added to the muon system is more significant above $p_{\mathrm{T}} \geq 100$GeV/c, where the improvements to the resolution arise because the intrinsic resolution of the muon (+ tracker) system start to become the same order of magnitude as that due to the multiple scattering component.

In Fig. 15 we see the detector resolution for the tracker system and muon system and various combination of their components. We note the following points:

1. The intrinsic detector resolution becomes apparent for momentum $pt \geq 100$GeV/c. Above this momenta, the weight of individual tracker components becomes large enough to separate the stand-alone + 2 track and stand-alone + 3 tracker hits;

2. The muon system affects the overall resolution (full system) when the tracker system renders its precision to the component linear in momentum above $pt \geq 500$GeV/c.

3. The full resolution is alsready reached with one muon station; additional muons hits can improve the resolution for TeV muons if the effect of showers is controlled.

4. The *endcaps* show non-gaussian behavior due to magnetic inhomogeneity and shower effects at high momenta. The effect of non-gaussian tails can be noted from the error on the curves; the central value shown

is obtained from a fit to the $mean \pm 2 \times rms$, while the error assigment is calculated from the difference in the fits to the core and a wider range in order to take into account the tails of the distribution.

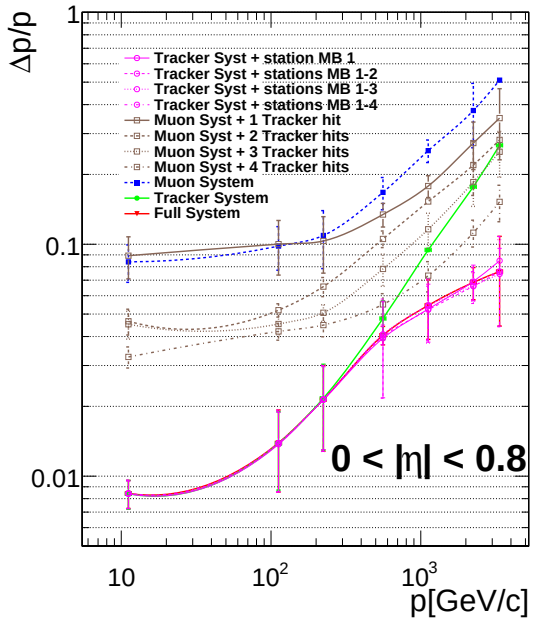

(a) Barrel q/p resulution vs p

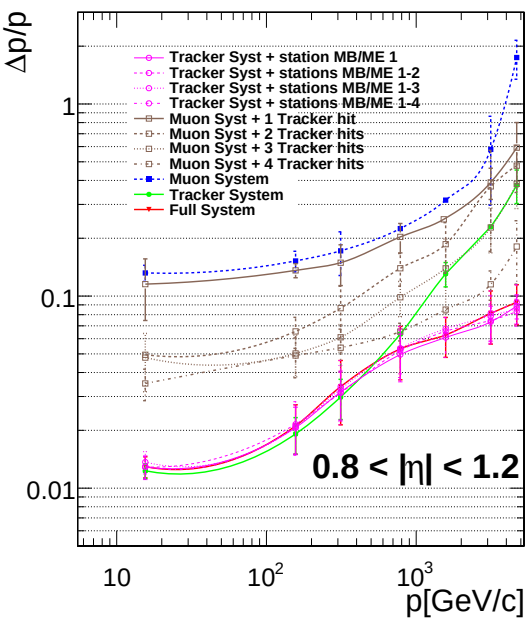

(b) Overlap q/p resulution vs p

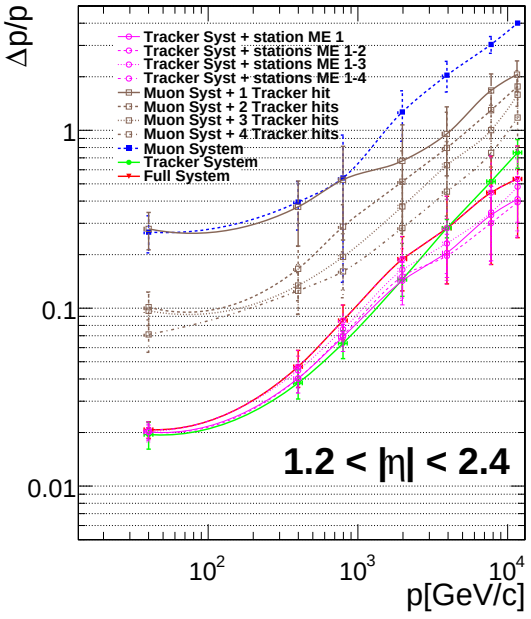

(c) End-caps q/p resulution vs p

Figure 15: Resolution on q/p divided by pseudorapidity regions for the different muon reconstruction steps.

5.2.3 Momentum Resolution vs η

The resolution plots as a function of η are shown in figure Fig. 43(h), Fig. 46(h), and Fig. 47(h). An inherent feature for all plots is the sudden decrease in resolution above $|\eta| \geq 1.5$. The two main contributions for this effect are the increase in material in the end-caps and the steady decrease of the magnetic field. In addition, at

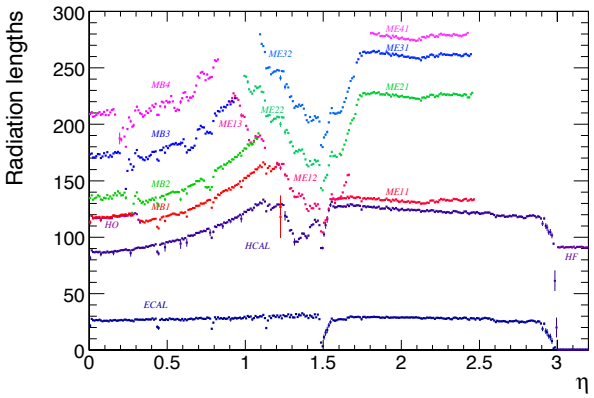

Figure 16: Material in terms of radiation lengths vs η

$|\eta| = 1.5$ there is a minimum in the material as shown in figure Fig. 16, which directly translates into a minimum for resolution curves.

The *stand-alone* fit directly reflects the distribution of the material at low momentum (neglecting non-linear magnetic field effects), we can infer this another way, given that the fact that the resolution curves cross for momenta below a few hundred GeVs, shows that the resolution component linear in momentum is small compared to the resolution component due to multiple scattering.

5.3 Effects of Misalignment on Momentum Resolution

To properly reconstruct muons, the positions and orientations of all elements in the silicon tracker and the muon system need to be well-known relative to one another. Misalignment, by which we mean an incorrect assumption about the geometry of the detectors, causes errors in the direction and curvature of reconstructed tracks, both of which have a degrading effect on reconstructed masses. To minimize these errors, data from dedicated hardware alignment systems and from the tracks themselves are used to identify the true positions of the detector elements in a common coordinate system, but there will always be some residual error. In this section, we calculate the error in muon p_{T} and dimuon masses which would be incurred under a variety of realistic alignment scenarios. The scenarios have been derived from experiences with the hardware alignment systems at the TIF (Tracker Integration Facility, for the silicon tracker), global runs in the spring of 2008 (for the muon alignment system), and the CSA08 computing exercise (for track-based alignment of both systems).

The silicon tracker and the muon system each have advantages at different momentum scales, and hence the importance of alignment of each system depends on the momentum scale. The tracker elements have a much higher intrinsic resolution, on the order of tens of microns within each module, as opposed to $100 - 200$ μm for $r\phi$ measurements in the muon system. The muon system, however, has a larger lever arm, measuring curvatures 4–7 m from the beamline as opposed to 1 m in the tracker (curvature resolution scales as the radial lever arm squared). Using all information from both systems, the tracker dominates momentum measurements below several hundred GeV/c (in part due to the lack of multiple scattering), but both systems are essential to resolve nearly straight TeV-scale muons. Consequently, the resolution of low-momentum tracks depends strictly on the quality of tracker alignment, while muon alignment and inter-alignment between the two systems is necessary to resolve highly energetic muons.

Alignment scenarios for muon resolution studies were generated in two different ways: randomly from resolution estimates or as the result of a mock-data challenge. For studies of alignment from the hardware systems, resolution estimates were derived from measurement uncertainties in the alignment devices, closure of overconstrained systems, and agreement with an independent photogrammetry survey. These uncertainties are hierarchical: detector elements were measured with the highest precision relative to their supporting structures, while the structures themselves were determined relative to other systems with less precision. We then create a model of the detector using the full hierarchy of uncertainties to generate random Gaussian deviations from ideal geometry: the misalignment scenario represents a typical difference between true geometry and measured geometry. We calculate the effect this would have on muon momenta and dimuon masses by generating Monte Carlo with an ideal detector and reconstructing it with the different scenarios. Since the misalignments are small compared with the size of the detector, this is equivalent to generating with the true geometry and reconstructing with the measured geometry, as would be the case with data.

To generate track-based alignment scenarios, we begin with a hardware-only geometry and attempt to align it, just as we would with real data. The Monte Carlo tracks fed into the alignment procedure were also generated with an ideal detector, so the resulting detector description represents the difference between true geometry and aligned geometry, and is useful for the same kinds of muon resolution studies. Scenarios prepared this way automatically include any correlations between detector elements that might survive or be generated by the track-based alignment process, such as global distortions of the detector which leave the track-based χ^2 invariant.

The track-based alignment scenarios used for these studies are products of the S156 iCSA08 exercise, a combined $10\ \mathrm{pb}^{-1}$ test of almost all alignment and calibration workflows. Both the tracker and the muon system were assumed to be miscalibrated as well as misaligned, so corrections had to be applied cumulatively to produce a realistic final state (calibration and beamspot determination before alignment, and tracker alignment before muon alignment). See the CSA08 Note [8] for details on the alignment procedure.

Fig. 17 presents the curvature ($1/p_\mathrm{T}$) resolution of muon tracks over three orders of magnitude in p_T. Each series of points represents a different alignment scenario: a perfectly-aligned detector (what one would get from the constants database using an "IDEAL_Vn" tag), the result of the $10\ \mathrm{pb}^{-1}$ CSA08 exercise (a "CSA08_S156" tag), a randomly-generated estimate of alignment quality after $10\ \mathrm{pb}^{-1}$ ("10PB_Vn"), used in the generation of some Monte Carlo samples, and a randomly-generated estimate of alignment quality with the expected precision of the LHC at statup based on survey information and hardware data ("STARTUP_Vn"). Muons were selected from physics samples: J/ψ (below 5 GeV/c) using the calorimeter only (caloMuons), Z (5–50 GeV/c) using full global muons (globalMuons), and Sequential Standard Model Z' (above 50 GeV/c) using the first hit on every station (TeVmuon/firstHit) to avoid losses in resolution due to showering.

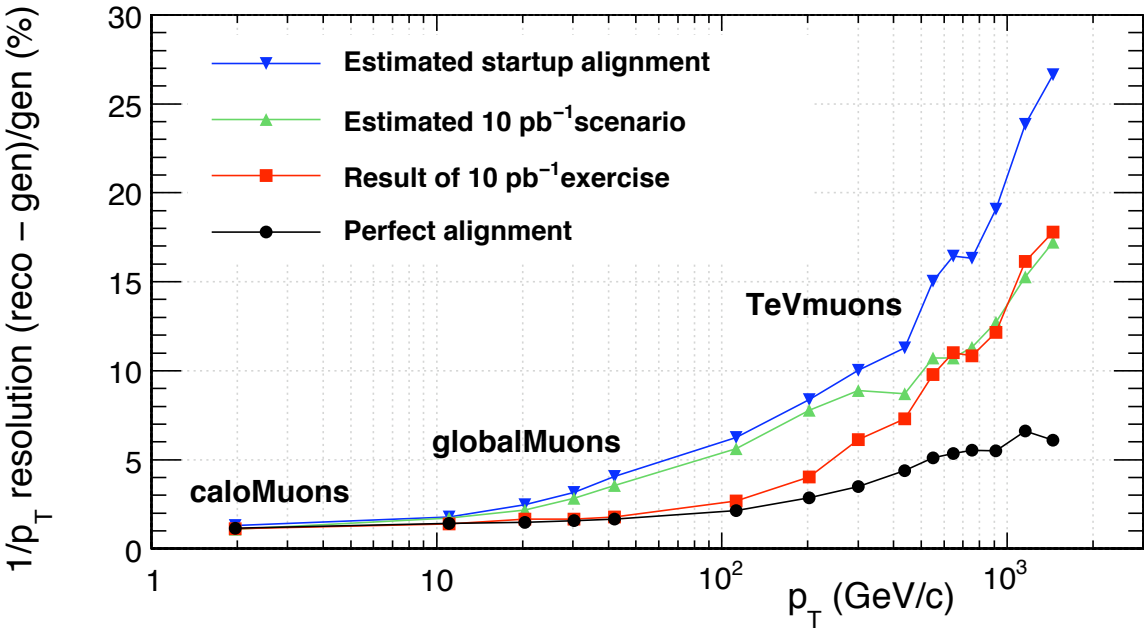

Figure 17: Track curvature resolution as a function of p_T for four alignment scenarios. Three algorithms were used to identify muon tracks and hits: caloMuons (below 5 GeV/c), globalMuons (5–50 GeV/c), and TeVmuons/firstHit (above 50 GeV/c).

To interpret this plot, note first that the fractional uncertainty in curvature ($1/p_\mathrm{T}$) for a given track is equal to the fractional uncertainty in transverse momentum (p_T) for that track, so we can read the

$$(\text{reconstructed} - \text{generated})/\text{generated}$$

curvature resolution as transverse momentum resolution. A much better alignment accuracy was achieved in the CSA08 exercise than expected, primarily from minimum-bias events, while the first stations of the muon system were aligned to roughly the expected accuracy. This is why there is a gap between simulated (red squares) and estimated (green upward-pointing triangles) at low p_T, where the tracker dominates, but the gap closes above 400 GeV/c. The $10\ \mathrm{pb}^{-1}$ track-based muon alignment is more accurate than an alignment with the hardware system only (0.7 mm rather than 1.2 mm) or the startup estimates, but still far from design (0.2 mm). Including cosmic rays in the alignment could improve this [8]. The better than expected alignment accuracy achieved in the

CSA08 exercise or the simulated $10\ \mathrm{pb}^{-1}$ scenario may be optimistic, but this performance does not invalidate the results of these alignment studies.

Curvature resolution is a strong function of η, due to the available lever arm. Fig. 18 illustrates this dependence for the three most relevant scenarios: a perfect detector, the track-based results, and the startup estimate. The transition region between the barrel and endcap of both the silicon tracker and the muon system is roughly $0.9 < |\eta| < 1.3$.

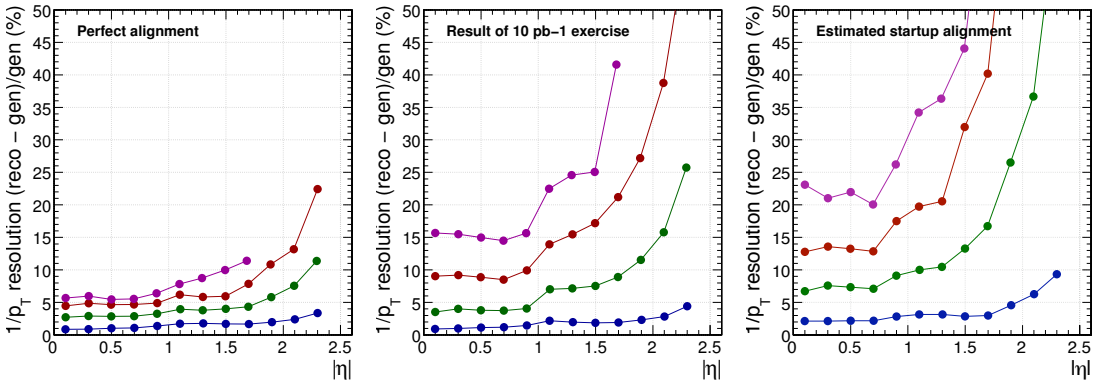

Figure 18: Curvature resolution versus η for three scenarios. Connected series of points, from bottom to top, are 5–50 GeV/c (blue), 50–500 GeV/c (green), 500–1000 GeV/c (red), and 1000 to about 1500 GeV/c (purple).

Finally, to see what this means for dimuon resolution, Fig. 19 displays the fractional dimuon mass resolution as a function of mass for five resonances: J/ψ, Z, and a 1, 2, and 3 TeV Sequential Standard Model Z'. The same four alignment scenarios are presented, and the same track-selection conditions apply (caloMuons for J/ψ, globalMuons for Z, and TeVmuon/firstHit for Z').

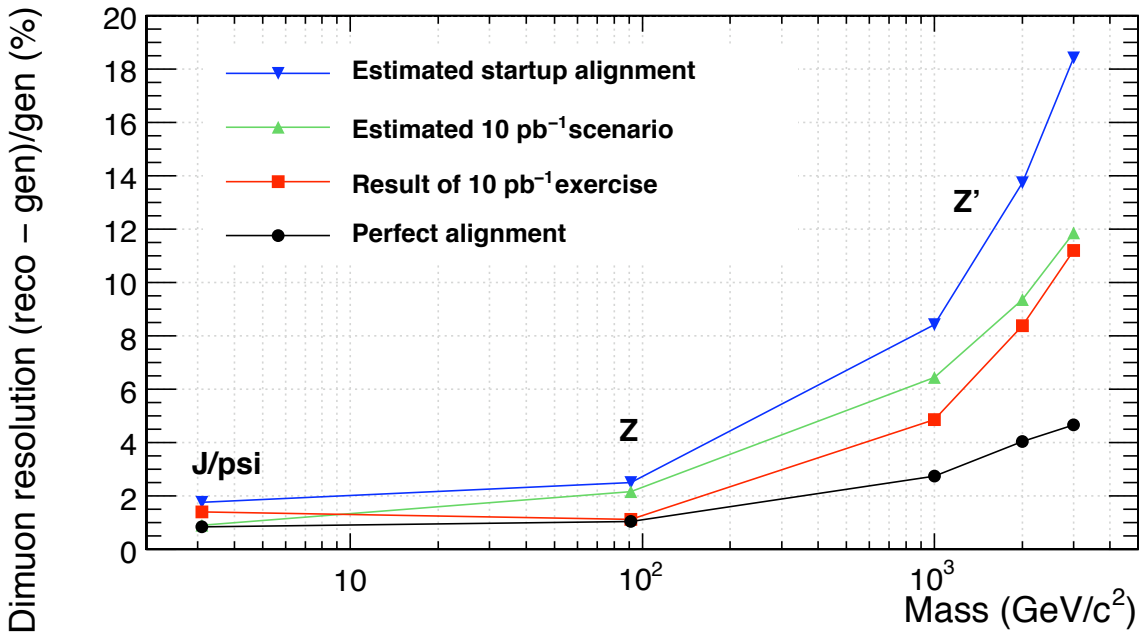

Figure 19: Dimuon mass resolution for four alignment scenarios.

5.4 High energy muon reconstruction

Muons with energies of several hundred GeV and more have a high probability of producing electromagnetic showers in the iron of the CMS magnet return yoke. These large energy losses can significantly degrade the performance of the muon track fitter. Two main effects can contribute to this degradation:

- The muon can lose a large fraction of it's energy, in which case the part of the track following the energy loss should be discarded as the particle's momentum has changed.

- The shower can contaminate the muon detectors, causing the local reconstruction algorithms to return incorrect trajectory measurements. Including these measurements in the track fit can lead to incorrect reconstructed momentum values.

The approach chosen to minimize the negative effect of showers on muon momentum estimation is the following: several refits of the global muon trajectory are performed, with different sets of hits:

- First Muon Station - a fit with the hits from the tracker and the first muon station with hits, minimizing the effect of a large change in muon momentum after showering.
- Picky Muon Reconstructor - a fit with the hits selected by an algorithm applying tight cuts for hit compatibility with the trajectory, but only in muon stations with high multiplicity of reconstructed hits. This approach minimizes the influence of contaminated chambers, while preserving the hits from chambers providing good trajectory measurement, despite containing a shower.

These two refits optimized for showering muons are considered along with the standard global muon fit and the fit using only the hits from the inner tracker, and the global goodness-of-fit of each four trajectories is evaluated. Two algorithms have been developed for selecting the best trajectory, basing the decision of the comparison of the goodness-of-fit variables. Known as the ”cocktails”, these were found to perform better than any of the four individual algorithms.

The performance comparison between all the approaches is shown in Fig. 20.

6 Tracker Muon Reconstruction in the CMS Detector

The muon track reconstruction algorithm described in Section 4 and Section 5 starts from the muon system and combines stand-alone muon tracks with tracks reconstructed in the inner tracker. This approach works well if a high quality muon track exists in the muon detector. However, in some cases the hit and segment information in the muon system is minimal, and stand-alone muon reconstruction fails. For example a large fraction of muons with transverse momentum below 6-7 GeV/c (cf. Fig. 4c) do not leave enough hits in the muon spectrometer to be reconstructed as stand-alone muons. Moreover, geometrical effects, such as the gap between the wheels, (Fig. 1) also cause retrievable losses.

A complementary approach consists in considering all silicon tracker tracks and identifying them as muons by looking for compatible signatures in the calorimeters and in the muon system [9]. Muons identified with this method are called “Tracker Muons” and are described in the following sections.

It is important to keep in mind that the association between muon chamber segments and silicon tracker tracks is kept very loose by design in the construction of a Tracker Muon. Thus, these objects should in general not be used without further requirements. Tracker Muon requirements developed by the muon POG are described in a separate note [10].

6.1 Tracker Muon algorithm

The algorithm starts from reconstructed silicon tracker tracks above a given p or p_{T}. The momentum requirements, as well as many other parameters in the algorithm, are configurable. See Section 6.4 for information on the configurable parameters.

The general idea of Tracker Muons is to reconstruct and identify muons in CMS starting from a silicon tracker track and then searching for compatible segments in the muon detectors. The energy deposition in the calorimeter can also be used for muon identification.

The algorithm collects and stores all the relevant information into a final Muon object. Specific muon identification criteria can be developed based on these variables [10].

No combined (silicon-hits + muon-hits) track fit is performed. Thus, the momentum vector of a Tracker Muon is the same as that of the silicon tracker track. Note, however, that if a Global Muon is reconstructed using the same silicon tracker track, the Global Muon fit is stored in the same Muon object and the default momentum of the muon in the object is taken from the Global Muon fit. The momentum of the silicon tracker track fit is still retrievable through the reference to the silicon tracker track which is stored in the muon object.

6.1.1 Propagation into the calorimeter

Each silicon tracker track is propagated outward from the inner tracker into the calorimeter using the `TrackAssociator` algorithm. The propagation is performed with the same `Stepping Helix` algorithm that is used in stand-alone and global muon reconstruction (see Section 3.4.3).

Tracks are propagated to the face of the calorimeter and then stepped into the calorimeter (four steps for ECAL and barrel HCAL; 20 steps for endcap HCAL). The energies in all the crystals (ECAL) or towers (HCAL) crossed by the track, as well as the energies in a 3x3 regions, are calculated and stored in the muon object.

As a default, these energies are computed based on RecHits. This allows for the best possible resolution for the small energy deposition in the ECAL. Alternatively, one could use CaloTowers instead of RecHits. In that case the energy stored in the muon object would be consistent with what is used in the calculation of calorimeter $\not\!\!E_T$, thus allowing for a more precise muon-$\not\!\!E_T$ correction.

It is important to note that the propagation into the calorimeter, the calculation of the calorimeter energy, and the storing of this information in the muon object is not a unique feature of Tracker Muons. The calorimeter energy is calculated and stored in the muon object for all reconstructed muons in CMS (Global Muons, Stand-Alone Muons, Tracker Muons).

6.1.2 Propagation into the muon detector

Next, the track is propagated into the muon detector. As before, the propagation is based on `TrackAssociator`, which in turn is based on `SteppingHelixPropagator`. Thus, the propagation into the muon detector takes into account the magnetic field, the average expected dE/dX, and it takes multiple scattering into account in the estimated uncertainties on the propagated trajectory. During the track propagation, the covariance matrix of the track is properly updated.

As the track is propagated through the muon detector, the algorithm keeps track of which chambers are crossed or nearly crossed by the extrapolated track. Note that because of multiple scattering a track that points outside a chamber could actually cross a chamber. This is why the algorithm keeps track of the nearly crossed chambers as well as the crossed chambers.

For each crossed or nearly crossed chamber the algorithm stores

- The distance between the propagated track and the nearest chamber edge, in both the chamber local X and Y directions. This distance has a sign convention (negative inside the active volume, positive outside the active volume). This is illustrated in Fig. 21.
- The one sigma uncertainty in the quantity above calculated from the uncertainties in the transported track covariance matrix, including multiple scattering and dE/dX.
- The position of the extrapolated track in local (X,Y) coordinates inside a chamber.
- The slope of the extrapolated track (dX/dZ and dY/dZ) where X and Y are local chamber coordinates, and Z is the coordinate perpendicular to the chamber.
- The one sigma uncertainties in positions and slopes.
- The detID of the chamber.
- A vector with information for 4D segments in the chamber that are near enough to the propagated track. We refer to these segments as associated segments.

The vector of segment information contains the following information

- The local positions (X and Y) of the segment
- The local slopes (dX/dZ and dY/dZ) of the segments
- The uncertainties on these quantities
- Information on *arbitration*; the concept of arbitration is described in Section 6.2.

All of the above information can be employed for the purpose of muon identification. For example, the difference in position between the expected position of a muon segment in a chamber (from the track extrapolation) and the nearest reconstructed muon segment can be used to confirm the quality of a track-to-segment match. In Fig. 22 this difference in local Y position is shown for segments in the first station and the third station of the Drift Tube detector, for a Monte Carlo sample of $p_{\mathrm{T}} = 10$ GeV/c muons. Due to the longer extrapolation to the third station, the extrapolation uncertainty increases as expected. The pull distributions however show that the uncertainties are estimated correctly and can be used to determine the quality of the segment match. Similar plots are shown in Fig. 23 for the segment direction in the Cathode Strip Chambers. While in the majority of cases a good match can be established, there is a non-negligible chance that the direction of a segment is misreconstructed, leading to small but visible tails in the pull distributions. Nevertheless the direction information can be useful and is available for muon identification. More examples are shown in Fig. 24 to Fig. 28.

6.1.3 Creation of the persistent muon object

The Tracker Muon algorithm is run for each track above a certain p or p_{T}. However, the muon object for a given track is stored only if the track has a minimum number of associated segments. This requirement is configurable and its default is at least one associated segment for the 2_X release series.

6.2 Arbitration

The algorithm described so far treats each track individually. If two (or more) tracks are near each other, it is quite possible that the same segment or set of segments is associated to more than one track. This can happen for muons in jets.

By arbitration we mean the pattern recognition problem of assigning segments to tracks. In the current implementation of the algorithm, arbitration is performed with two separate algorithms and the results are stored in the muon object (more precisely: in the vector of segment information inside the muon object). In other words, the user can in principle

- use one of the existing algorithms
- ignore the arbitration problem
- implement a different arbitration algorithm

The two algorithms currently implemented are very simple and based on an study of muons from b-quarks in top events. The segment arbitration is based on the best ΔX match or the best $\Delta R^2 = \Delta X^2 + \Delta Y^2$ match, where ΔX (ΔY) is the distance in local X (Y) between the segment and the extrapolated track. The two current algorithms are referred to as DxArbitration and DrArbitration.

More explicitly, the arbitration algorithm works as follows: suppose a segment is associated to more than one track. For each track we calculate ΔX (ΔR) between the track and the segment. The track-segment combination with the best absolute value of ΔX (ΔR) is the combination that passes the arbitration algorithm. This result is stored in the muon object.

The current arbitration algorithms are very simple, since they only use information from one chamber at a time. Mistakes in arbitration can impact the efficiency, because segments that belong to a real muons can be reassigned to a different candidate. This effect depends on the track density near a muon, and, of course, on the requirements that are imposed.

As an example, in Table 3, we show the efficiency loss due to arbitration for muons from bottom and charm decays in top events using the LastStation requirements. The LastStation requirements will be discussed in a forthcoming note. Briefly, they require that there be at least two associated segments that are matched within 3σ in X (*Loose*) or X and Y (*Tight*) with the extrapolated track. Furthermore, the algorithm defines a *last station* as the outermost muon station crossed by the extrapolated track well inside the active area of the chamber. The LastStation requirements demand that there be a segment in this last station, to ensure that the muon penetrated to the back of the detector. From Table 3 we see that even if the arbitration algorithms are very simple, the efficiency losses are quite small.

Muon source	Eff. Loss 1	Eff. Loss 2	Eff. Loss 3	Eff. Loss 4
$b \to \mu$	3.3 ± 0.4 %	1.7 ± 0.3 %	3.5 ± 0.5 %	1.1 ± 0.3 %
$c \to \mu$	5.4 ± 0.5 %	2.6 ± 0.3 %	5.6 ± 0.5 %	2.9 ± 0.3 %

Table 3: Efficiency loss due to arbitration for muons in top events for four different algorithms. Algorithm 1: TMLastStationLoose and ΔX arbitration; Algorithm 2: TMLastStationLoose and ΔR arbitration; Algorithm 3: TMLastStationTight and ΔX arbitration; Algorithm 4: TMLastStationTight and ΔR arbitration.

6.3 Performance

The pulls of ΔX and ΔY between the extrapolated muon track and the matched segments are quite close to 1, see for example Fig. 22 for the ΔY. The distance between the propagated track and the nearest chamber edge (`dist`) also behaves sensibly and can be used to decide whether or not a given chamber should have an associated segment. This is illustrated in Fig. 21, where we show for single muon events the probability of finding a segment in a given chamber as a function of `dist`.

6.4 Configuration

The Tracker Muon producer has many parameters that are configurable. Here we list the most important ones, with their defaults for the 2_X release series:

- the minimum p (3 GeV/c) or p_{T} (1.5 GeV/c) for a Tracker Muon;
- the minimum number of matched segments (one);
- the matching quality between the extrapolated track and a matching segment (4 σ or 3 cm in the X view);
- for an extrapolated track that just misses the active volume of a chamber, the maximum distance from the chamber edge for the chamber information to be kept in the Tracker Muon object (5 cm in both X and Y).

6.5 Intended use cases

The Tracker Muon algorithm can be particularly useful in cases where one has a soft p_{T} spectrum for the lowest-energy muon in the event since these muons are more likely to range out in the detector and not be fully reconstructed. Even for event topologies in which all of the final state muons are fully reconstructed, the information provided by the identification algorithm helps in understanding muon fake rates and solving potential ambiguities at the analysis level. In addition, the algorithm will be useful during commissioning for picking out a class of potential, unreconstructed muon candidates for studying and improving the reconstruction software. The combination of outside-in and inside-out approaches in a merged collection of muons has already shown great potential in improving robustness and enhancing performance in terms of efficiency versus purity. This will be reported in more detail elsewhere [10].

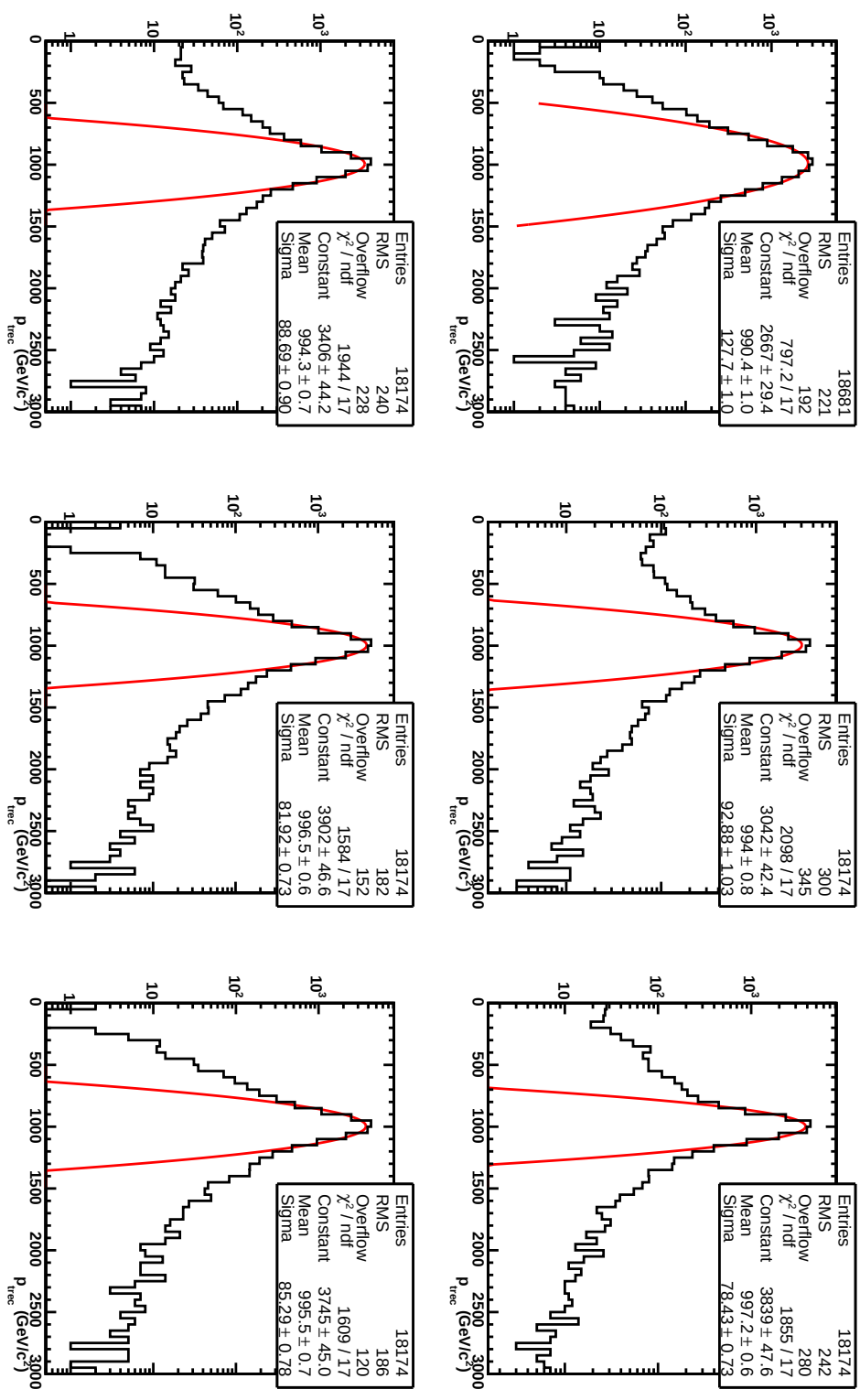

Figure 20: Reconstructed p_{T} distributions for $p_{\mathrm{T}} = 1$ TeV single muons for the different refits. Starting from the top left plot, the distributions show a fit with the Tracker only, followed by the default Global fit, First Muon Station, Picky Muon Reconstructor, and two cocktails, the old one and the new one.

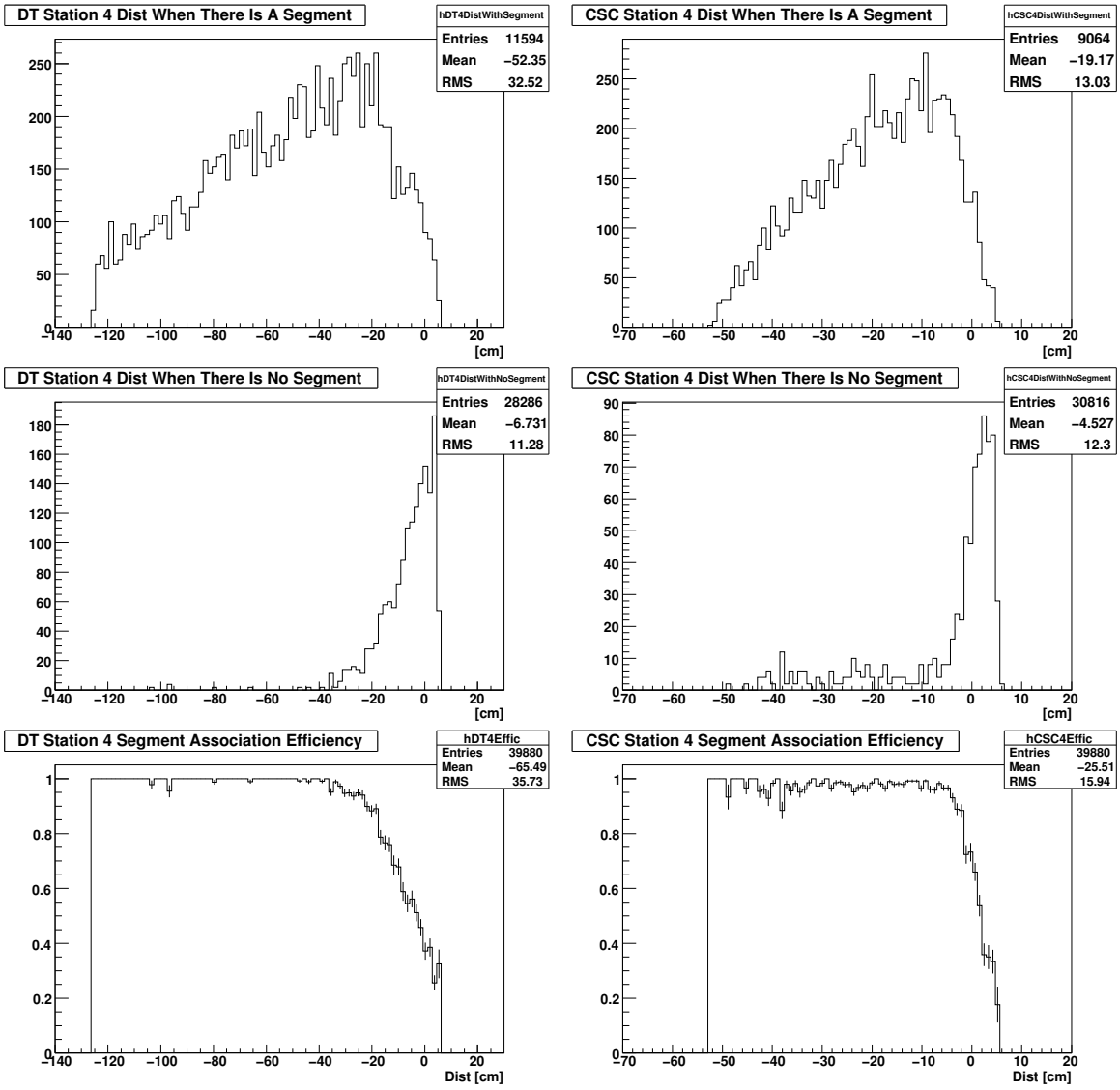

Figure 21: The probability of reconstructing a segment in DT (left) and CSC chambers (right) as a function of the distance from the nearest edge for a Monte Carlo sample of $p_{\mathrm{T}} = 10$ GeV/c muons. This efficiency is calculated from the number of times that a segment is found (top plots) and that no segement is found (middle plots). The sign convention is that negative (positive) distances correspond to tracks extrapolating inside (outside) the fiducial volume of the chambers.

.

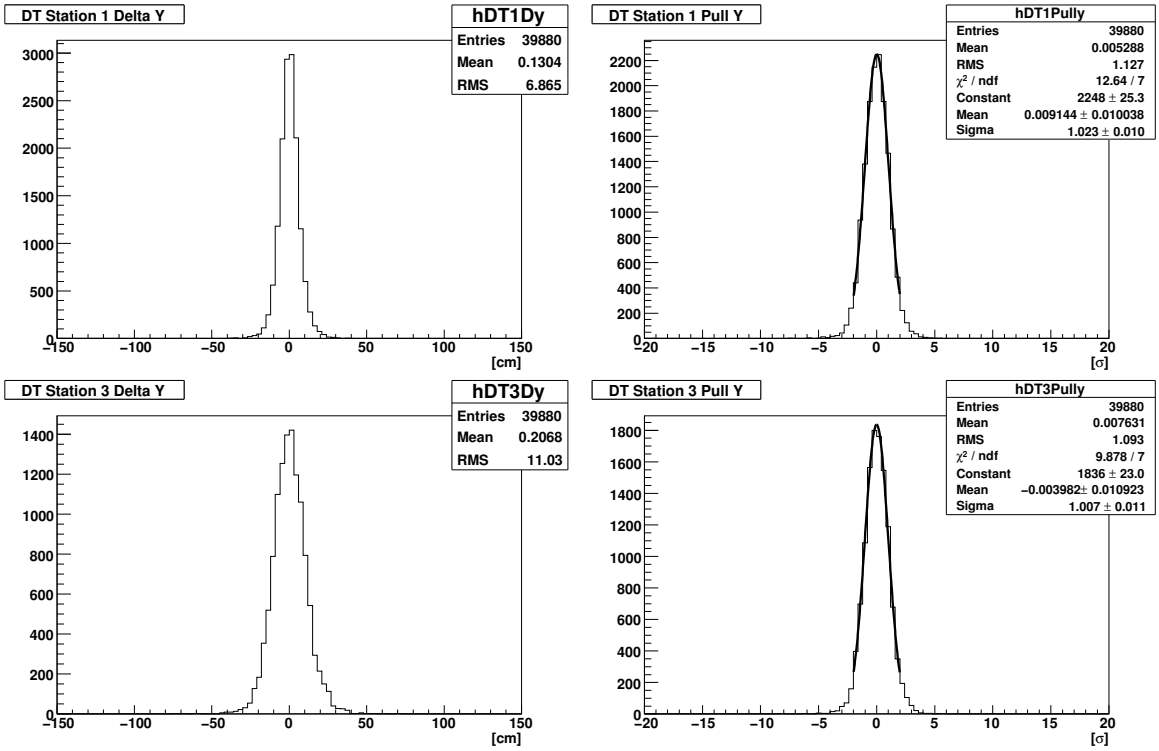

Figure 22: The distance between the extrapolated track position and the reconstructed segment in the local-Y direction in the first (top plots) and third layer (bottom plots) of the drift tubes for a Monte Carlo sample of $p_{\mathrm{T}} = 10\mathrm{GeV}/c$ muons. The left plots show the distance, while the right plots show the pull (distance divided by the estimated uncertainty). The distribution of the distance between segment and extrapolation becomes broader when going from station 1 to 3, but the width of the pull remains stable and has a value close to unity.

.

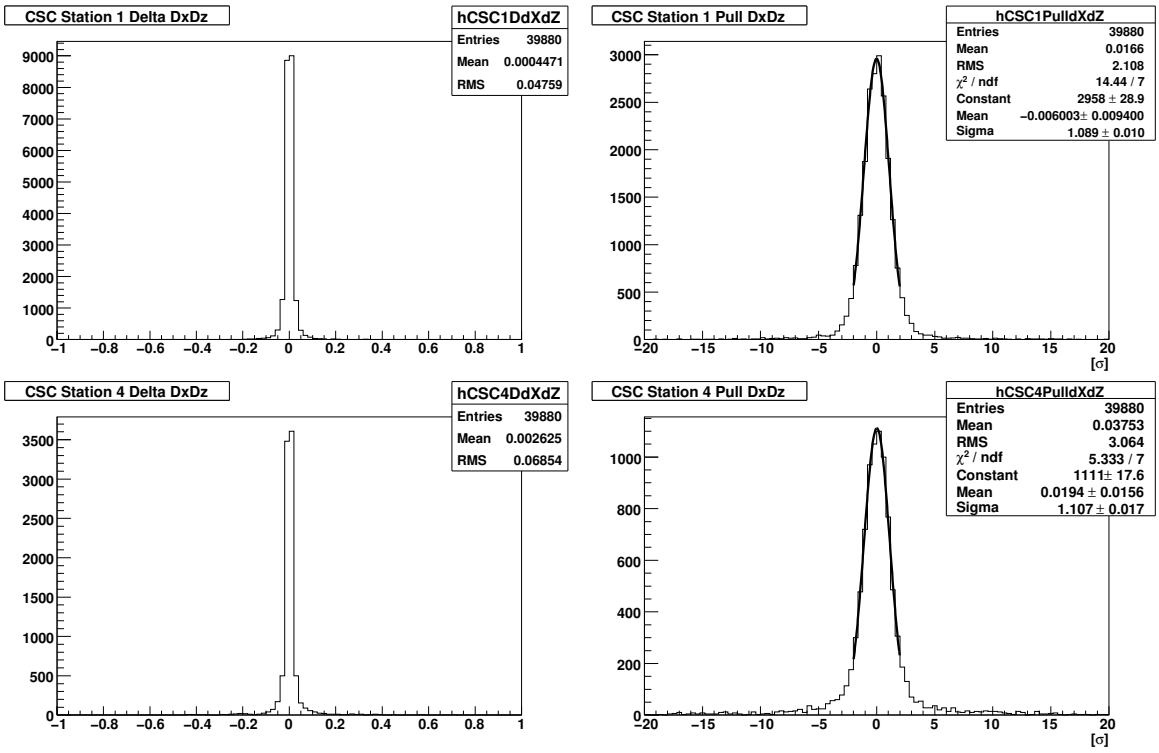

Figure 23: The difference between the direction of the extrapolated track and the reconstructed segment in the local-XZ plane in the first and fourth station of the Cathode Strip Chamber for a Monte Carlo sample of $p_{\mathrm{T}} = 10\mathrm{GeV}/c$ muons. The differences are plotted on the left, and the corresponding pull distributions on the right.

.

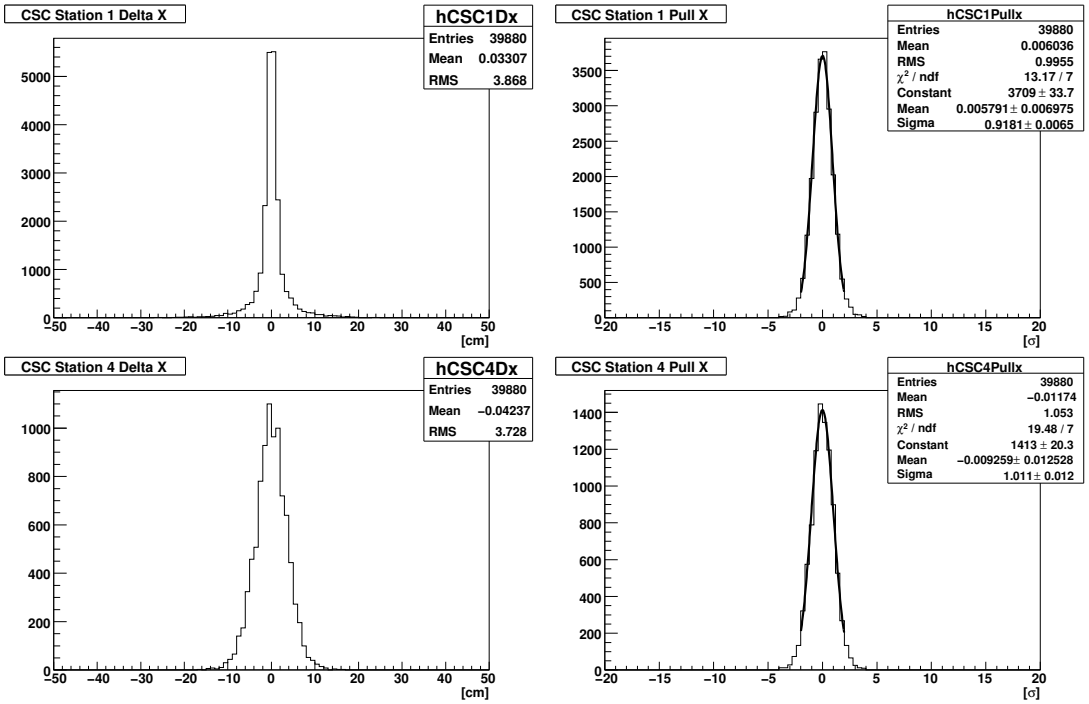

Figure 24: The distance between the extrapolated track position and the reconstructed segment in the local-x direction in the first and fourth station of the Cathode Strip Chambers for a Monte Carlo sample of $p_{\mathrm{T}} = 10\mathrm{GeV}/c$ muons.

.

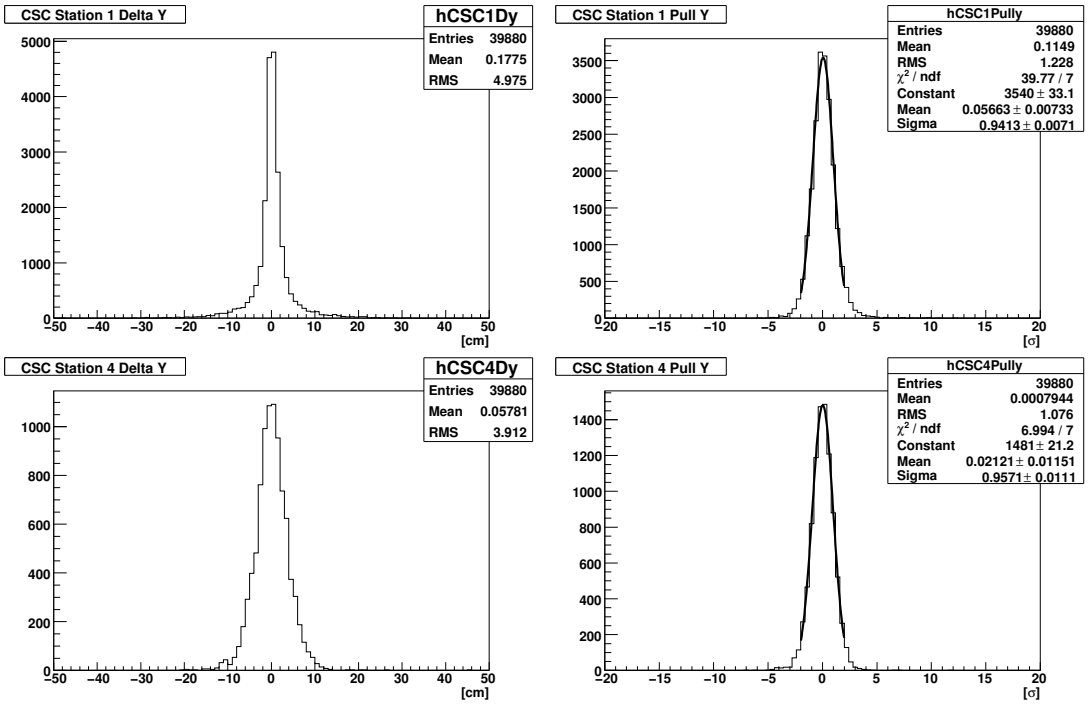

Figure 25: The distance between the extrapolated track position and the reconstructed segment in the local-Y direction in the first and fourth layer of Cathode Strip Chambers for a Monte Carlo sample of $p_{\mathrm{T}} = 10\mathrm{GeV}/c$ muons.

.

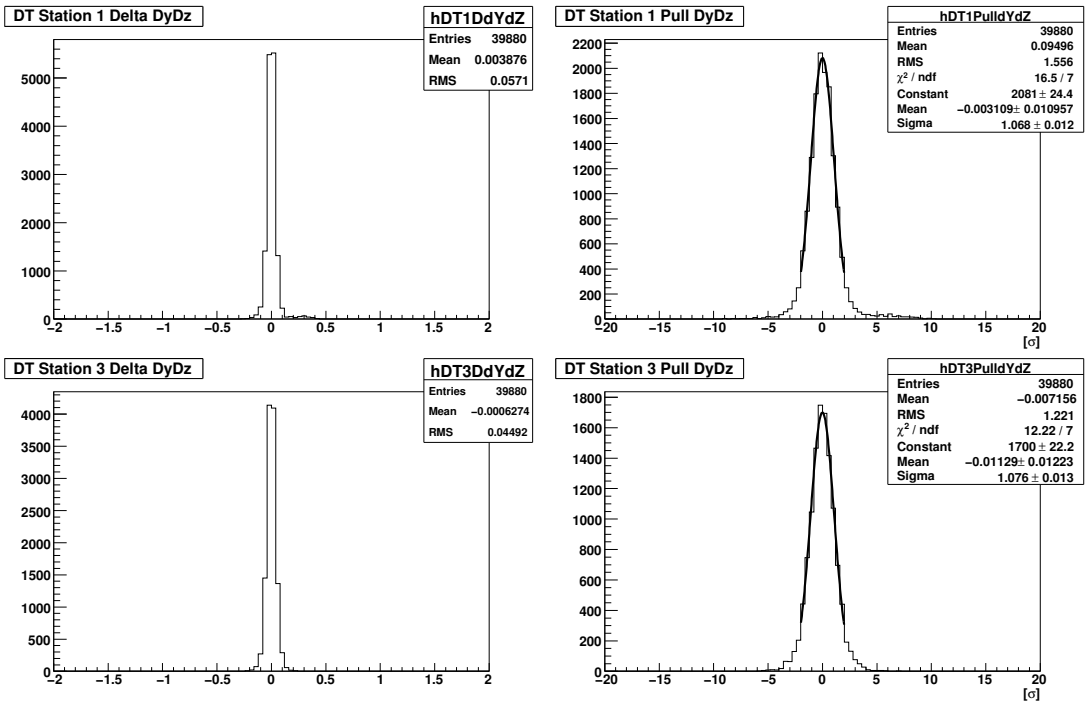

Figure 26: The difference between the direction of the extrapolated track and the reconstructed segment in the local-YZ plane in the first and third layer of Drift Tubes for a Monte Carlo sample of $p_{\mathrm{T}} = 10\mathrm{GeV}/c$ muons.

.

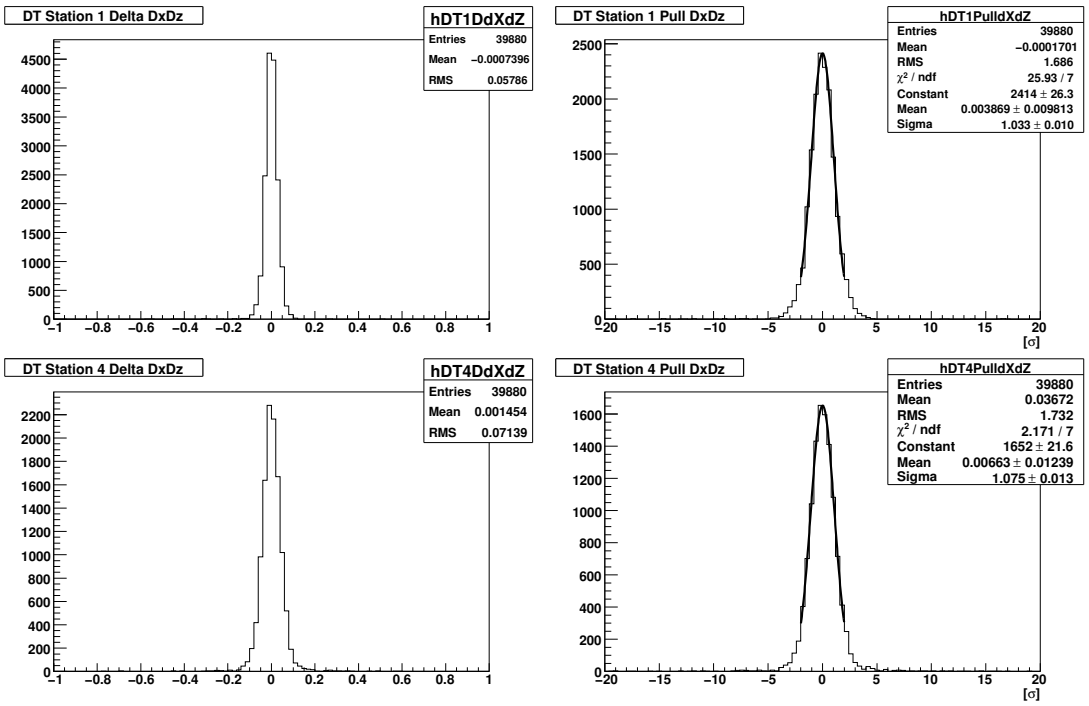

Figure 27: The difference between the direction of the extrapolated track and the reconstructed segment in the local-XZ plane in the first and fourth layer of Cathode Strip Chambers for a Monte Carlo sample of $p_{\mathrm{T}} = 10\mathrm{GeV}/c$ muons.

.

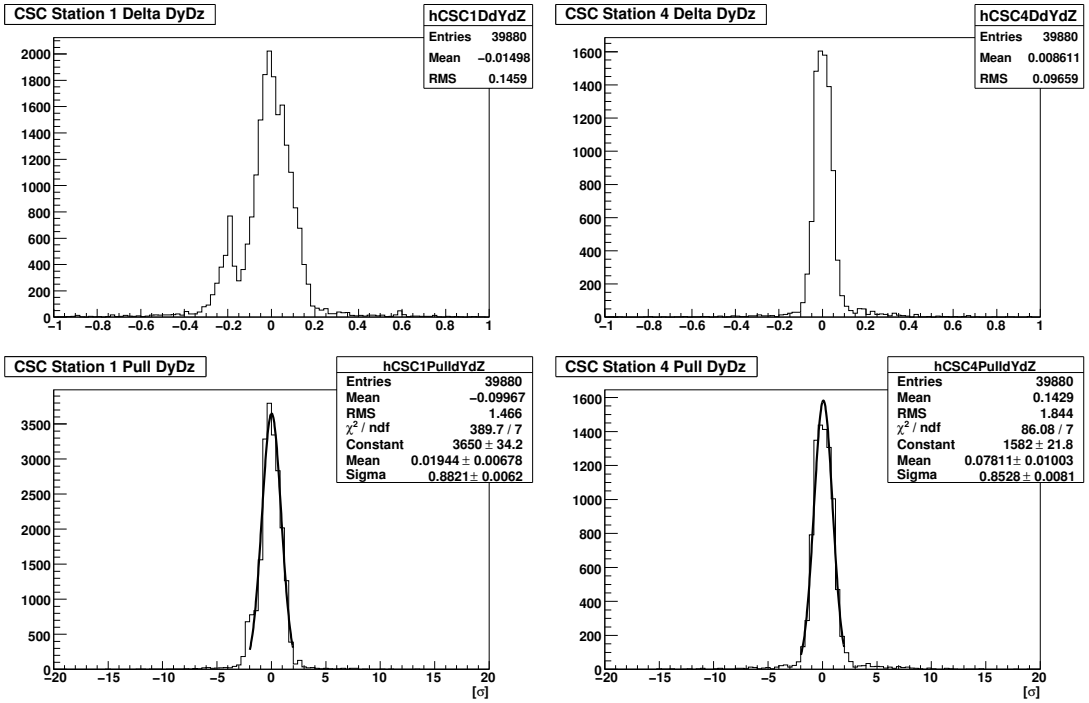

Figure 28: The difference between the direction of the extrapolated track and the reconstructed segment in the local-YZ plane in the first and third layer of Cathode Strip Chambers for a Monte Carlo sample of $p_{\mathrm{T}} = 10\mathrm{GeV}/c$ muons.

.

7 Performance

The muon reconstruction algorithms have been described in Section 4 to Section 6 and the performance of these algorithms has been evaluated using the full detector simulation with a magnetic field of 3.8 Tesla. In addition the performance of reconstruction in the inner tracker alone is determined since such tracks are fundamental for global muon reconstruction.

The performance has been evaluated using samples of single muons generated with different values of p_{T} and flat distributions in η and ϕ (Table 4) using CMSSW 220. The performance has also been evaluated for more than one muon and with non-flat distributions of their parameters. The samples used are shown in Table 4.

Table 4: Samples used for the study of the muon reconstruction performance ($|\eta| \leq 2.4$ and $|\phi| \leq \pi$).

Transverse Momentum (GeV/c)	Number of events
5	50000
10	50000
50	50000
100	50000
200	50000
500	50000
1000	50000
2000	35000
3000	20000
0-500 (flat)	250000

Using these samples we have measured the efficiencies, the resolutions and the pulls of the track parameters. In this analysis in order to match the simulated muon with the reconstructed track, a cone criterion has been used, $\Delta R = \sqrt{(\Delta\phi)^2 + (\Delta\eta)^2}$ as well as an association algorithm which matches simulated hits and reconstructed hits. The single particle generated events include also the anti-particle in order to study reconstruction of particles with different charges. No charge dependant differences were observed. In the following analysis, therefore, no distinction is made between the two charges and all quantities are determined using the full samples.

The final results of the efficiency of the stand-alone reconstruction are shown in this section. The resolutions and pulls of the stand-alone track parameters are shown in Section 7.

7.1 Efficiencies

For the stand-alone and global reconstruction the efficiencies for each step are factorized as follows:

$$\begin{aligned} \varepsilon_{seed} &= \varepsilon_{seed-algo} \times \varepsilon_{\mu-acceptance}, \\ \varepsilon_{sa} &= \varepsilon_{seed} \times \varepsilon_{sa-algo}, \\ \varepsilon_{glb} &= \varepsilon_{sa} \times \varepsilon_{tk} \times \varepsilon_{matching}, \end{aligned} \tag{4}$$

ε_{seed} is the efficiency for finding a seed which is matched to the simulated hits and where $\varepsilon_{\mu-acceptance}$ accounts for the muon system geometry acceptance and for such effects as inefficiencies due to the energy loss in the material before the muon chamber stations and losses due to the bending in the magnetic field. After applying the reconstruction algorithms efficiencies are evaluated. These include the total efficiency of reconstruction normalised to the number of simulated tracks, algorithmic efficiencies, which are the efficiencies with respect to one (or more) previous reconstruction steps and for reconstruction in the muon spectrometer alone the effect of the system acceptance on the total reconstruction efficiency.

7.1.1 Stand-Alone reconstruction

In Fig. 29 and Fig. 30 the total efficiency for the muon seeding step (ε_{seed}) and for the stand-alone reconstruction (ε_{sa}) is shown. The loss in efficiency at $|\eta| \sim 0.3$ is due to a geometrical effect, since in that region there is a discontinuity between the central wheel and its neighbours (Fig. 2). The dips in the $0.8 < |\eta| < 1.2$ region are due to failures in the seed-finding algorithm which may be recovered although that region is known to be problematic as in that region DT and CSC segments are used together to estimate the seed state. In Fig. 30 and Fig. 31 the

algorithmic efficiency of the pattern recognition in the muon system ($\varepsilon_{sa-algo} = \varepsilon_{sa,seed} = \varepsilon_{sa}/\varepsilon_{seed}$) is shown. These figures and Table 5 show that the stand-alone muon reconstruction efficiency is determined by the seed, as $\varepsilon_{sa,seed}$ is close to 100%. The small inefficiency is due to incorrectly estimated parameters at the seeding stage, which may lead to a failure in the pattern recognition.

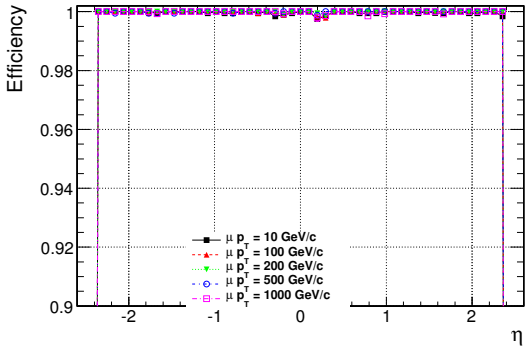

(a) ε_{seed} vs η

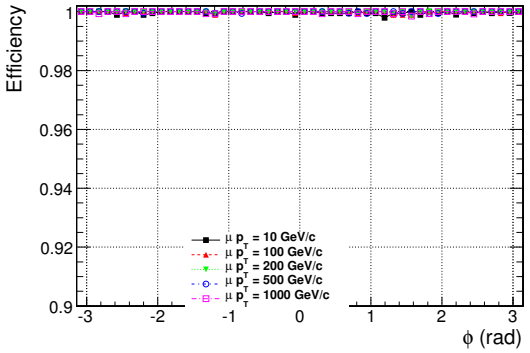

(b) ε_{seed} vs ϕ

Figure 29: Efficiency of the muon seed reconstruction in the muon spectrometer as a function of η and ϕ, for different p_{T} samples.

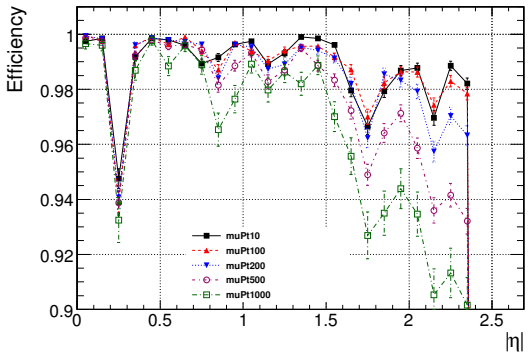

(a) ε_{sta} vs η

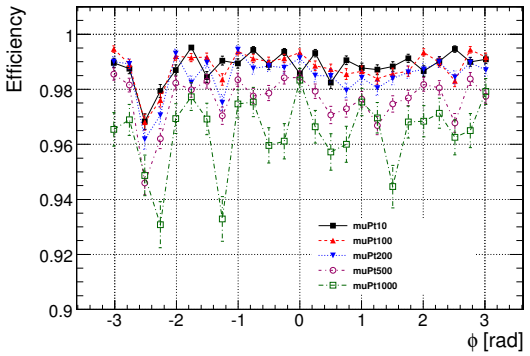

(b) ε_{sta} vs ϕ

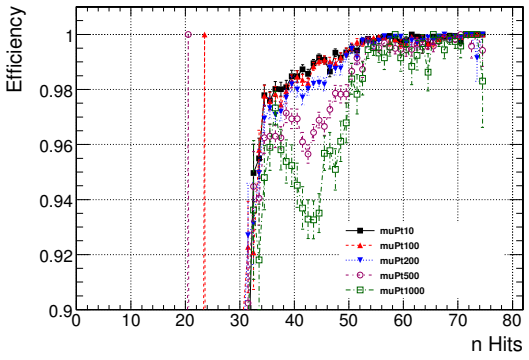

(c) ε_{sta} vs n Hits

Figure 30: Efficiency of the reconstruction in the muon spectrometer as a function of η, ϕ, p_{T}, and number of hits for different p_{T} samples.

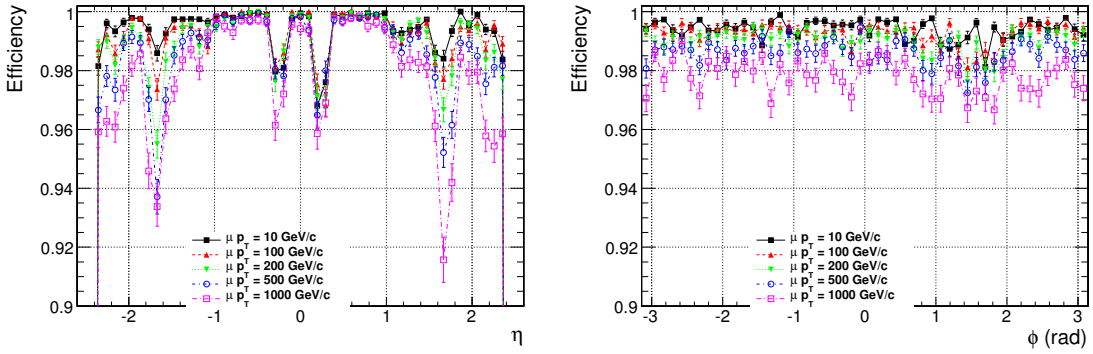

(a) $\varepsilon_{sta,seed}$ vs η

(b) $\varepsilon_{sta,seed}$ vs ϕ

Figure 31: Algorithmic efficiency of the stand-alone muon reconstruction as a function of η and ϕ, for different p_{T} samples.

Table 5: Integrated efficiencies for the stand-alone muon reconstruction.

p_{T} sample (GeV/c)	ε_{sa} (%)
5	$96.2869 \pm 7.76e-02$
10	$98.8239 \pm 3.48e-02$
100	$98.7639 \pm 5.04e-02$
200	$98.5380 \pm 6.38e-02$
500	$97.6514 \pm 6.91e-02$
1000	$96.4173 \pm 1.72e-01$
2000	$94.8493 \pm 1.35e-01$
3000	$93.7827 \pm 1.77e-01$

The overall integrated efficiency, for momenta above 10 GeV/c, is more than 97% (Fig. 39). For low momenta the efficiency decreases because of two effects, one is energy loss in the material before the muon stations and the second is the increased bending in the magnetic field.

In order to decouple the algorithmic efficiency from the muon system acceptance we select simulated tracks that leave more than a given number of simulated hits in the muon detector since it is only the muon acceptance that results in lost hits. We then determine the reconstruction efficiency to find a seed or a track as a function of the minimum required number of *true* hits in the detector. In Fig. 32 this efficiency is shown both for the seed, $\varepsilon_{seed}(n^{min}_{simhits})$, and for the whole stand-alone muon reconstruction, $\varepsilon_{sa}(n^{min}_{simhits})$. As a cross check $\varepsilon_{sa,seed}(n^{min}_{simhits})$ is also evaluated. The curves are integral and the n^{th} point means: only simulated tracks with *n or more* associated simulated hits in the muon spectrometer are selected and used to calculate the efficiency.

The curves show the expected trend of a monotonic increase reaching a plateau. Two regions can be identified for muons less than a TeV, one is from 0 to about 9 hits and the other from 9 to the plateau. The first interval is defined by the minimum number of reconstructed hits required to have a segment in either a CSC or DT station in addition to an RPC measurement. Requiring at least 9 simulated hits is equivalent to having at least two segments in the muon system. The curves asymptotically reach a maximum, which is the efficiency for the reconstruction of a high quality muon. For the TeV-muons the pattern recognition efficiency (Fig. 32) decreases above 24 hits. This is due to the high probability that a TeV-muon emits a photon during the energy loss process, leading to an electromagnetic shower in the spectrometer. Many segments are generated and the probability of building fake segments (or segments with incorrect parameters) increases considerably, reducing the algorithmic efficiency of the pattern recognition. Therefore, for TeV-muons, the requirement on the *minimum* number of simulated hits is no longer a useful parameter for establishing the quality of the track, and $\varepsilon(n_{simhits})$ should be evaluated instead.

The value at the plateau gives the efficiency divided by the acceptance and the loss in efficiency due to the muon spectrometer acceptance is the difference between the value at the plateau and the value at the origin. The final result is that the loss in efficiency in the muon track reconstruction is entirely due to the acceptance.

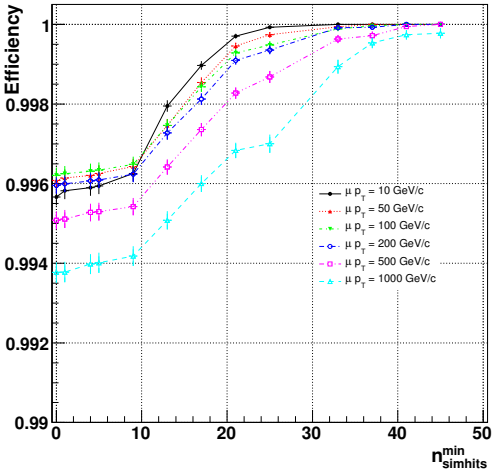

(a) ε_{seed} vs $n^{min}_{simhits}$.

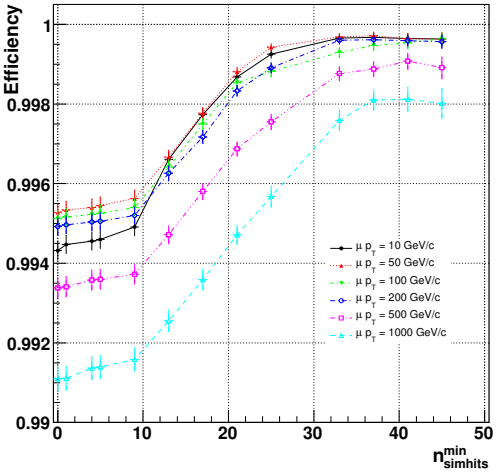

(b) ε_{sa} vs $n^{min}_{simhits}$.

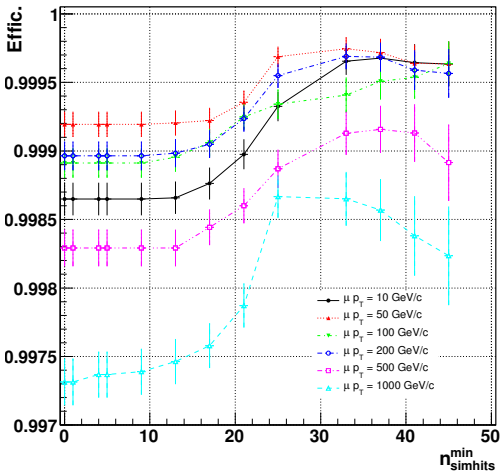

(c) $\varepsilon_{sa,seed}$ vs $n^{min}_{simhits}$.

Figure 32: Efficiency as a function of the minimum required number of simulated hits in the muon spectrometer.

In the case of real data one could use this technique, but with reconstructed hits, and a tag and probe method to determine the algorithmic efficiency and the effect of acceptance on the stand-alone muon reconstruction.

7.1.2 Inner tracker reconstruction

The inner tracker is less affected by multiple scattering and energy loss than the muon system. Moreover the magnetic field in the tracker volume is homogeneous and almost constant. In Fig. 33 and Fig. 34 the efficiency as a function of pseudorapidity and ϕ, for different p_{T} samples, is shown for general tracker tracks and tracker muons (Section 6). The integrated efficiency is almost constant for all p_{T} values (Table 6 and Fig. 33, and Table 7 and Fig. 34) and its value is above 99%. The dip at $\eta \simeq 0$ is due to the tracker geometry. The tracker is made of two half-barrels joined together, and the junction surface is at $\eta = 0$.

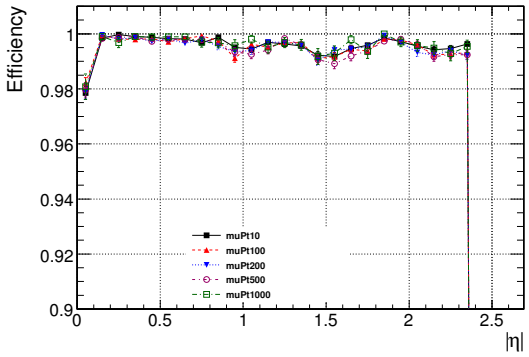

(a) ε_{tk} vs η

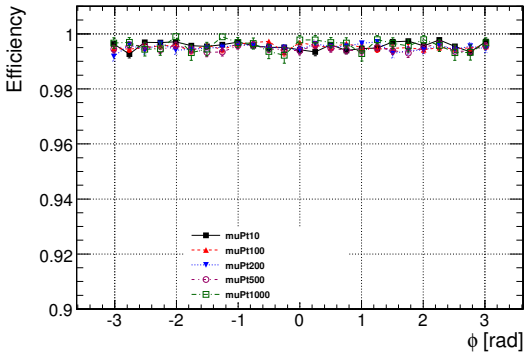

(b) ε_{tk} vs ϕ

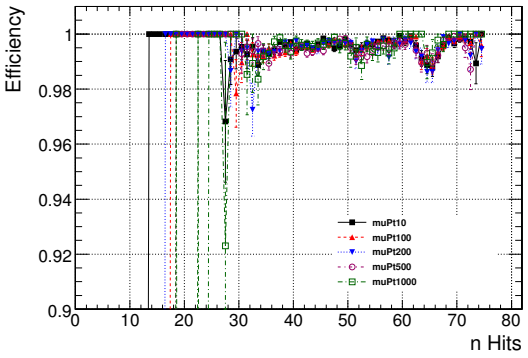

(c) ε_{tk} vs n Hits

Figure 33: Efficiency of the reconstruction in the inner tracker system and muon spectrometer as a function of η, ϕ, p_{T}, and number of hits for different p_{T} samples.

7.1.3 Global reconstruction

Global reconstruction requires the matching of reconstructed tracks in both the muon system and the tracker and the overall efficiency is a product of the stand-alone, the tracker track and the matching efficiencies.The results are shown in the following figures: (Fig. 35) shows the global efficiency ε_{glb}, $\varepsilon_{glb,sa} = \varepsilon_{glb}/\varepsilon_{sta}$, (Fig. 37) shows $\varepsilon_{glb,tk}$, and (Fig. 36) shows $\varepsilon_{glb}/\varepsilon_{tk}$.

The efficiency plot shown in Fig. 35 exhibit a number of lower efficiency structures which correspond to discontinuities in the geometry of the detector as mentioned in Section 7.1.1 and Section 7.1.2. These are as follows:

- $\eta \simeq 0$: junction surface between the two tracker barrels;
- $|\eta| \simeq 0.3$: inter-space between the DT central wheel and its neighbours;
- $0.8 < |\eta| < 1.2$: problematic region for seed estimation (DT and CSC overlap);

Table 6: Integrated efficiencies for the tracker tracks reconstruction.

p_{T} sample (GeV/c)	ε_{tk} (%)
5	$99.4801 \pm 2.95e-02$
10	$99.5618 \pm 2.13e-02$
100	$99.4848 \pm 3.26e-02$
200	$99.5174 \pm 3.68e-02$
500	$99.4920 \pm 3.24e-02$
1000	$99.6238 \pm 5.66e-02$
2000	$99.4688 \pm 4.45e-02$
3000	$99.4547 \pm 5.38e-02$

Table 7: Integrated efficiencies for the tracker tracks reconstruction.

p_{T} sample (GeV/c)	ε_{tk} (%)
5	$98.0198 \pm 5.71e-02$
10	$98.9842 \pm 3.23e-02$
100	$99.2542 \pm 3.92e-02$
200	$99.3875 \pm 4.14e-02$
500	$99.3545 \pm 3.65e-02$
1000	$99.4613 \pm 6.77e-02$
2000	$99.1846 \pm 5.50e-02$
3000	$98.9629 \pm 7.41e-02$

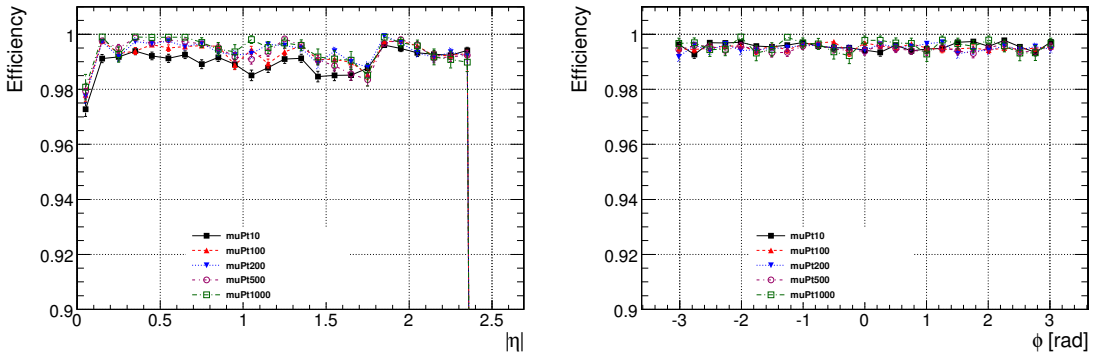

(a) ε_{tkmu} vs η

(b) ε_{tkmu} vs ϕ

Figure 34: Efficiency of the reconstruction of the tracker muons as a function of η and ϕ, for different p_{T} samples.

- $|\eta| \simeq 1.8$: problematic region for tracker track reconstruction (transition from TID to TID/TEC subsystem);
- $\phi \simeq 1.2$: barrel inactive region (chimney), because of instrumentation services;
- periodic structure in phi: loss in efficiency in the stand-alone muon reconstruction due to muons which escape in the space between two adjacent sectors (Fig. 2) or chambers in CSCs (although all chambers overlap in ϕ, except those in ME1/3). See also the effect on the parameter resolutions in Fig. 54.

The $\varepsilon_{matching}$ is shown in (Fig. 38) as a function of η and ϕ and the integrated efficiencies are shown in Table 8. The matching efficiency is above 99% over all the p_{T} spectra down to 5 GeV/c, where it is around 91%. This drop in efficiency for low p_{T} is due to muon seed parameters which are poorly estimated and this directly affects the stand-alone muon reconstruction and the subsequent matching with the tracker tracks. This efficiency can be improved by tuning the seed parameters for low p_{T} muons. $\varepsilon_{glb,sta}$ shows that the stand-alone muon efficiency dominates the final muon reconstruction efficiency.

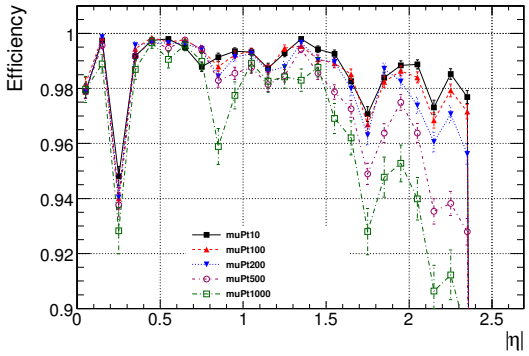

(a) ε_{glb} vs η

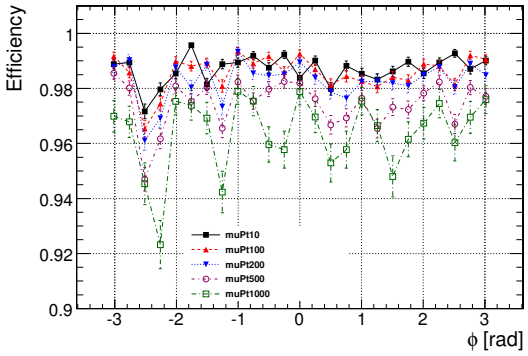

(b) ε_{glb} vs ϕ

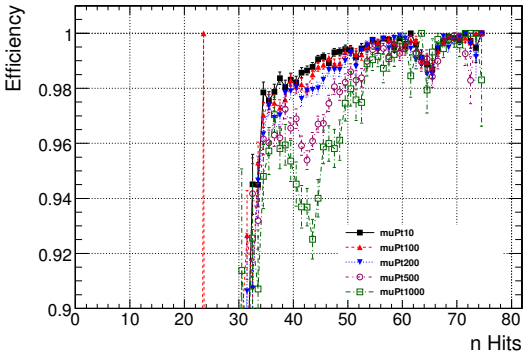

(c) ε_{glb} vs n Hits

Figure 35: Efficiency of the reconstruction in the inner tracker system and muon spectrometer as a function of η, ϕ, p_{T}, and number of hits for different p_{T} samples.

Table 8: Integrated efficiencies for the global muon reconstruction.

p_{T} sample (GeV/c)	ε_{glb} (%)	$\varepsilon_{glb,sa}$ (%)	$\varepsilon_{glb,tk}$ (%)
5	$89.3923 \pm 1.26e-01$	$89.5432 \pm 0.00e+00$	$89.8595 \pm 0.00e+00$
10	$98.6949 \pm 3.66e-02$	$99.4152 \pm 0.00e+00$	$99.1292 \pm 0.00e+00$
100	$98.5666 \pm 5.42e-02$	$99.5024 \pm 0.00e+00$	$99.0770 \pm 0.00e+00$
200	$98.2727 \pm 6.92e-02$	$99.4146 \pm 0.00e+00$	$98.7493 \pm 0.00e+00$
500	$97.5098 \pm 7.11e-02$	$99.2748 \pm 0.00e+00$	$98.0077 \pm 0.00e+00$
1000	$96.3489 \pm 1.73e-01$	$99.0738 \pm 0.00e+00$	$96.7127 \pm 0.00e+00$
2000	$94.9428 \pm 1.34e-01$	$98.8839 \pm 0.00e+00$	$95.4498 \pm 0.00e+00$
3000	$93.8362 \pm 1.76e-01$	$98.6593 \pm 0.00e+00$	$94.3507 \pm 0.00e+00$

The Fig. 39 shows a direct comparison of the reconstruction efficiencies: ε_{seed}, ε_{sa}, ε_{tk} and ε_{glb}, as a function of p_{T}, η and ϕ. The plots have been made using the flat p_{T} sample described in Table 4. The values are almost the same for $p_{\mathrm{T}} \geq 10$ GeV/c. The structure visible in the efficiency as a function of ϕ, for the seed, stand-alone and global reconstruction, is due to the ϕ-acceptance of the muon system, as discussed in Section 7.2.

The efficiency as a function of the muon transverse momentum is shown in (Fig. 39). The muon reconstruction efficiency increases up to a plateau which is approximately constant from 8 GeV/c to 1 TeV/c (starting from $p_{\mathrm{T}} = 5$ GeV/c more than 50% of muons are reconstructed). At TeV momenta the muon reconstruction efficiency decreases slowly, due to the effects of bremsstrahlung on finding correct seeds.

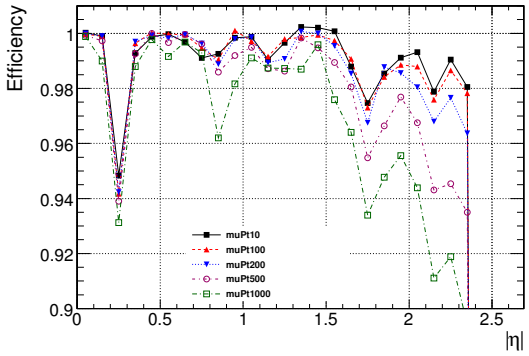

(a) $\varepsilon_{glb,tk}$ vs η

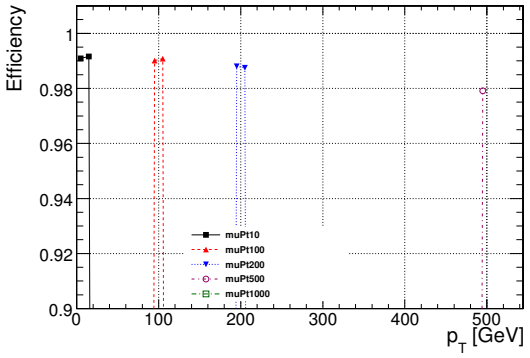

(b) $\varepsilon_{glb,tk}$ vs p_{T}

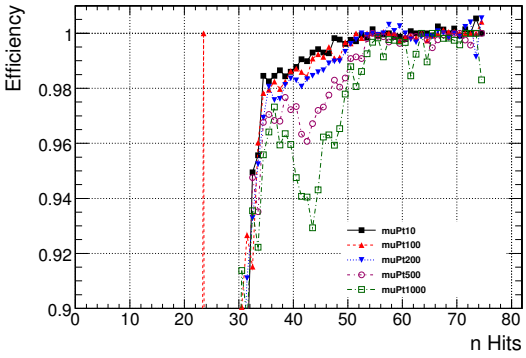

(c) $\varepsilon_{glb,tk}$ vs n hits

Figure 36: Efficiency of the reconstruction in the inner tracker system and the muon spectrometer as a function of η, p_{T}, and n hits for different p_{T} samples.

The tracker efficiency is stable above 1 GeV/c so the loss in efficiency at low p_{T} is due to the muon identification efficiency. The conclusion from the analysis is that high reconstruction efficiency in the tracker together with the muon spectrometer ensure a robust muon identification system with minimal losses.

7.1.4 Data-Driven Efficiency Measurements

For early CMS data-sets, reliance on efficiency predications from Monte Carlo (MC) simulation will produce large systematic errors due to imperfections in modelling both the data and the detector response. Ideally therefore, we would like to measure particle efficiencies from the data itself, with no reference to simulation. The problem then becomes one of identifying the desired particle types in data with a small, or easily subtracted, fake rate. One well established data-driven approach to measuring particle efficiencies is the so called “Tag and Probe” method [11].

The Tag and Probe method utilizes a known mass resonance (e.g. J/Ψ, Υ, Z) to select particles of the desired type, and probe the efficiency of a particular selection criterion on those particles. In general the “tag” is an object that passes a set of very tight selection criteria designed to isolate the required particle type. In the case of muons, the tag will in general be a global muon with some additional p_{T} cuts imposed such that the fake-rate is very small. A generic set of the desired particle type (i.e. with potentially very loose selection criteria) known as “probes” is selected by pairing these objects with tags such that the invariant mass of the combination is consistent with the mass of the resonance. Combinatoric backgrounds may be eliminated through any of a variety of background subtraction methods such as fitting, or sideband subtraction. The definition of the probe object depends on the specifics of the selection criterion being examined. The efficiency itself is measured by counting the number of “probe” particles that pass the desired selection criteria:

$$\varepsilon = \frac{P_{\mathrm{pass}}}{P_{\mathrm{all}}}, \tag{5}$$

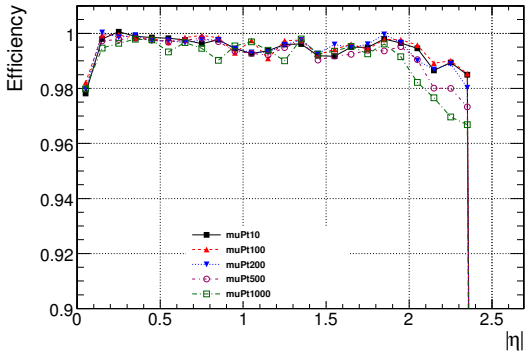

(a) $\varepsilon_{glb,sta}$ vs η

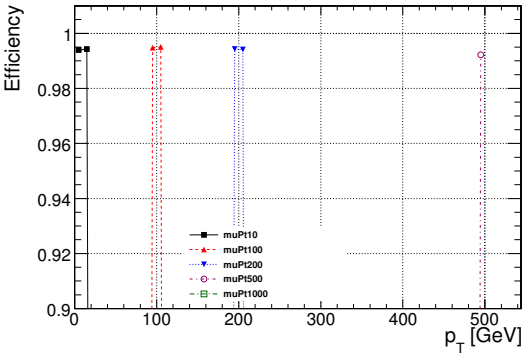

(b) $\varepsilon_{glb,sta}$ vs p_{T}

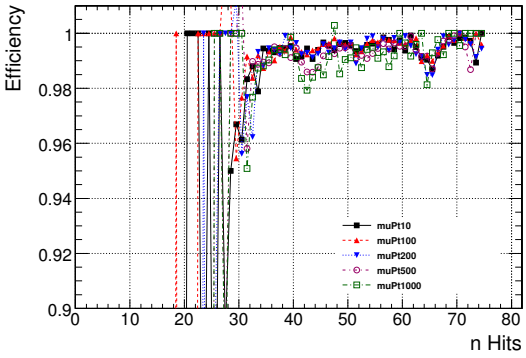

(c) $\varepsilon_{glb,sta}$ vs n hits

Figure 37: Efficiency of the reconstruction in the inner tracker system and the muon spectrometer as a function of η, p_{T}, and n hits for different p_{T} samples.

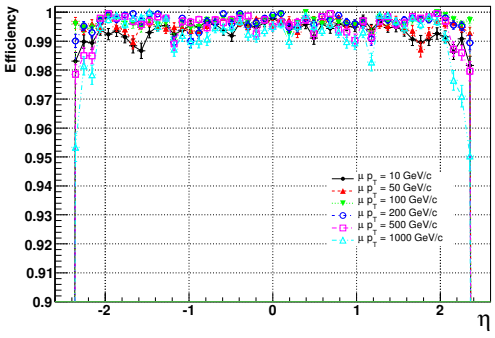

(a) $\varepsilon_{matching}$ vs η

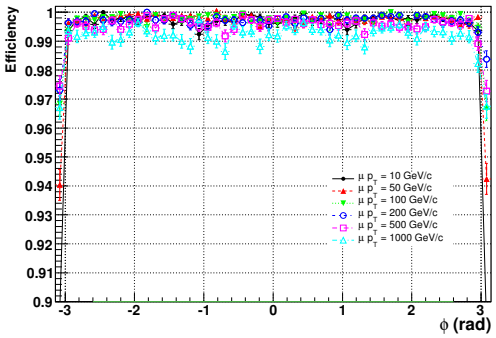

(b) $\varepsilon_{matching}$ vs ϕ

Figure 38: Matching efficiency between muon and tracker tracks, as a function of η and ϕ, for different p_{T} samples.

where P_{pass} is the number of probes passing the selection criteria and P_{all} is the total number of probes counted using the resonance. It is worthwhile to note that in some cases a probe object will also pass the tag selection criteria. In this case it will appear in both the tag and probe lists, and produce a double pairing in the same event. The efficiency formula as written above accounts for these double pairings.

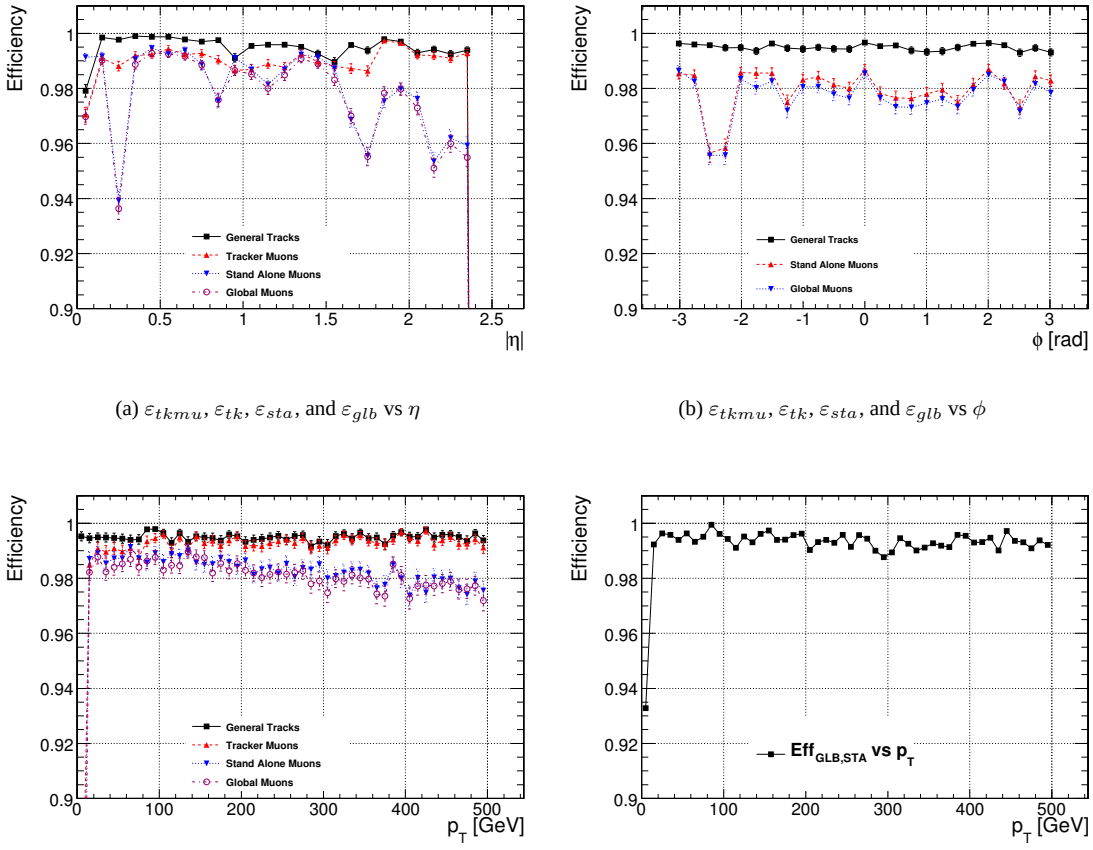

(a) ε_{tkmu}, ε_{tk}, ε_{sta}, and ε_{glb} vs η

(b) ε_{tkmu}, ε_{tk}, ε_{sta}, and ε_{glb} vs ϕ

(c) ε_{tkmu}, ε_{tk}, ε_{sta}, and ε_{glb} vs p_{T}

(d) $\varepsilon_{glb,sta}$ vs p_{T}

Figure 39: Efficiencies of the different muon reconstruction steps as a function of η, ϕ and p_{T}.

A generic[4)] Tag and Probe tool that carries out the data-driven efficiency measurements described above has been designed for the CMS software. Details and example efficiency measurements can be found in [12]. Here we give a couple of examples of muon efficiency measurements from the Z and Υ resonances.

For muons the total efficiency measurement can be broken down (factorized) into five sequential measurements. The five steps are: muon tracking efficiency, stand-alone muon reconstruction efficiency, identification efficiency, isolation efficiency and the online or total trigger efficiency. The total efficiency is thus given by the product

$$\varepsilon_{\mathrm{total}} = \varepsilon_{\mathrm{trk}} \times \varepsilon_{\mathrm{sta}} \times \varepsilon_{\mathrm{id}} \times \varepsilon_{\mathrm{iso}} \times \varepsilon_{\mathrm{online}}. \quad (6)$$

In Fig. 40 we show an example of the fit output from the CMS Tag and Probe tool at the Z resonance. The example fit is shown for a particular p_{T} and η range in the measurement of muon stand-alone reconstruction efficiency (step two in Eq. 6). For the stand-alone muon reconstruction efficiency we take the set of all probes to be all tracks from the inner (silicon) trackers. A passing probe is then a probe that is also matched (geometrically) to a stand-alone muon track.

In Fig. 41 we show an example of the fit output from the CMS Tag and Probe tool at the Υ(1S) resonance. The example fit is shown for a particular p_{T} and η range in the measurement of muon identification efficiency (step three in Eq. 6). The identification efficiency is the probability that give a tracker track and a stand-alone muon track have been found (for the same muon) a global muon track is also reconstructed. A probe is therefore a muon that has a tracker track and a stand-alone track, while a passing-probe also has a valid global muon fit.

Finally in Fig. 42 we show example agreements between MC truth and the tag and probe tool measured efficiencies for 2D fit efficiency output at the Z resonance. For complete details of the tag and probe tool results, and full example measurements for both electrons and muons we refer the reader once again to [12].

[4)] The Tag and Probe tool is generic in the sense that it cna be used for any resonance, and for either electrons or muons.

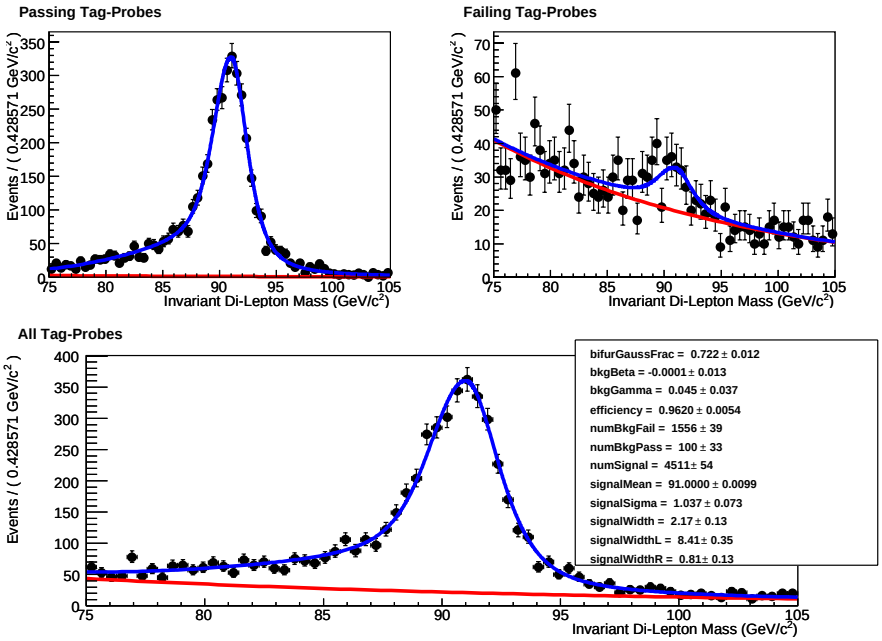

Figure 40: Tag and Probe Z reconstruction efficiency: Multiple bin fit $30.0 < p_{\mathrm{T}} < 40.0$ GeV/c, $-2.4 < \eta < 2.4$.

7.2 Resolutions and Residuals

In this section we analyse the track resolutions and residuals and in addition two parameters of particular interest for the physics analysis, the pseudorapidity and q/p_{T}. To describe a track, the following information is used:

- a reference position on the track ($\mathbf{v}$).For tracks reconstructed in the tracker, the reference position is the point of closest approach to the centre of CMS.
- the momentum at the reference point on the track
- 5D curvilinear covariance matrix resulting from the track fit
- the charge, the χ^2 and the number of degrees of freedom
- a summary of the information on the collected hits

For muons produced from the decays of long-lived particles the reference position would not be the center of CMS, however, for the samples used in the present analysis this is the case. The parameters associated with the 5D curvilinear covariance matrix are: q/p, λ, ϕ, d_{xy}, d_{sz}. These are defined as:

- $q/|\mathbf{p}|$ = signed inverse of momentum expressed in (GeV/c)$^{-1}$;
- λ = complement to $\pi/2$ of the polar angle at the given point;
- ϕ = azimuthal angle at the given point;
- $d_{xy} = -v_x \sin\phi + v_y \cos\phi$, expressed in cm. Geometrically, d_{xy} is the signed distance in the (x,y) plane between the point (0,0) and the straight line passing through (v_x,v_y) with azimuthal angle ϕ. It coincides with the impact parameter with respect to (0,0,0) only if the reference point is close to (0,0,0). In other parametrisations it is also called d_0 ($d_0 = -d_{xy}$).
- $d_{sz} = v_z \cos\lambda - (v_x \cos\phi + v_y \sin\phi)\sin\lambda$ expressed in cm. The d_{sz} parameter is the signed distance in the (s,z) plane between the point ($s = 0$,$z = 0$) and the straight line passing through $\mathbf{v}$ with angles (ϕ,λ). The s-axis is defined by the projection of the straight line onto the (x,y) plane. The convention is to assign the s coordinate for (v_x,v_y) as the value $v_x \cos\phi + v_y \sin\phi$. This value is zero when (v_x,v_y) is the point of minimum transverse distance to (0,0). A more intuitive parameter, which represents the track position along the beam axis, is $d_z = d_{sz}/\cos\lambda$.

Note that d_{xy} and d_z provide sensible estimates of the distance from the true particle trajectory to the IP only in two cases:

1. when $\mathbf{v}$ already corresponds to the point of minimum transverse distance to the IP or it is close to it (so that the differences between considering the exact trajectory or a straight line are negligible).
2. When the track has very high momentum.

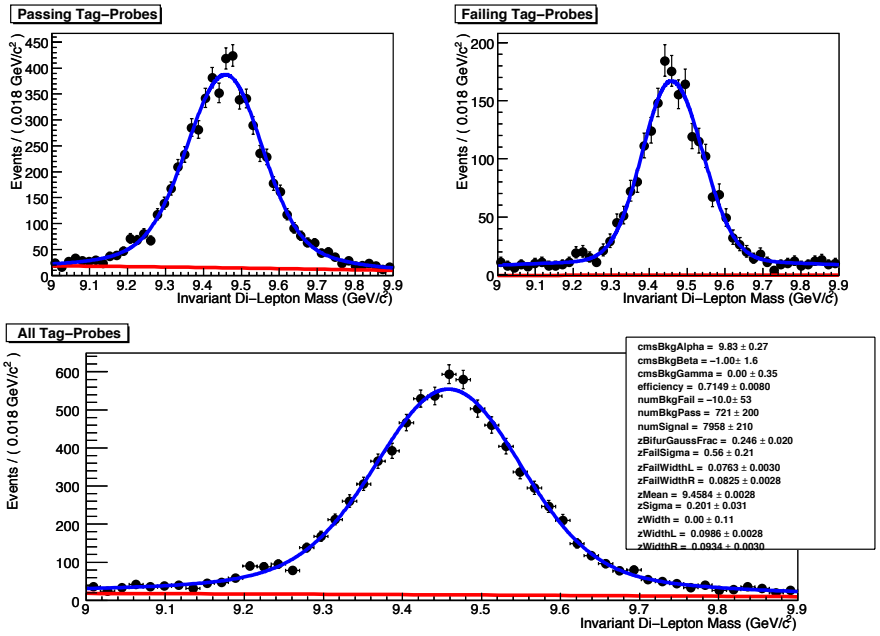

Figure 41: Υ(1S) identification efficiency: Multiple bin fit: $3.0 < p_{\mathrm{T}} < 5.0$ GeV/c, $0 < \eta < 2.4$.

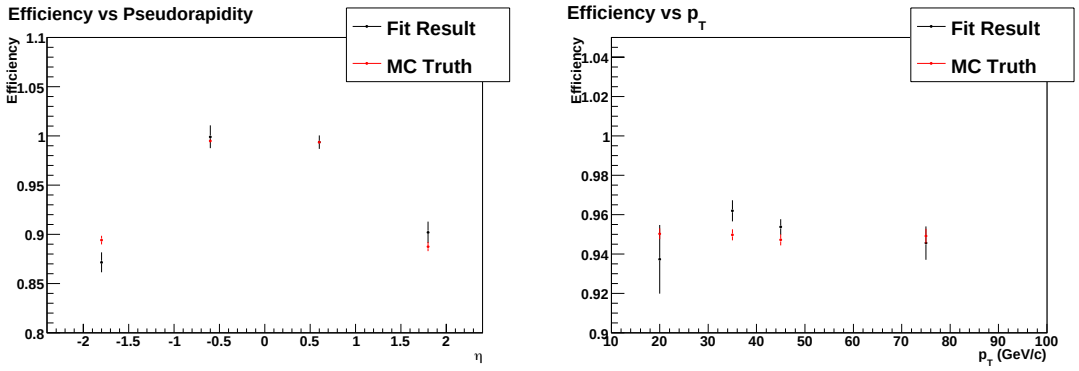

(a) Stand-alone muon reconstruction efficiency vs η.

(b) Stand-alone muon reconstruction efficiency vs p_{T}.

Figure 42: Comparison of the results of the efficiency measurements from the CMS Tag and Probe tool with the same efficiencies from MC truth. The examples are from one piece of the overall efficiency measurement, namely the stand-alone muon reconstruction efficiency.

There are two more parameters of particular interest for the physics analysis: the pseudorapidity and q/p_{T}. Since η and λ are closely related, only the former is studied here. We choose q/p_{T} as the variable of interest because q/p_{T} is, locally, directly proportional to the curvature in the bending plane, which is what is measured by the tracking system.Moreover q/p_{T} is more suitable than p_{T} because it distributes normally around the true value. The resolution on this parameter is defined as the Gaussian width of:

$$\frac{\delta(\frac{q}{p_{\mathrm{T}}})}{\frac{q}{p_{\mathrm{T}}}} = \frac{q^{\mathrm{rec}}/p_{\mathrm{T}}^{\mathrm{rec}} - q^{\mathrm{sim}}/p_{\mathrm{T}}^{\mathrm{sim}}}{q^{\mathrm{sim}}/p_{\mathrm{T}}^{\mathrm{sim}}}, \tag{7}$$

where q is the charge and $p_{\mathrm{T}}^{\mathrm{sim}}$ and $p_{\mathrm{T}}^{\mathrm{rec}}$ are the simulated and reconstructed transverse momenta, respectively. In the following the resolution is indicated as $R(\frac{q}{p_{\mathrm{T}}})$. Summarizing, in this section the following quantities are studied: the resolution on q/p_{T} and the residuals of ϕ, η, d_{xy} and d_z, where the residual for a variable a is defined as the Gaussian width of:

$$\delta a = a^{rec} - a^{gen}.$$

and we use the notation for the residual $R(a)$.

7.2.1 Analysis of $R(q/p_{\mathrm{T}})$

The q/p_{T} resolutions as function of η and ϕ, for the stand-alone muon reconstruction are shown in Fig. 43, and Fig. 44. The resolution for the stand-alone muon reconstruction ranges from 8% in the barrel, for the 10 GeV/c p_{T} sample, to 40% at 2.4 for the TeV-muons, matching the design performance of the muon system [13]. The peak in the spectra corresponds to the problematic regions already discussed in the analysis of the efficiencies. The resolution degrades as the pseudorapidity increases. This is due to the more complex environment in which the endcaps are embedded: the integral of the magnetic field decreases, the magnetic field has large inhomogeneities and it is no longer solenoidal. As an example, for muons with a momentum of 100 GeV/c the sagitta measured at $|\eta| \sim 2.4$ is five times smaller than the sagitta measured at $|\eta| \sim 1.6$. The q/p_{T} resolution as a function of ϕ reflects the periodic structure of the CMS apparatus (Fig. 54), moreover it shows the improvement obtained passing from a parameterized estimation (the seed) to a true fit.

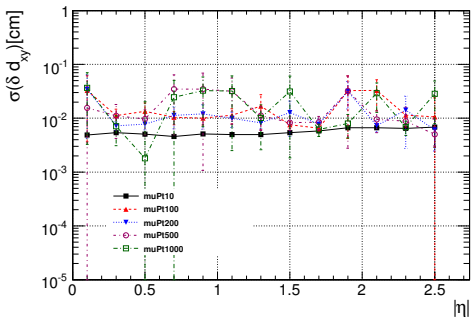

(a) Resolution of d_{xy} parameter.

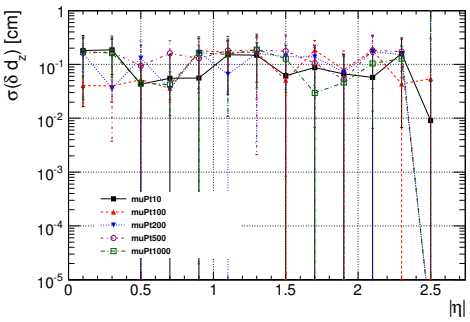

(b) Resolution of d_z parameter.

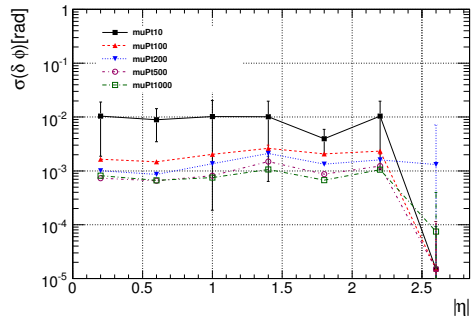

(c) Resolution of ϕ parameter.

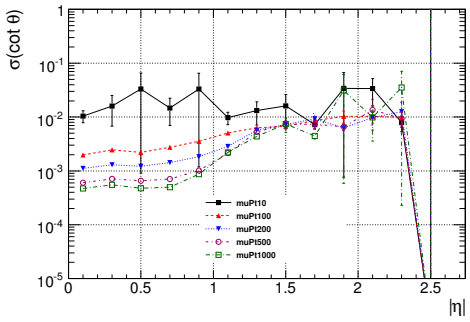

(d) Resolution of θ parameter.

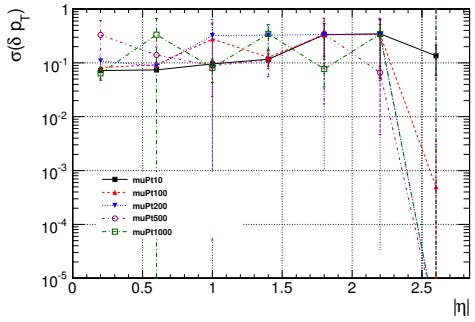

(e) Resolution of pt parameter.

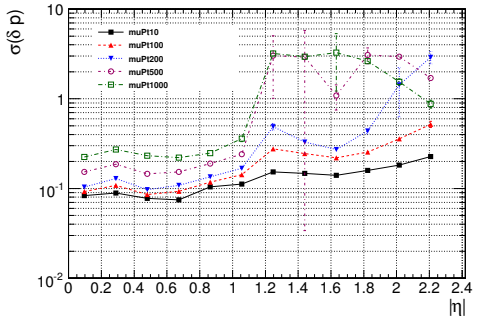

(f) Resolution of p parameter.

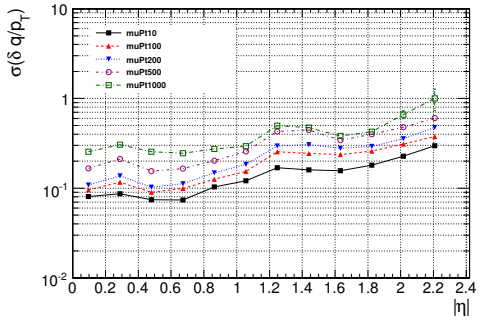

(g) Resolution of q/pt parameter.

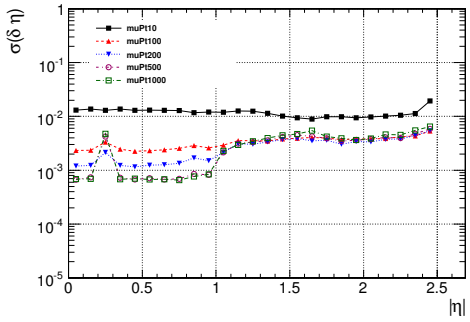

(h) Resolution of η parameter.

Figure 43: The resolution of the track parameters vs η for the stand-alone muon reconstruction step.

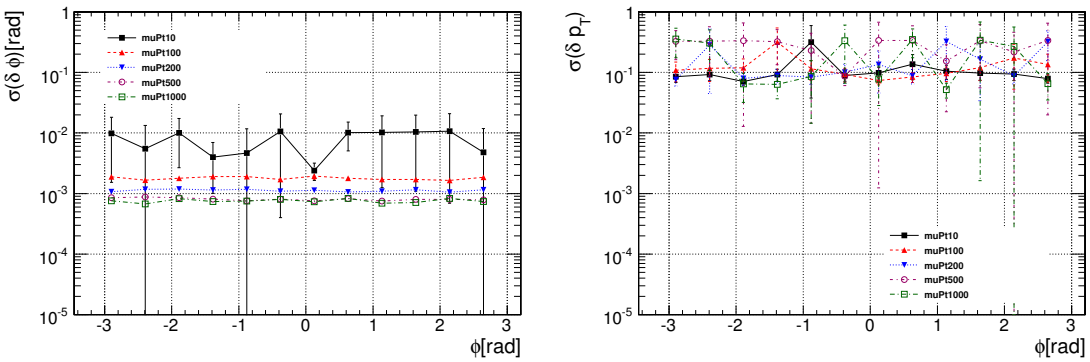

(a) Resolution of ϕ parameter.

(b) Resolution of pt parameter.

Figure 44: The resolution of the track parameters vs ϕ for the stand-alone muon reconstruction step.

We have also evaluated the effect of the constraint at the vertex on the q/p_{T} resolution. In Table 9 the $R(q/p_{\mathrm{T}})$ values before and after the constraint at the vertex are reported. To better appreciate the improvement, the table has been divided in three pseudorapidity regions: barrel ($|\eta| < 0.8$), overlap ($0.8 < |\eta| < 1.2$) and end-caps ($1.2 < |\eta| \leq 2.4$).

An improvement is visible for all p_{T} values. In particular the high p_{T} muons gain a factor of two in the $R(q/p_{\mathrm{T}})$ resolution.The $R(q/p_{\mathrm{T}})$ distribution before the constraint at the IP is shown in Fig. 45.

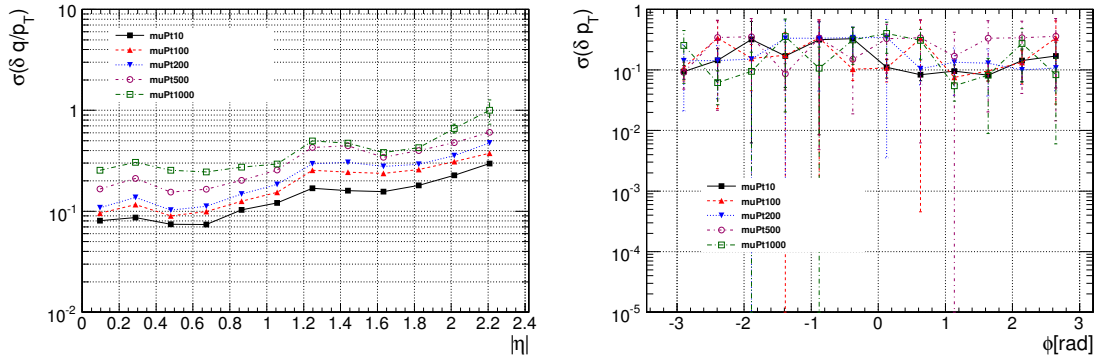

(a) stand-alone muons: $R(q/p_{\mathrm{T}})$ vs η.

(b) stand-alone muons: $R(q/p_{\mathrm{T}})$ vs ϕ.

Figure 45: stand-alone muon resolution on q/p_{T} before the constraint at the vertex as a function of η and ϕ, for different p_{T} samples. Cf. Fig. 43 and Fig. 44.

Table 9: Stand-alone muon resolution on q/p_{T} before and after the constraint at the vertex, divided by pseudorapidity regions.

p_{T} (GeV/c)	$R(q/p_{\mathrm{T}})$ (%) Before/after the vertex constraint		
	Barrel	Overlap	End-caps
1	$7.9485 \pm 8.83e-02$ / $6.4485 \pm 6.29e-02$	$13.2124 \pm 2.05e-01$ / $10.5128 \pm 1.35e-01$	$19.0881 \pm 1.79e-01$ / $15.8220 \pm 1.15e-01$
5	$9.9973 \pm 9.94e-02$ / $7.8819 \pm 7.12e-02$	$15.9312 \pm 2.02e-01$ / $11.7424 \pm 1.17e-01$	$23.2980 \pm 1.77e-01$ / $18.0582 \pm 1.07e-01$
10	$14.3658 \pm 1.15e-01$ / $9.8071 \pm 6.04e-02$	$25.0216 \pm 3.04e-01$ / $14.1826 \pm 1.15e-01$	$40.0438 \pm 4.12e-01$ / $26.0345 \pm 1.70e-01$
100	$17.0478 \pm 1.55e-01$ / $11.1506 \pm 8.05e-02$	$30.5473 \pm 4.61e-01$ / $16.1216 \pm 1.51e-01$	$50.5167 \pm 8.39e-01$ / $29.7601 \pm 2.61e-01$
200	$26.5718 \pm 2.91e-01$ / $16.6844 \pm 1.34e-01$	$41.7092 \pm 9.14e-01$ / $21.2971 \pm 2.36e-01$	$49.2874 \pm 1.08e+00$ / $37.9941 \pm 4.56e-01$
500	$39.6101 \pm 9.34e-01$ / $26.4196 \pm 4.17e-01$	$50.4544 \pm 2.47e+00$ / $29.6941 \pm 8.11e-01$	$52.7794 \pm 3.13e+00$ / $51.2939 \pm 2.17e+00$
1000	$42.8473 \pm 8.92e-01$ / $29.9655 \pm 4.18e-01$	$49.1419 \pm 1.96e+00$ / $33.0219 \pm 8.27e-01$	$61.6579 \pm 3.31e+00$ / $61.3619 \pm 2.75e+00$
2000	$16.1882 \pm 8.53e-01$ / $41.1417 \pm 9.60e-01$	$42.8277 \pm 3.18e+00$ / $46.9792 \pm 2.52e+00$	$177.2653 \pm 3.91e+01$ / $119.2237 \pm 1.85e+01$

The $R(q/p_{\mathrm{T}})$ distributions for the track reconstruction in the tracker and for the global muon reconstruction are shown in Fig. 46, Fig. 48, Fig. 47, and Fig. 49. The two curves do not differ much for low-p_{T}; the main differences are at high η. The benefit of including the hits reconstructed in the muon chambers becomes evident for momenta greater than 200 GeV/c (Fig. 50). The main reason of this behaviour is related to the formula[5)]:

$$\frac{\delta p_{\mathrm{T}}}{p_{\mathrm{T}}} = \frac{0.0136}{\beta B L}\sqrt{\frac{x}{X_0}}\sqrt{\frac{4A_N}{N}} \oplus \frac{\sigma \cdot p_{\mathrm{T}}}{0.3BL^2}\sqrt{4A_N}, \tag{8}$$

where $\beta = v/c$, x/X_0 is the thickness of the scattering medium in radiation lengths, B is the magnetic field value, L the length of the tracking system, N the number of measurements, σ their individual errors and

$$A_N = \frac{180N^3}{(N-1)(N+1)(N+2)(N+3)}. \tag{9}$$

The first term represents the contribution of multiple scattering and it is constant with respect to p_{T}. This term is dominant in the stand-alone muon reconstruction particularly in the barrel and it has the effect of keeping the resolution almost constant up to 100 GeV/c. Above this value, the second term starts to become important. In the

[5)] eq. 8 is not directly used in the CMS track reconstruction because it neglects the magnetic field inhomogeneities, in particular in the muon system, and the very complex geometry. Nevertheless the general features extracted from it are also valid for the real CMS tracking system.

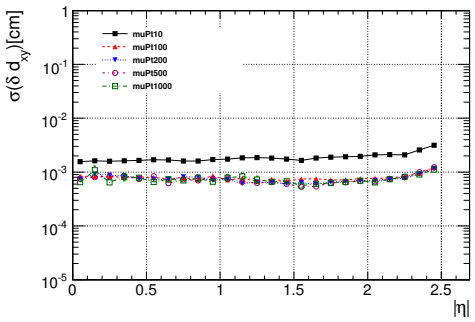

(a) Resolution of d_{xy} parameter.

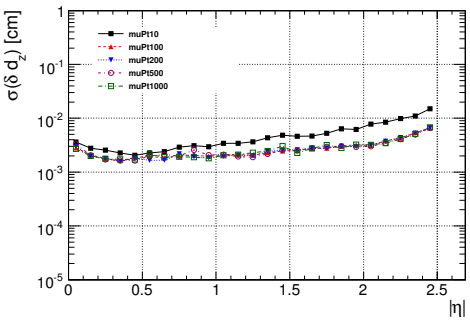

(b) Resolution of d_z parameter.

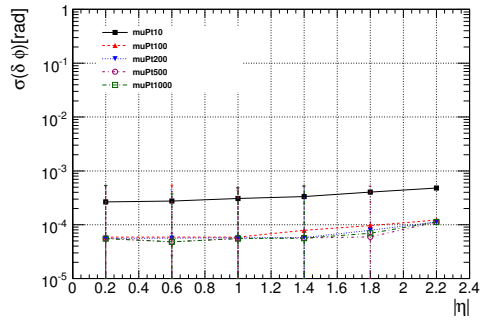

(c) Resolution of ϕ parameter.

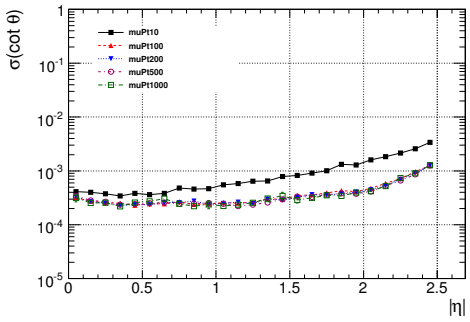

(d) Resolution of θ parameter.

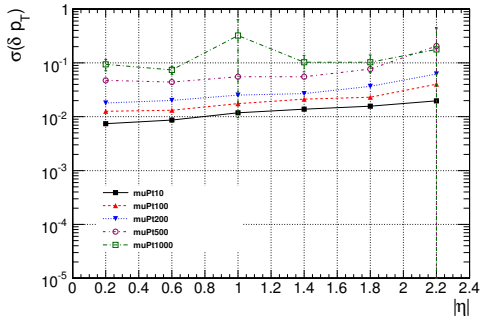

(e) Resolution of pt parameter.

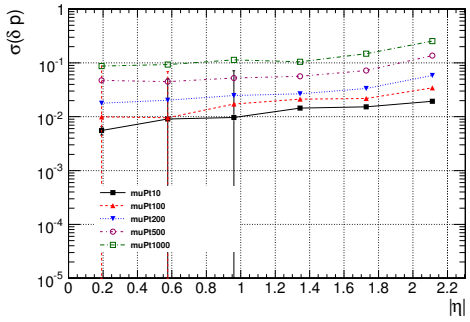

(f) Resolution of p parameter.

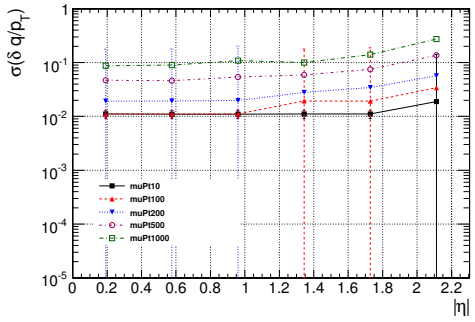

(g) Resolution of q/pt parameter.

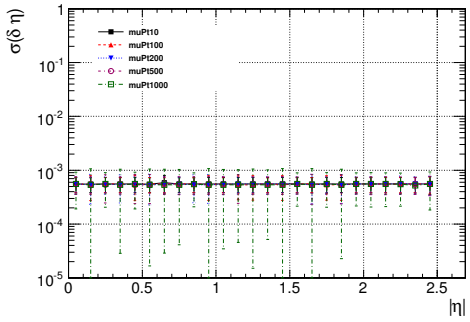

(h) Resolution of η parameter.

Figure 46: The resolution of the track parameters for the general track reconstruction step.

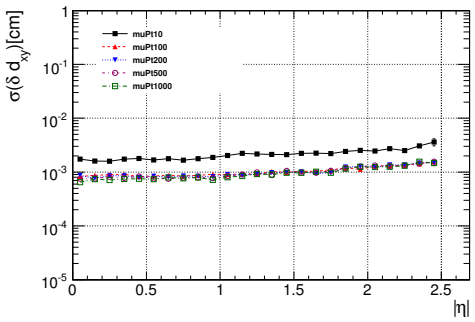

(a) Resolution of d_{xy} parameter.

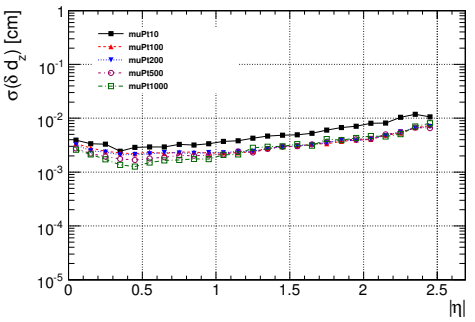

(b) Resolution of d_z parameter.

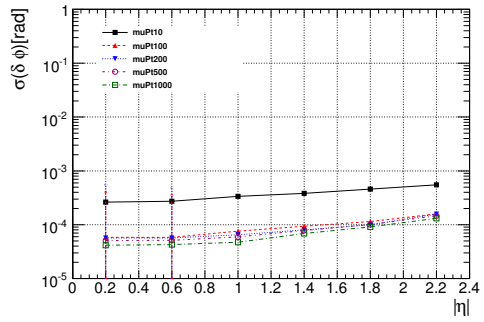

(c) Resolution of ϕ parameter.

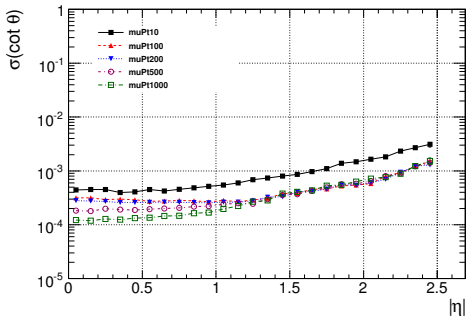

(d) Resolution of θ parameter.

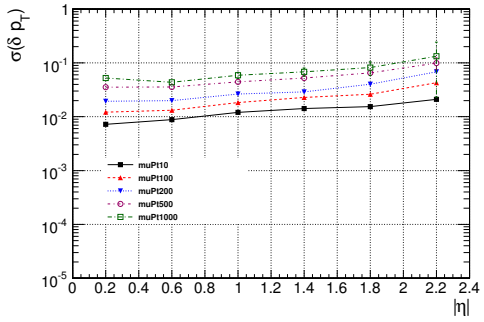

(e) Resolution of pt parameter.

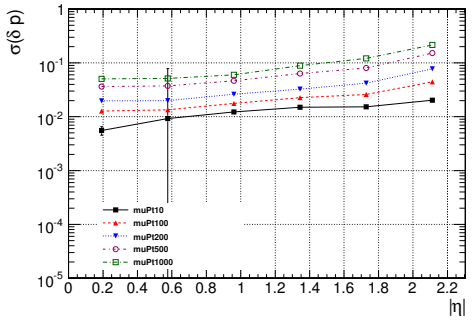

(f) Resolution of p parameter.

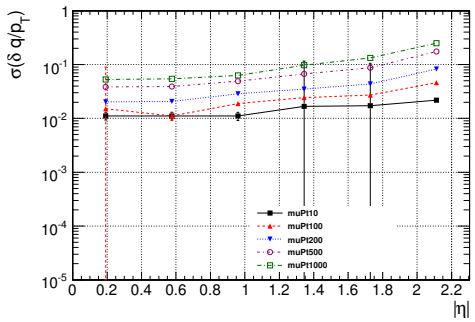

(g) Resolution of q/pt parameter.

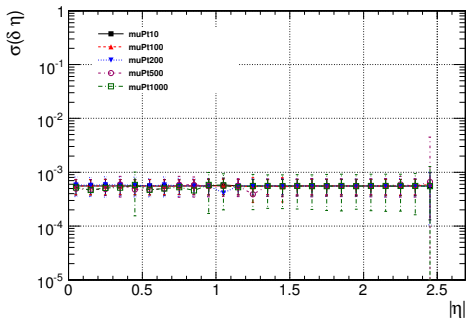

(h) Resolution of η parameter.

Figure 47: The resolution of the track parameters for the global muon reconstruction step.

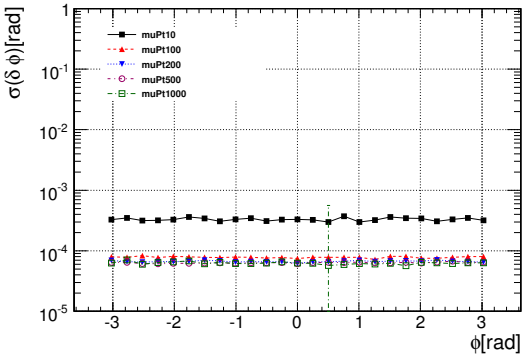

(a) Resolution of ϕ parameter.

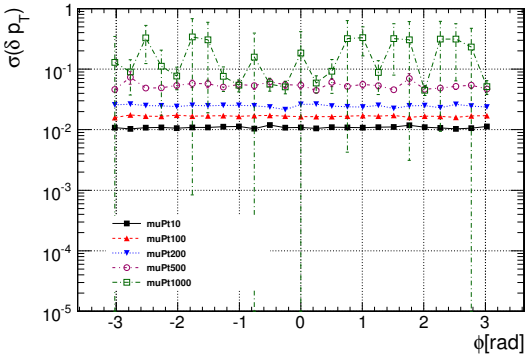

(b) Resolution of pt parameter.

Figure 48: The resolution of the track parameters for the general track reconstruction step.

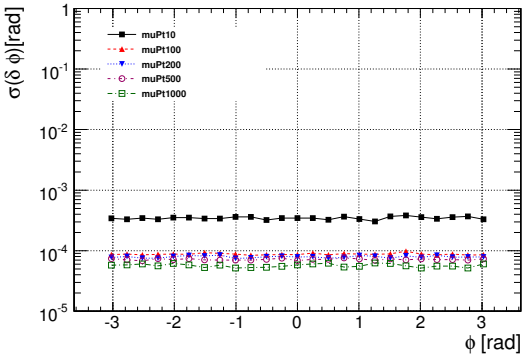

(a) Resolution of ϕ parameter.

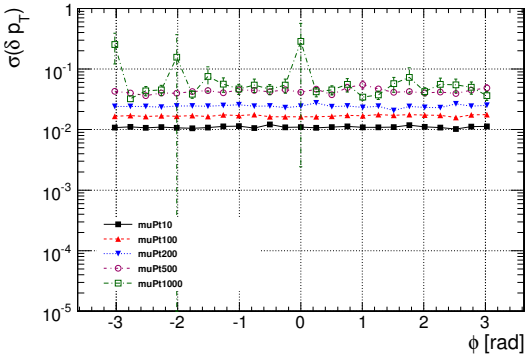

(b) Resolution of pt parameter.

Figure 49: The resolution of the track parameters for the global muon reconstruction step.

tracker the multiple scattering is lower than in the muon system and the dominant term is the one directly related to measurement precision. As the p increases, the measurement term becomes more and more important, but can be balanced by a a longer path length in the magnetic field (i.e. a larger L): this is accomplished using the tracker and the muon system together. The combination of the information from the tracker and the muon chamber ensures the best p estimation both at low and high momenta.

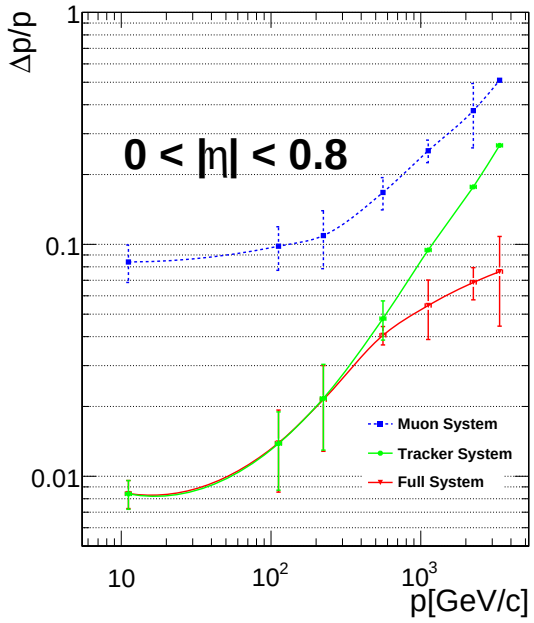

(a) Barrel.

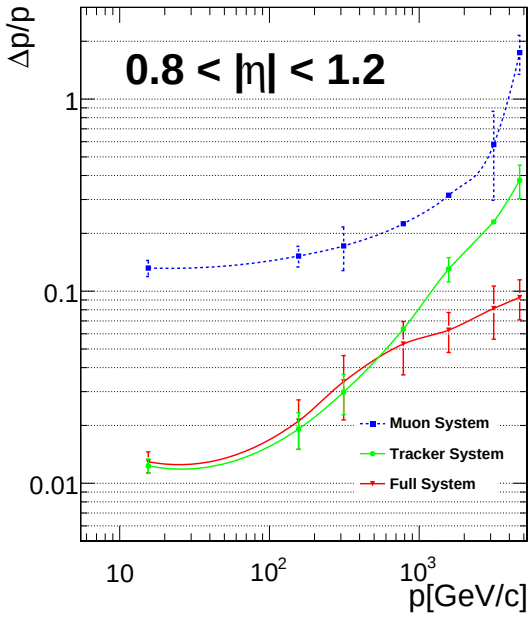

(b) Overlap.

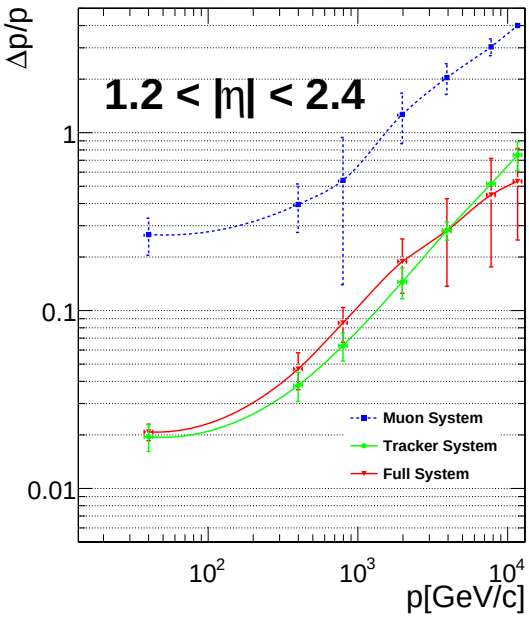

(c) End-caps.

Figure 50: Resolution on q/p with the tracker alone, with the muon spectrometer alone and with the full CMS tracking system, as a function of p.

In Table 10 a summary of the values of $R(q/p)$, in the barrel, overlap and endcap regions is shown for the global muon reconstruction and for the tracker track reconstruction. The values of $R(q/p)$ are obtained by fitting the

distribution to the $mean \pm 2 \times rms$, while its errors is obtained from a difference to the fits on the core and a wider range to take into account the tails of the distribution.

Table 10: Resolution on q/p_{T} divided by pseudorapidity regions for the different muon reconstruction steps.

p_{T} (GeV/c)	$R(q/p_{\mathrm{T}})$ (%) Tracker/Global		
	Barrel	Overlap	End-caps
1	$1.0997 \pm 1.39e-01$ / $1.1600 \pm 7.48e-03$	$1.0939 \pm 1.82e-01$ / $1.3836 \pm 1.18e-02$	$1.1095 \pm 1.45e-01$ / $1.8934 \pm 1.29e-02$
5	$1.1047 \pm 1.25e-01$ / $1.1083 \pm 1.27e-01$	$1.1031 \pm 1.65e-01$ / $1.1263 \pm 2.09e-01$	$1.8445 \pm 8.84e-02$ / $2.2194 \pm 1.53e-02$
10	$1.1082 \pm 1.33e-01$ / $1.4016 \pm 1.83e-02$	$1.1111 \pm 2.78e-01$ / $2.2818 \pm 2.09e-02$	$3.4148 \pm 8.68e-02$ / $2.8430 \pm 1.29e-02$
100	$1.8686 \pm 5.01e+00$ / $2.1020 \pm 1.94e-02$	$3.1411 \pm 1.19e-01$ / $2.7556 \pm 2.30e-02$	$3.0690 \pm 4.55e-02$ / $4.2499 \pm 2.49e-02$
200	$4.6242 \pm 1.07e-01$ / $3.8540 \pm 2.44e-02$	$4.9621 \pm 1.68e-01$ / $4.8890 \pm 4.08e-02$	$7.5805 \pm 1.84e-01$ / $8.3065 \pm 5.81e-02$
500	$8.1466 \pm 3.24e-01$ / $5.3119 \pm 5.49e-02$	$9.9515 \pm 5.40e-01$ / $6.3021 \pm 9.54e-02$	$12.7971 \pm 4.93e-01$ / $11.7320 \pm 1.63e-01$
1000	$17.7836 \pm 5.15e-01$ / $6.5026 \pm 4.87e-02$	$20.4208 \pm 7.35e-01$ / $7.8332 \pm 7.87e-02$	$31.1789 \pm 8.79e-01$ / $16.3528 \pm 1.59e-01$
2000	$26.0926 \pm 8.89e-01$ / $7.1602 \pm 6.21e-02$	$29.7096 \pm 1.24e+00$ / $8.7524 \pm 1.10e-01$	$45.5004 \pm 1.58e+00$ / $13.6898 \pm 1.64e-01$

7.2.2 Charge Identification

The charge identification probability has been evaluated for the different stages of the reconstruction. In Fig. 51, Fig. 52, and Fig. 53 the probability to assign the correct charge is shown as a function of η and ϕ.

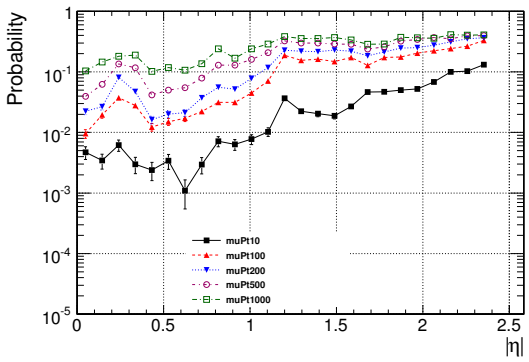

(a) Stand-alone charge mis-id vs η

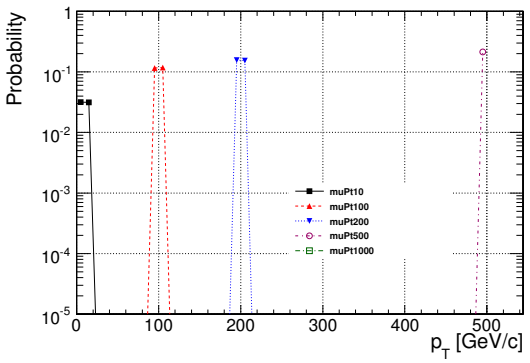

(b) Stand-alone charge mis-id vs p_{T}

Figure 51: Charge mis-assignment probability for stand-alone muons as a function of η and p_{T}, for different p_{T} samples.

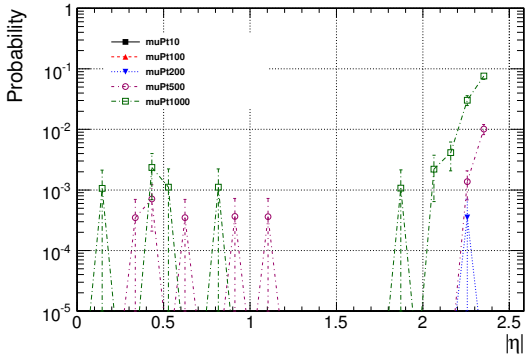

(a) General Track charge mis-id vs η

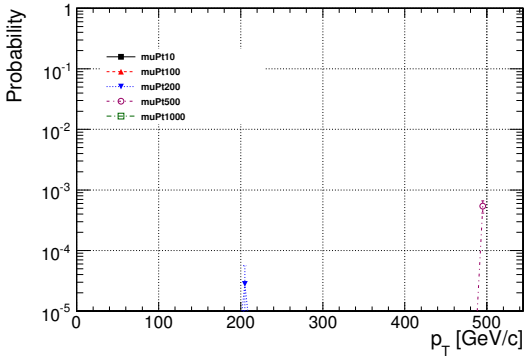

(b) General Track charge mis-id vs p_{T}

Figure 52: Charge mis-assignment probability for general track muons as a function of η and p_{T}, for different p_{T} samples.

The correct charge assignment probability in the muon spectrometer is above 75% for TeV-muons and reaches 99% for lower p_{T} muons. With the full tracking system the probability stays above 98%, even for TeV-muons. It

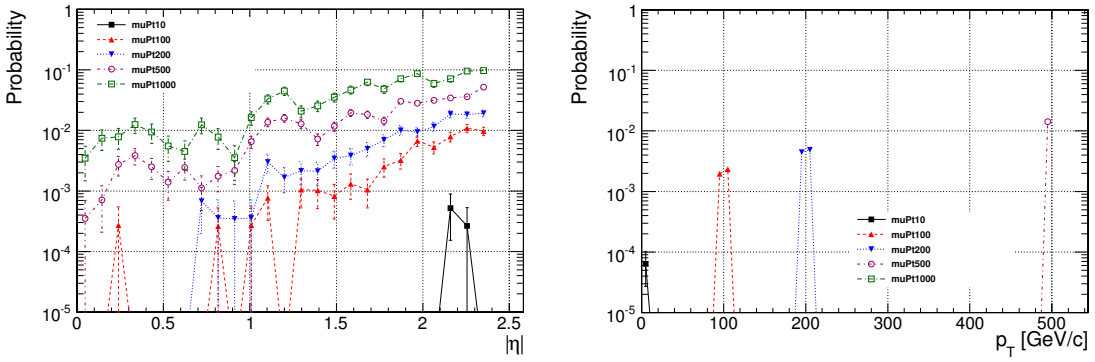

(a) Global charge mis-id vs η

(b) Global charge mis-id vs p_{T}

Figure 53: Charge mis-assignment probability for global muons as a function of η and p_{T}, for different p_{T} samples.

is interesting to note that, contrary to the momentum estimation, the track reconstruction in the tracker alone has a higher probability to assign the correct sign of the charge than the full tracking system. This derives from the more complex assumptions used during the fit of the measurements collected in the whole tracking system. A better assignment can be achieved by either reviewing the assumption made at the fit level or by more heavily weighting the tracker track charge.

7.2.3 Residuals for ϕ , η and d_{xy} and d_z

The q/p_{T} resolution is directly connected to the residual of the ϕ parameter, because the curvature measured in the $r-\phi$ plane determines the q/p_{T} value. Almost all of what has been said for $R(q/p_{\mathrm{T}})$ is also applicable to the ϕ residual. The structure in the $R(q/p_{\mathrm{T}}(\phi))$ present in the stand-alone muon reconstruction is even more evident in the ϕ residual as a function of ϕ (Fig. 54). In the barrel the peaks correspond to the discontinuity between sectors (Fig. 2). In the endcap the structure is due to the geometrical configuration of the CSC stations.

The distribution of the ϕ residual as a function of p_{T}, for the tracker tracks, the seed, the stand-alone and the global muon reconstruction is shown in Fig. 55. The residuals for the global muon and the tracker track reconstruction overlay each other.

$R(\phi)$ is proportional to $1/p_{\mathrm{T}}$, which means it is proportional to r_T, the curvature in the bending plane, as expected. The improvement passing from the stand-alone muon tracks to the global tracks leads to a gain of a factor 40 on the ϕ residual.

The other parameter which defines the direction of the muons is the pseudorapidity (Fig. 43(d), Fig. 47(d)). Also $R(\eta)$ is proportional to $1/p_{\mathrm{T}}$, because a set of positions is what is really measured in the detector. The gain in the η residual passing from the stand-alone reconstruction to the reconstruction with the whole CMS tracking system is a factor of 10. Note also the better resolution around $\eta = 0$ of the global reconstruction with respect to the tracker alone. Although small, it shows the interplay of the two terms in eq. 8.

The other two parameters to be evaluated are d_{xy} and d_z. In Fig. 47 and Fig. 49 these quantities are shown only for the global reconstruction; for the tracker they distribute identically. The resolution (expressed in μm) on the transverse impact parameter is about three times more accurate than the one on the longitudinal parameter. For both parameters, a better accuracy is obtained as the muon transverse momentum increases.

7.3 Muon Reconstruction Parameter Pulls

In order to study the uncertainties assigned to the measured parameters, the pulls are studied in this section. The pull of a variable a is defined as:

$$\text{Pull} = \frac{a^{rec} - a^{gen}}{\sigma_a}.$$

For a normally distributed variable a the pull distributions are Gaussian with null mean value and unit variance. Deviation from unit indicates incorrectly estimated uncertainties. More precisely, if $\sigma_{pull} < 1$ the error is over-estimated, while $\sigma_{pull} > 1$ means the error is under-estimated.

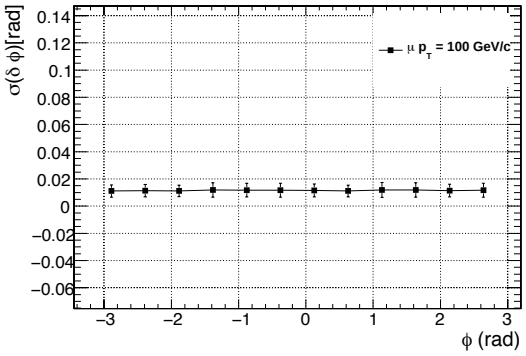

(a) $p_{\mathrm{T}} = 100$ GeV/c in the barrel.

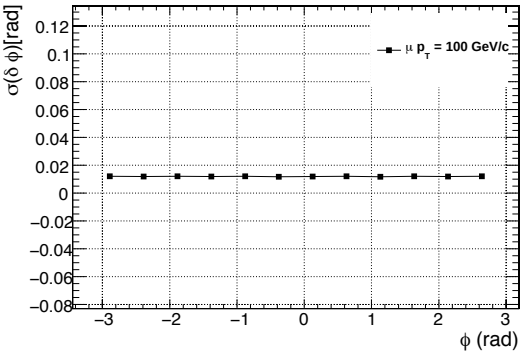

(b) $p_{\mathrm{T}} = 100$ GeV/c in the endcaps.

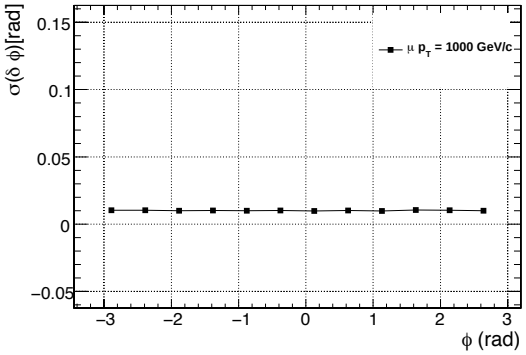

(c) $p_{\mathrm{T}} = 1000$ GeV/c in the barrel.

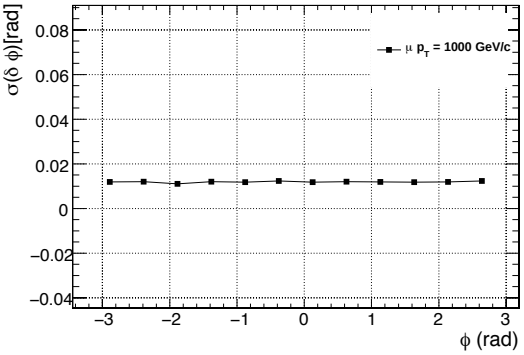

(d) $p_{\mathrm{T}} = 1000$ GeV/c in the endcaps.

Figure 54: ϕ residual as a function of ϕ for the stand-alone muon reconstruction.

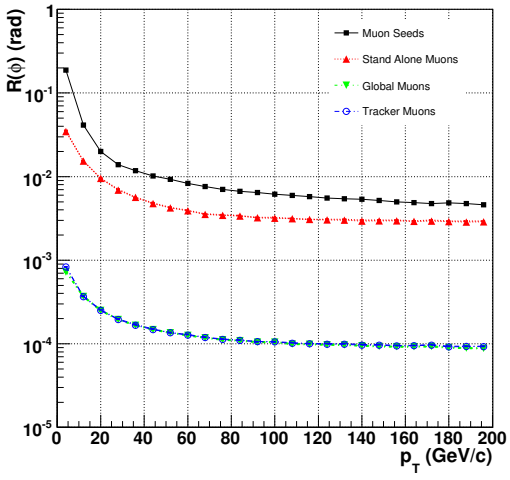

Figure 55: ϕ residual for the different reconstruction steps, evaluated using the $(1 \div 500)$ GeV/c p_{T} sample.

The width of the q/p_{T} pull distributions Fig. 57, Fig. 56, and Fig. 58) shows a complex structure. The pull distributions of η show variation with mean values far from one. The correction in this case is easy, as it implies a set of re-scale factors. The seed algorithm does not compute the errors, instead they were assigned with a dedicated study of the muon seed parameterisation (Section 4.1). This study was performed on an old version of the CMS detector model. Further work is ongoing in order to update the assignment of seed uncertainties.

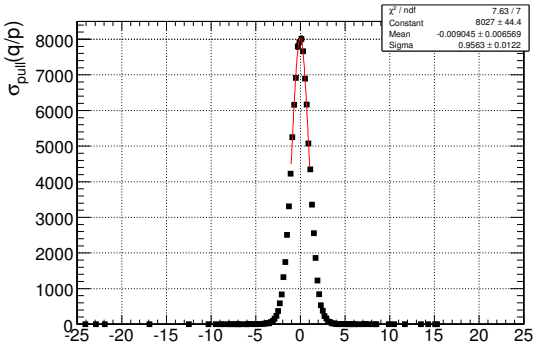

(a) Pull of q/p parameter.

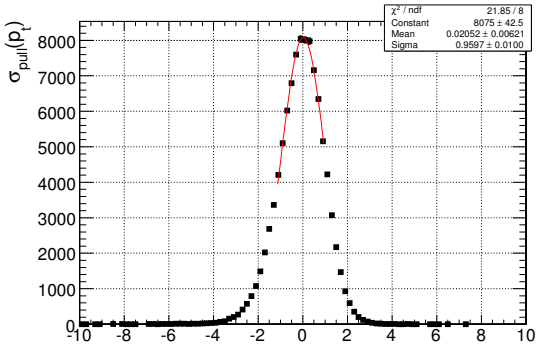

(b) Pull of p_{T} parameter.

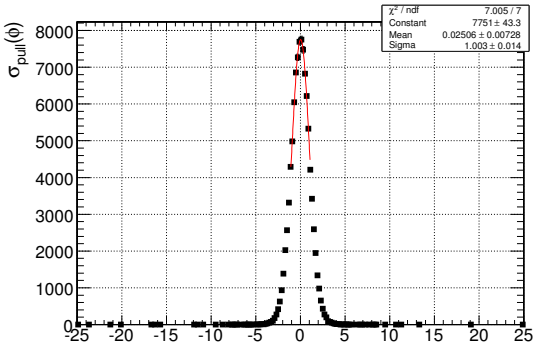

(c) Pull of ϕ parameter.

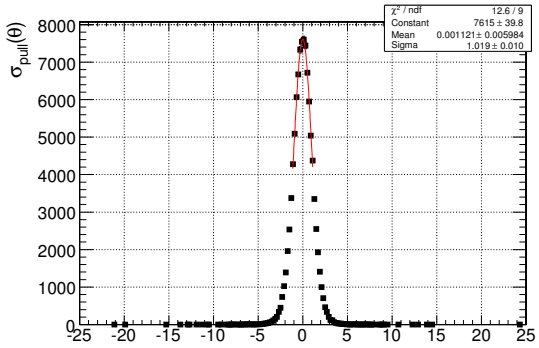

(d) Pull of θ parameter.

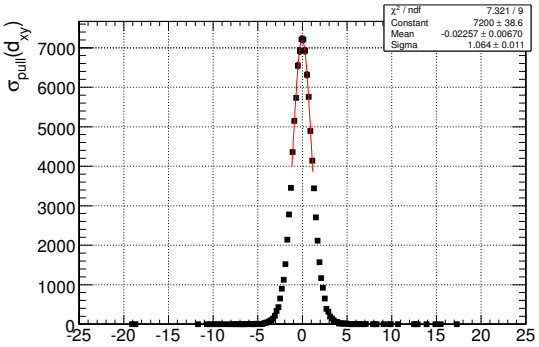

(e) Pull of d_{xy} parameter.

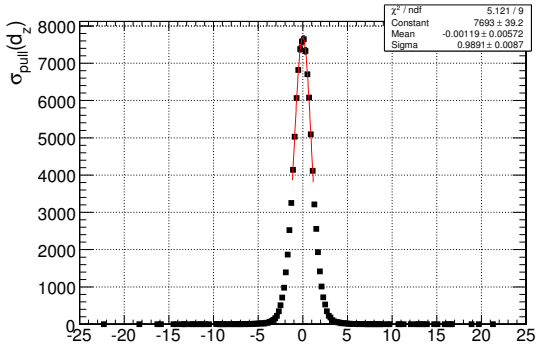

(f) Pull of d_z parameter.

Figure 56: The pull distribution of the track parameters for the tracker reconstruction step.

The stand-alone reconstruction computes the errors together with the parameters; they are better assigned than in the seeding step, although the pull distributions still do not show unit variance. The pull width of the q/p_{T} parameter (Fig. 57) is about 1.4 and indicates that the errors are under-estimated by about 30% of the true value. In the case of TeV-muons the assigned errors are, on average, about 40% of the true value. The uncertainties assigned to η produce pull widths much closer to unity (Fig. 60), but the spectra in η show they are under-estimated in the barrel by 20% and the end-caps by 10%, in average. In the overlap region the errors are well estimated. For 10 GeV/c muons the pull width is equal to one over all the η range.

The pull distributions (Fig. 59, Fig. 61, Fig. 62, and Fig. 64) for the global and the tracker track reconstruction are better, although they show similar features. The q/p_{T} pull variances show that the errors are under-estimated, on average by about 15%. The uncertainties assigned to η distribute with a similar pattern as the one shown for the stand-alone muon reconstruction, but with smaller deviations from unity. The η errors are, in mean, under-estimated by about 10%. The uncertainties on the impact parameters are well estimated (Fig. 58).

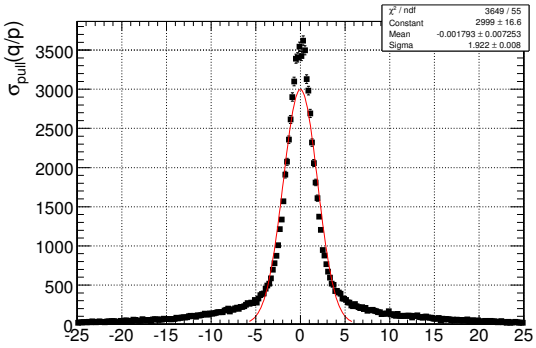

(a) Pull of q/p parameter.

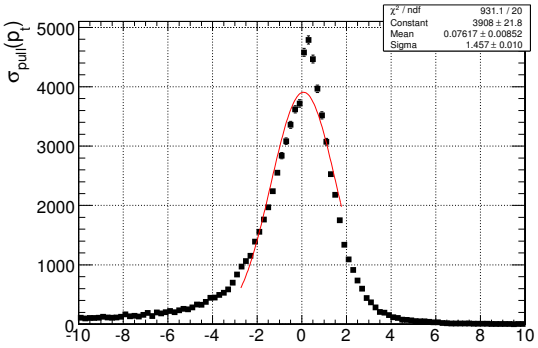

(b) Pull of p_{T} parameter.

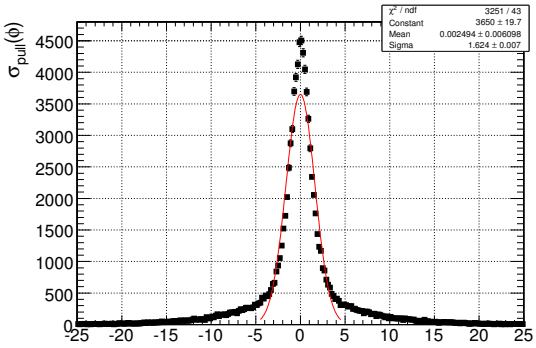

(c) Pull of ϕ parameter.

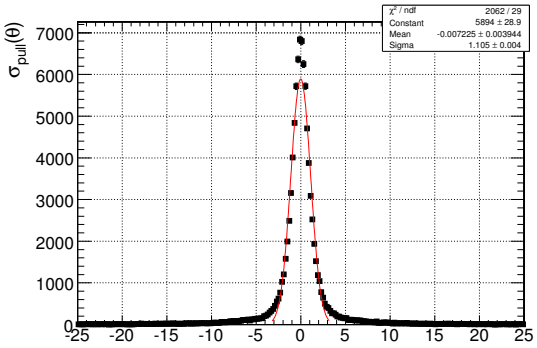

(d) Pull of θ parameter.

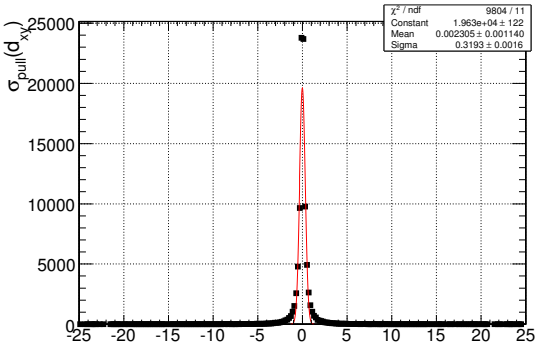

(e) Pull of d_{xy} parameter.

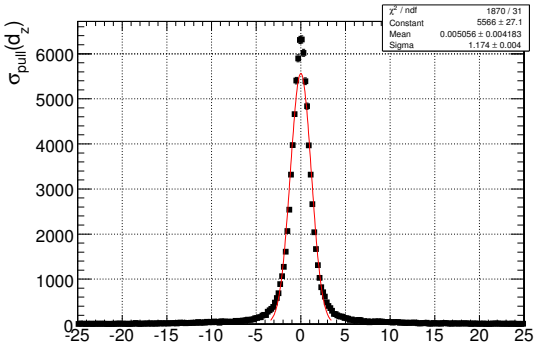

(f) Pull of d_z parameter.

Figure 57: The pull distribution of the track parameters for the stand-alone muon reconstruction step.

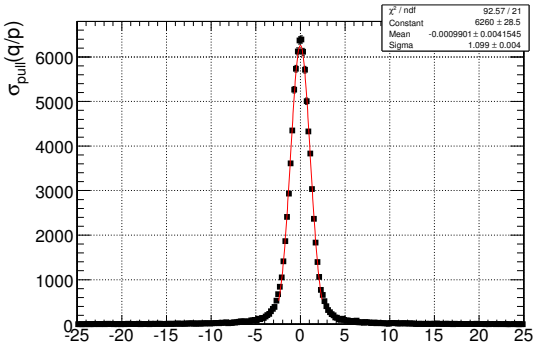

(a) Pull of q/p parameter.

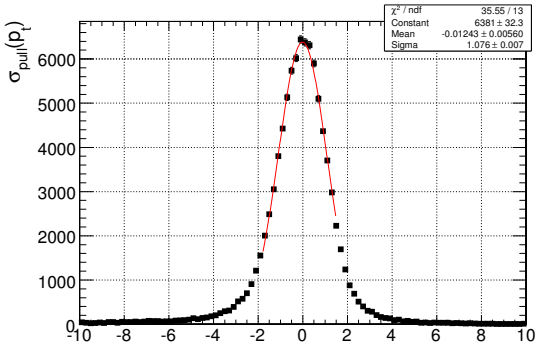

(b) Pull of p_{T} parameter.

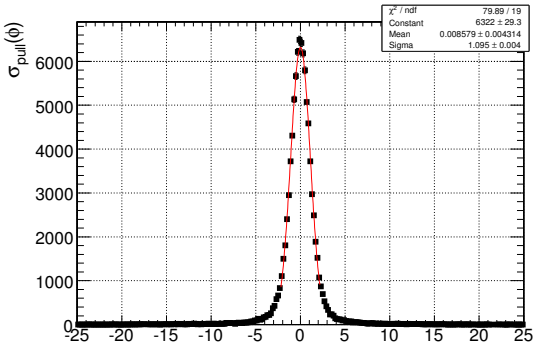

(c) Pull of ϕ parameter.

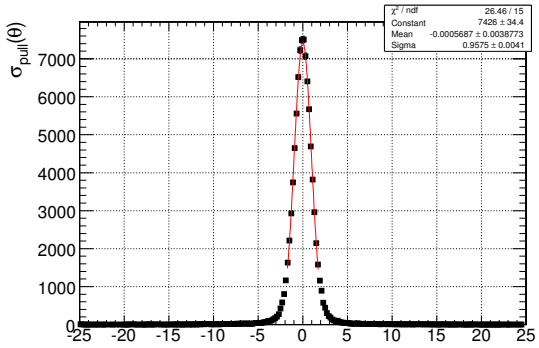

(d) Pull of θ parameter.

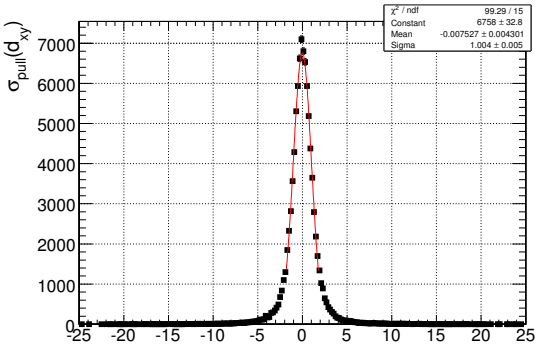

(e) Pull of d_{xy} parameter.

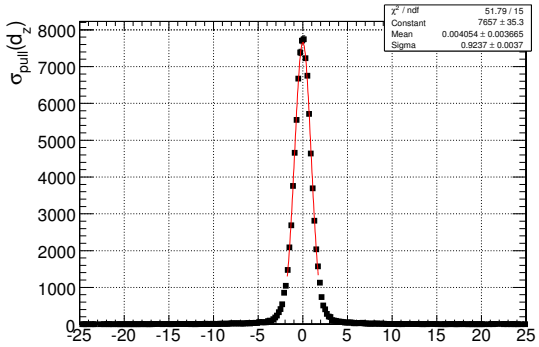

(f) Pull of d_z parameter.

Figure 58: The pull distribution of the track parameters for the global muon reconstruction step.

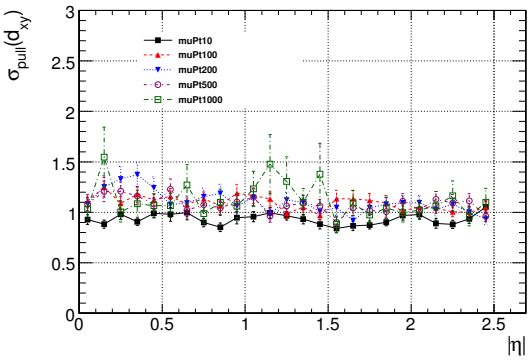

(a) Pull of d_{xy} parameter.

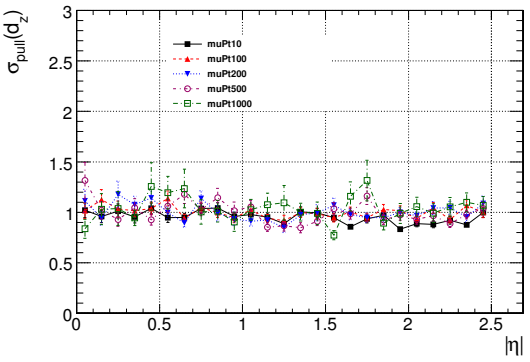

(b) Pull of d_z parameter.

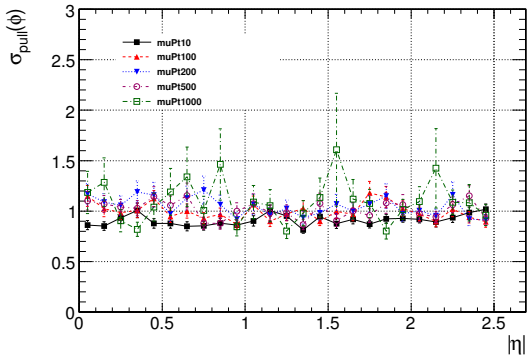

(c) Pull of ϕ parameter.

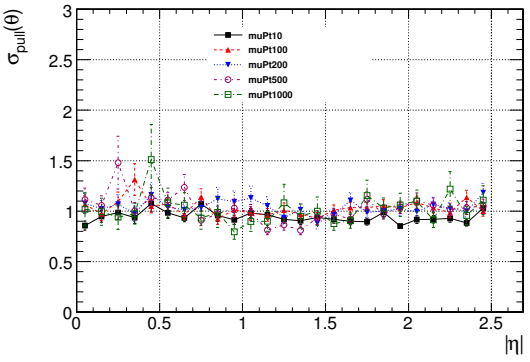

(d) Pull of θ parameter.

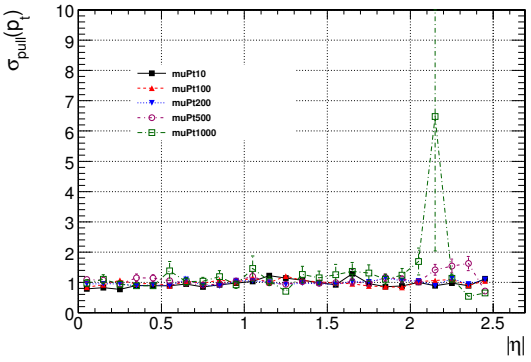

(e) Pull of q/p_{T} parameter.

Figure 59: The pull distribution of the track parameters for the general track reconstruction step.

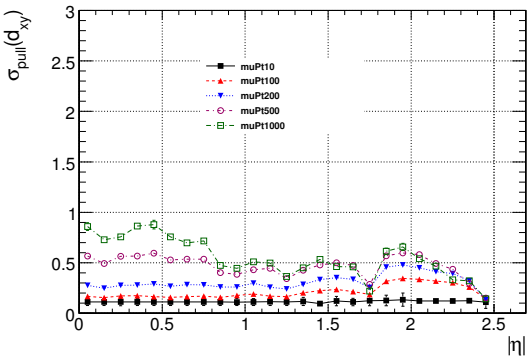

(a) Pull of d_{xy} parameter.

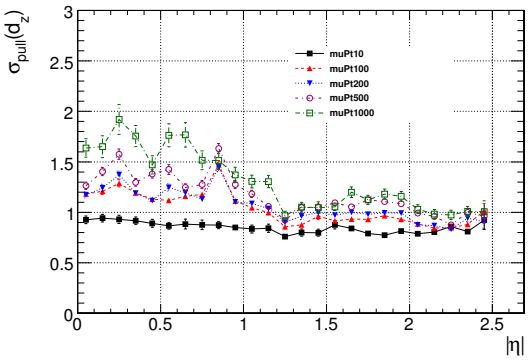

(b) Pull of d_z parameter.

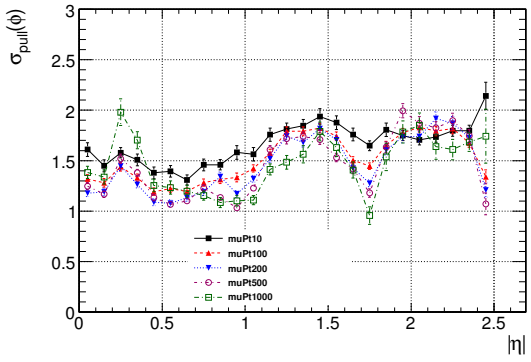

(c) Pull of ϕ parameter.

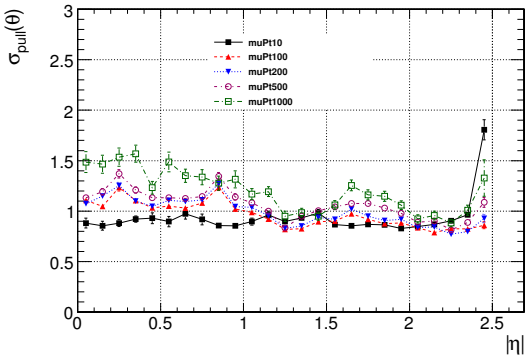

(d) Pull of θ parameter.

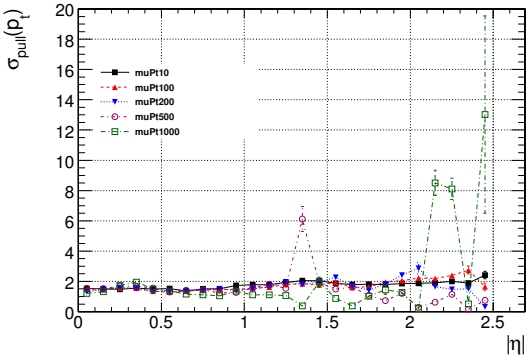

(e) Pull of q/p_{T} parameter.

Figure 60: The pull distribution of the track parameters for the stand-alone muon reconstruction step.

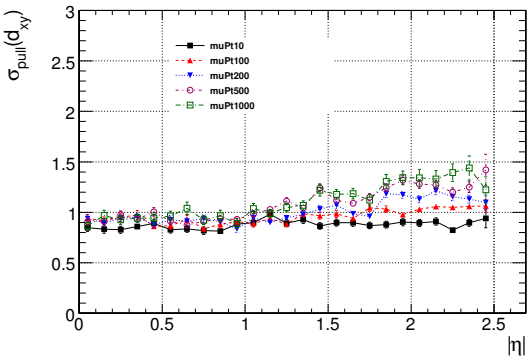

(a) Pull of d_{xy} parameter.

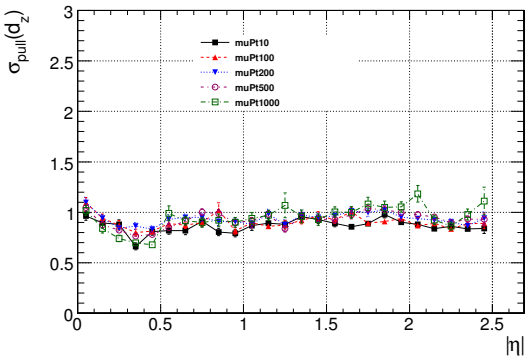

(b) Pull of d_z parameter.

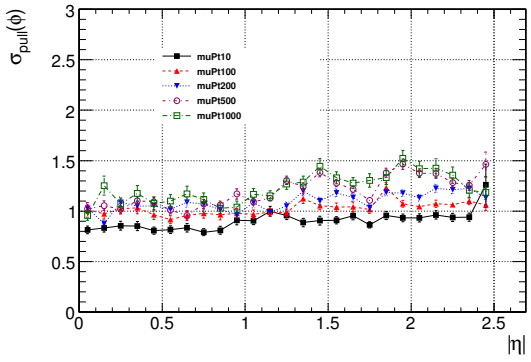

(c) Pull of ϕ parameter.

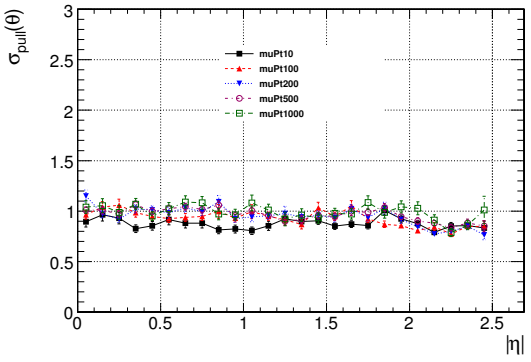

(d) Pull of θ parameter.

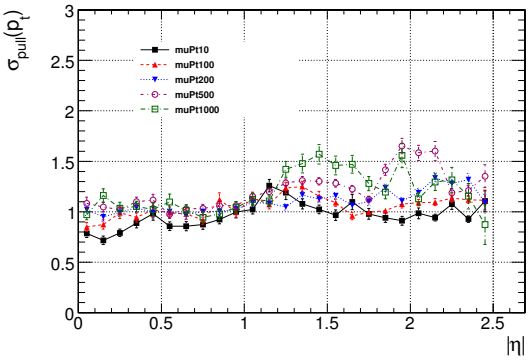

(e) Pull of q/p_{T} parameter.

Figure 61: The pull distribution of the track parameters for the global muon reconstruction step.

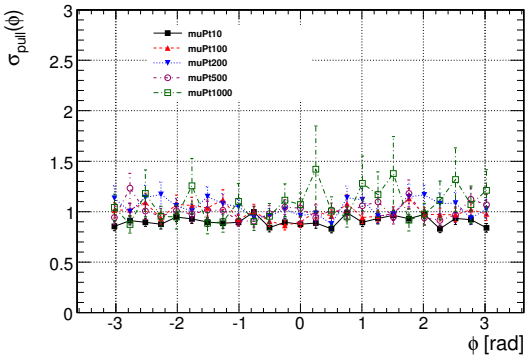

(a) Pull of ϕ parameter.

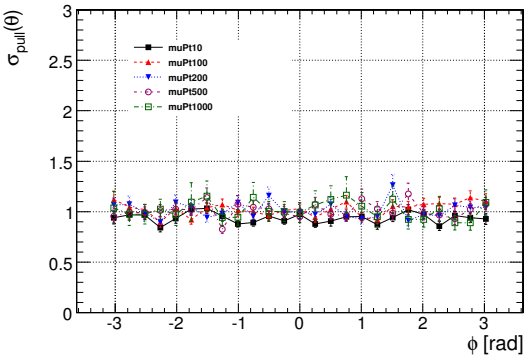

(b) Pull of θ parameter.

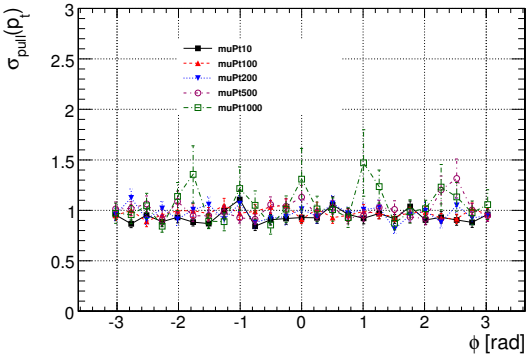

(c) Pull of q/p_{T} parameter.

Figure 62: The pull distribution of the track parameters for the general track reconstruction step.

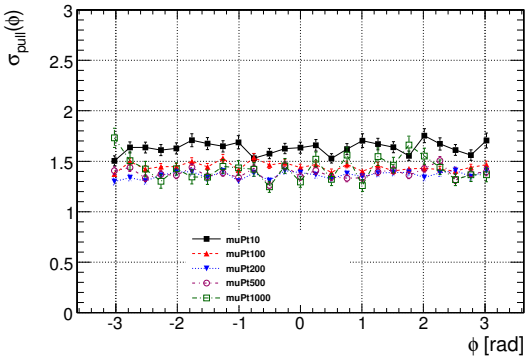

(a) Pull of ϕ parameter.

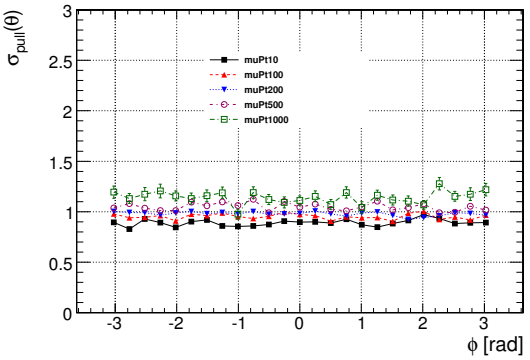

(b) Pull of θ parameter.

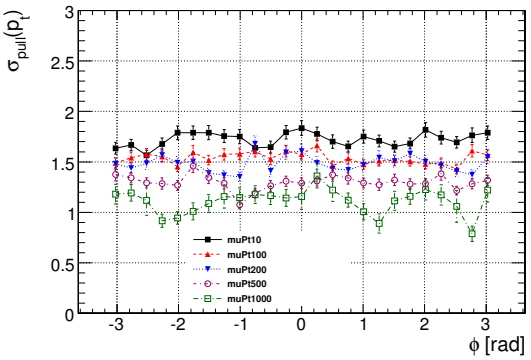

(c) Pull of q/p_{T} parameter.

Figure 63: The pull distribution of the track parameters for the stand-alone muon reconstruction step.

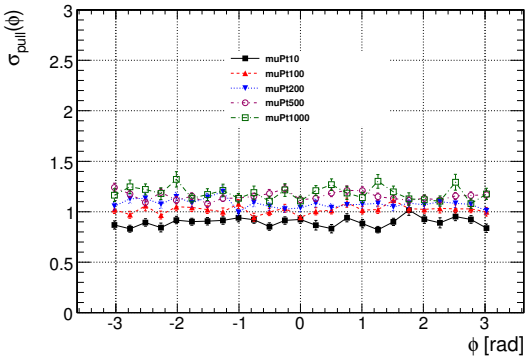

(a) Pull of ϕ parameter.

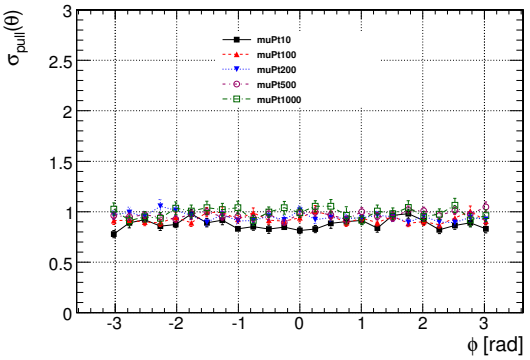

(b) Pull of θ parameter.

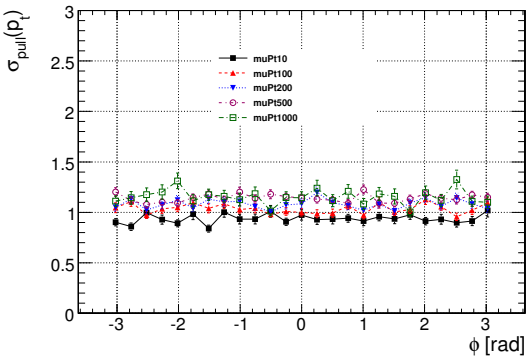

(c) Pull of q/p_{T} parameter.

Figure 64: The pull distribution of the track parameters for the global muon reconstruction step.

8 Conclusions

The ability to identify and reconstruct muons with high efficiency over the whole kinematic range of the LHC is the key to the success of the CMS experiment. This requires algorithms that are robust and flexible and use all the available detector information over the full geometrical acceptance of the CMS detector. We have shown that the current algorithims fulfill all the necessary requirements for the reconstruction of single muons with full detector simulation. Muons are identified and reconstructed with efficiencies of close to 99% with clearly defined understood efficiency losses due to the CMS detector geometry. Muons are reconstructed in three categories

- Stand-Alone muons using just muon detector information and the interaction point
- Global muons which match stand-alone muons with silicon tracker tracks.
- Tracker muons which match silicon tracker tracks with calorimeter energy deposits and muon system hits

The final output from the algorithms is a muon physics object together with a compatibility value indicating the probabilty of the track being a muon. These algorithms satisfy all of the requirements for robust high efficiency reconstruction. These algorithms are the foundation for real data taking and analysis and can be tuned for the more complex environments of real events and actual detector inefficiencies.

Acknowledgements

References

[1] R. K. Bock, H. Grote, D. Notz *et al.*, *Data analysis techniques for high-energy physics experiments*, Camb. Monogr. Part. Phys. Nucl. Phys. Cosmol. **11** (2000) 1.

[2] W. R. Leo, *Techniques for Nuclear and Particle Physics Experiments: A How-to Approach*, Springer, 1987. Berlin, Germany: Springer (1987).

[3] W. Adam, B. Mangano, T. Speer *et al.*, *Track Reconstruction in the CMS Tracker*, CMS Note-2006/041 (2006).

[4] F.-P. Schilling, *Track Reconstruction and Alignment with the CMS Silicon Tracker*, CMS CR-2006/061 (2006).

[5] R. Fruhwirth, *Application of Kalman filtering to track and vertex fitting*, Nucl. Instrum. Meth. **A262** (1987) 444.

[6] W. M. Yao *et al.*, *Review of particle physics*, J. Phys. **G33** (2006) 1.

[7] R. Fruhwirth, W. Waltenberger and P. Vanlaer, *Adaptive Vertex Fitting*, CMS Note-2007/008 (2007).

[8] The CMS Collaboration, *The 2008 CMS Computing Software and Analysis Challenge*, CMS IN-2008/044 (2008).

[9] The CMS Collaboration, *CMS Physics: Technical Design Report. Volume I: Detector Performance and Software*, CERN/LHCC 2006-01, CMS TDR 8.1 (2006).

[10] C. Campagnari *et al.*, *Muon Identification in CMS*, CMS AN-2008/098 (2008).

[11] The CMS Collaboration, *Measuring Electron Efficiencies at CMS with Early Data*, CMS AN-2007/019 (2007).

[12] The CMS Collaboration, *Generic Tag and Probe Tool for Measuring Efficiency at CMS with Early Data*, CMS AN-2008/XXX (2008).

[13] The CMS Collaboration, *The Muon Project, Technical Design Report*, CERN/LHCC 97-32, CMS TDR 3 (1997).

[14] The CMS Collaboration, *The CMS experiment at the CERN LHC*, JINST (2008).

[15] S. Baffioni *et al.*, *Electron reconstruction in CMS*, Eur. Phys. J. **C49** (2007) 1099.

[16] The CMS Collaboration, *CMS Physics: Technical Design Report. Volume II: Physics Performance*, CERN/LHCC 2006-021, CMS TDR 8.2 (2006).